Thesis Report

Modelling Internal Reforming Solid Oxide Fuel Cells with Surface Chemistry to Find Regions Susceptible to Carbon Deposition

by

Ralf Meijer

to obtain the degree of Master of Science
at the Delft University of Technology
to be defended publicly on Monday, June 7, 2021 at 09:00 AM

Student number: 4137434

Thesis committee:

Prof. dr. D.J.E.M. Roekaerts	TU Delft, supervisor
Dr. Ir. J.W. Haverkort	TU Delft
Dr. L. Botto	TU Delft
Ir. J.N. Stam	TU Delft

TU Delft

FOREWORD

This thesis was written in partial fulfilment of Masters degree.
The subject combines sustainable energy technology, mechanical engineering, physics and modelling.
These are all subjects that are important to me. Combining these subjects in one project has been a joy and a real challenge.

DEDICATIONS

Jelle Stam
Saša Kenjereš
Dirk Roekaerts

"Start by doing what is necessary,
then do what's possible,
and suddenly you are doing the impossible"

ABSTRACT
The lifespan of internal reforming solid oxide fuel cells (SOFCs) is not yet sufficient. Among other design challenges, this is due to detrimental carbon deposition formations. This must be mitigated, without compromising the power output and efficiency of the fuel cell for it to become a commercial viable product. The carbon that is deposited originates from a methane/hydrogen mixture, fed to the fuel cell.
All failure modes caused either directly or indirectly by carbon formations are explored. A 3D-model representing part of an SOFC is modelled, in order to identify areas specially susceptible to carbon depositing on the anode. The methane is reformed by a surface chemistry mechanism developed with density functional theory. By doing this, it is possible to model both reaction kinetics and reaction equilibrium of the reforming process.
The final model can accurately model local mixture composition, as well as surface site coverage. The reaction rate and activation energy of methane reforming on a nickel catalyst is also calculated by using the output of the simulations. The site coverage observed can lead to further carbon deposition, but this is not yet modelled.

List of frequently used symbols

Symbol	Name	Units	Symbol	Name	Units
A	Area	m^2	ρ	Density	kg/m^3
A_r	Arrhenius constant	-	σ	Conductivity	S/m
D	Diffusivity coefficient	m^2/s	μ	Viscosity	Pa•s
E	Potenial	V	b	Tafel slope	-
E_{act}	Activation Energy	J/mol	c	Concentration	mol/m^3
F	Faraday constant	A/mol	c_p	Specific heat	J/kg/K
G	Gibbs Free energy	J	d	Thickness	m
H	Enthalpy	J	h	Specific enthalpy	J/kg
I	Current	A	j	Current density	A/m^2
L	Length	m	j_*	Exchange current	A/m^2
N	Molar flux	$mol/m^2/s$	k	1^{st} order rate constant	s^{-1}
R	Ohmic resistance	Ω	k_f	Rate constant	-
S	Entropy	J	n	Number of electrons	-
T	Temperature	K	p	Pressure	Pa
Sh	Sherwood number	-	t	Time	s
Gz	Graetz number	-	u	Effective velocity	m/s
β	Temp. coefficient	-	v	Velocity	m/s
η	Over potential	V	x, y, z	Dimensions	m
κ	Ionic conductivity	S/m			

List of frequently used subscripts and prefixes

a	Anode	w	Wall
c	Cathode	$\bar{y}$	Dimensionless variable y
d	Diffusion layer	$\dot{y}$	Time derivative of variable y
in	Initial	Δy	Difference (Delta) of y
m	Mean	0	Standard conditions
r	Reaction		

List of most relevant abbreviations

CFD	Computational Fluid Dynamics	IR	Internal Reforming
CHP	Combined Heat and Power	OCV	Open Circuit Voltage
DRT	Distribution of Relaxation Time	PEM	Proton Exchange Membrane
DES	Detached Eddy Simulation	S/C	Steam to Carbon (ratio)
FEM	Finite Element Model	TPB	Triple Phase Boundary
HT	High Temperature	SOFC	Solid Oxide Fuel Cell
IT	Intermediate Temperature	YSZ	Yttria Stabilised Zirconia

1 - Introduction

In 2019 the growth in carbon emissions started to slow down, compared to the previous years. This is due to the fact that renewable energy sources, but mainly natural gas are replacing more and more coal fired power plants (BP, 2019).
Another important aspect was the overall decrease in growth rate of total energy consumption, from 2.8% to 1.3%. This diminishing growth, caused by a decline in energy intensive economic activity in western Europe and the United States is somewhat compensated by China, India and Indonesia. These last three countries combined are now for over 85% responsible for the increasing demand in fossil fuels. This makes sense, since the economies in these countries are developing, resulting in higher standards of living. An increase in GDP is strongly related to higher energy demands, as table 1.1 shows. The equivalent electric power use, CO_2 emission and growth domestic product per capita

Country	PE use (MWh) /capita year	CO2 (metric ton) /capita year	GDP ($ US) /capita year
Canada	105	15.69	46.195
USA	80.1	15.52	65.298
Australia	70.2	17.27	55.060
Germany	44.0	8.52	46.445
Japan	41.1	9.09	40.247
UK	32.7	5.54	42.330
China	28.2	8.12	10.262
Brazil	16.3	2.25	8.717
Indonesia	9.15	2.32	4.136
India	6.93	1.90	2.100

Table 1.1 - Primary Energy (PE) demand, CO_2 emission and GDP per capita year for some countries in 2019. (BP, 2019)

Table 1.1 above shows two interesting geographical phenomena. Firstly, the substantial gulch in energy demand between the USA and Japan, Germany and the UK is remarkable considering the standard of living in these countries is comparable.
Another important aspect is the clear correlation between countries with substantially lower GDP's and lower energy demand.
The idea of 'energy justice' suggests that every person in the world should have equal and unbiased access to natural recourses, of which energy accessibility is one of the most important. Regional availability should be taken into account of course. Along with this concept of energy justice arises the question wether poor countries have low energy demand just because they need to develop their economies further, or is this not possible due to a lack of resources? The second possibility is sometimes referred to as 'energy poverty' (Sovacool & Dworkin, 2014).

Looking back to table 1.1, a simple thought experiment where all countries either rise or drop in energy use and CO_2 emission to a level compared to the UK exposes the ultimate challenge in sustainable worldwide energy supply.
The natural fossil reserves would be depleted in one or two generations. The only viable option to achieve this goal will rely heavily on non-fossil based solutions for practically all uses of energy.

Figure 1.1 shows the efficiency and scale of conventional power generation techniques. These generators rely on volumetric processes limited by the thermodynamic Carnot efficiency. Efficiencies of nearly 60% can be reached, but only at the largest scales using the most complex and expensive combined cycle.
A fuel cell is an electrochemical energy conversion device. Fuel cells can also reach higher efficiencies of up to 65% (LHV) and due to their modular nature, can be scaled from 1 kilowatt to several megawatts. Broadly speaking, fuel cells are limited by the interfaces on which this conversion takes place.

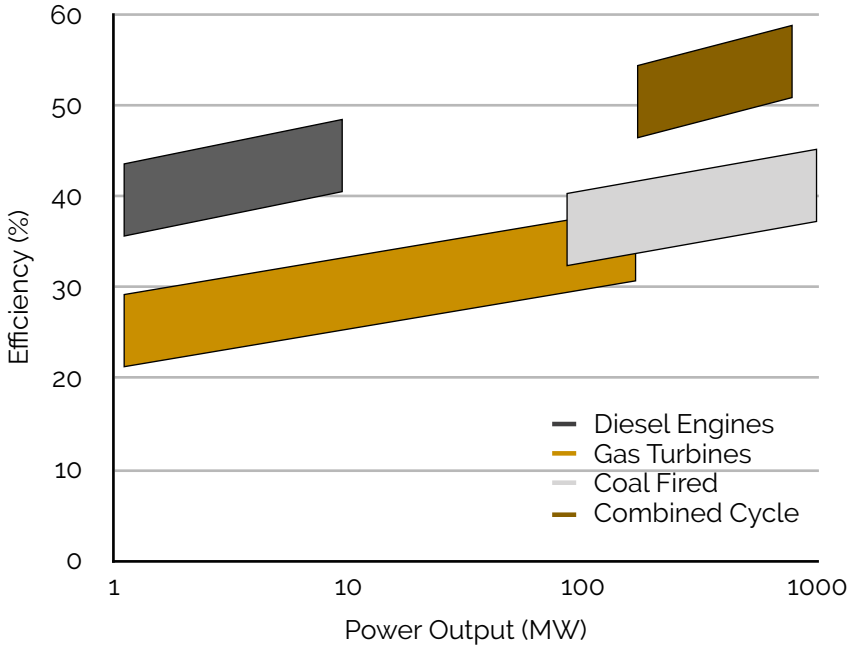

Figure 1.1 - Power output and efficiency of conventional generation methods. Adjusted from (Boaro & Salvatore, 2017)

When NASA used fuel cells in the Apollo program it was considered to be a highly specialised device, but since then more and more uses have been found.
The scalability of fuel cell technology made it possible that fuels cells are used on small and large scale in transport, military, industry, commercial and finally general power generation for residential use.

Solid Oxide Fuel Cells (SOFCs) are especially interesting devices from the perspective of fuel flexibility. Not only hydrogen, but also methane, ethane, several alcohols and ethers, as well as carbon monoxide and even pure coal could be used as fuel. A mixture of hydrogen and one of these fuels is also a viable option. Fuel cells that (partially) run on a hydrogen-rich reformed fossil fuel are called reforming fuel cells.

Reforming SOFCs could be a vital chain in the global transition to sustainable energy sources. Furthermore, reforming SOFCs are more energy intensive devices compared to their hydrogen counterparts. The increased energy density of these devices makes them suitable to power freight ships for example. Currently, the lifetime of these reforming SOFCs is not sufficient for commercial applications. The lifetime is mostly limited by failures caused by carbon deposition.

SCOPE OF THIS THESIS

The main focus of this thesis is to further the understanding in carbon deposition mechanisms in solid oxide fuel cells running on a mixture of methane and steam.
This will be done by modelling part of a 3D fuel cell where both methane reforming and hydrogen evolution from standard fuel cell operation occur simultaneously. The reforming process is simulated by real kinetic reaction rates of 42 intermediate surface reactions. Unlike other simulation methods where the chemical equilibrium is used as an input to estimate the local reaction rate, the chemical equilibrium will be a resulting feature of the model in this case. A true transient of the reacting species may be obtained this way.
The resulting temperature distributions and surface species concentrations could be used to identify regions and operating conditions that contribute to carbon deposit formation. Since the ultimate goal is to suppress carbon deposition altogether, no attempts will be made to model continuing evolution of carbon formations.

GOALS OF THIS THESIS

This thesis consists of a literature study and a set of models of increasing complexity. The literature study has four subgoals

- Identify all failure modes of SOFCs either directly or indirectly related to carbon deposition.
- Determine what type of model is best suited to model carbon deposition.
- Identify physical phenomena that can either be omitted in the model, or must be present in order to obtain accurate results.
- Determine the scale and complexity required to model carbon deposition accurately

The models that are consequently developed take these findings into account. Using non-transient operating conditions the following results will be presented

- Chemical equilibrium conditions at varying temperatures
- Temperature distribution inside the channel
- Rate of reaction of methane reforming
- Activation energy of the overall reaction
- Species distribution along the channel
- Concentration of intermediates on the active surfaces

The goal is to use these results to find the critical areas inside the channel that are most vulnerable to carbon deposition.

OUTLINE OF THIS THESIS

Chapter 2 will provide further insight in the general working principles, as well as details on the type of materials most often used. Finally, this chapter concludes with some performance and efficiency figures and developments. This chapter gives an impression on the current state of SOFC technology.

Chapter 3 goes into failure modes of SOFCs, with a special focus on internal reforming fuel cells. As will be made clear in this chapter, the lifetime of the fuel cell is threatened by several failure

mechanisms. First some background on fuel composition and cell degradation are given. A complete picture of all chemical and physical degradation mechanisms are given. The causes and effects of some of these mechanisms are intertwined.
Finally, solutions to one failure mode might increase the rate of degradation from another mechanism. This is why this chapter provides a complete picture of all failure modes of SOFCs.

Chapter 4 provides an overview on different modelling strategies currently employed. It is important to be aware of the limitations a particular modelling technique possesses.
Every model is a mathematical representation of reality, which will always be infinitely more complex. That being said, a model of high quality must be able to predict how a system will behave. This chapter compares modelling techniques previously used for fuel cells running on pure hydrogen. This chapter identifies crucial aspects to accurately model carbon deposition in combination with fuel cell operation.

Chapter 5 consists of a comprehensive description of the models used. The models consists of a combination of theories discussed in chapter 4. Besides the governing equations, the model dimensions and mesh parameters are shown in this chapter as well. Furthermore, all boundary conditions and initial conditions are specified in this chapter. Finally, the mesh quality and mesh independence will be demonstrated for a fuel cell at open circuit conditions, as well as the reforming mechanism in a standalone configuration.

Chapter 6 presents the results. The results are compared to earlier works, both theoretical and experimental.

Chapter 7 concludes this thesis. The main goal was to identify regions prone to carbon deposition. Some recommendations to reduce the chance of carbon deposition are also presented. The models used in this thesis could be used to test these recommendations.

2 - Background on SOFC

This chapter contains only the basic background on SOFCs, to provide an overview of all the required nomenclature and definitions used in the rest of the thesis. Additionally, the current state of the industry is also reviewed. Most of the fuel cells already in commercial use are atmospheric devices with temperature ranges from 550 °C up to 1100 °C. Recent efforts have made it possible to lower the operating temperature considerably, which can be seen from this wide temperature range. Together with other operating conditions, and working principles of solid oxide fuel cells, accompanying performance figures are listed in subsequent sections. These performance figures are not only listed to provide an overview on the current state of fuel cell technology. They are primarily used in this paper to compare the performance figures of the modelled fuel cell. To provide a complete image on the performance of different kinds of SOFCs, cost of fuel cell materials and operation are listed in the next section. This overview might be useful to spot diminishing returns on performance compared to the required costs and materials, but this is analysis lies outside the scope of this thesis. The information in these chapters are well-established in the field of fuel cell technology, and can also be found in general books on fuel cells (Lipman, 2019) (Sammes, 2006).

2.1 - Working Principles

Figure 2.1 shows a basic solid oxide fuel cell. Hydrogen flows through a channel and reacts with the oxygen ions diffusing through the electrolyte layer, forming water as the only product. The transport of oxygen ions is balanced by the electrically connecting the anode and cathode with each other, resulting in a positive supply of electrical energy.
The anode and cathode side reactions are shown in reaction 2.1 and 2.2. The overall reaction (2.3) is found by adding the two together.

$$2\,H_2 + 2\,O^{2-} \rightarrow 2\,H_2O + 4\,e^- \qquad [2.1]$$

$$O_2 + 4\,e^- \rightarrow 2\,O^{2-} \qquad [2.2]$$

$$2\,H_2 + O_2 \rightarrow 2\,H_2O \qquad [2.3]$$

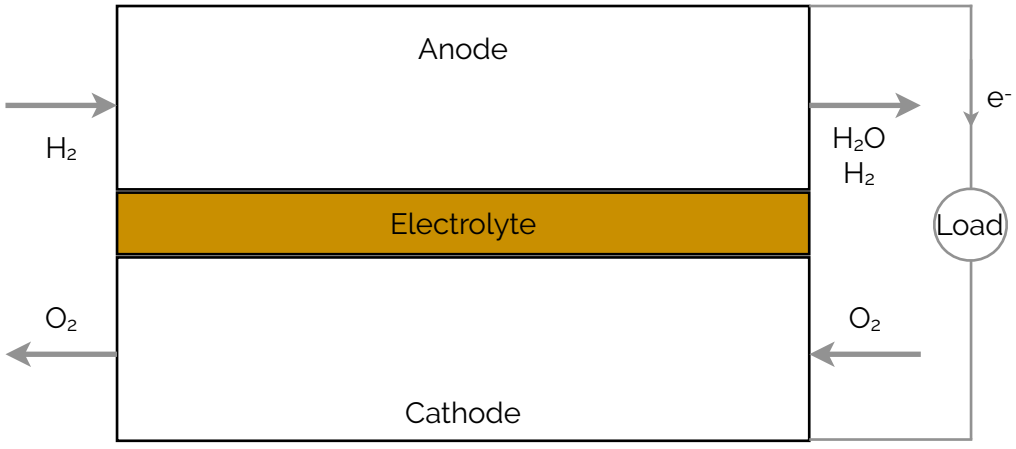

Figure 2.1 - Basic working principle of a solid oxide fuel cell running on pure H_2 and O_2

For internal reforming (IR) SOFCs, several global reactions influence the electrochemistry. Direct oxidation of methane is given by equation 2.4. The electrochemical conversion of methane is not very common. This global reaction requires four oxygen ions per methane, collision theory of chemical reactions tells us that many other reactions will be much more favourable. Many studies exist where CO2 is electrochemically reduced to CH4 (reversed process as in reaction 2.4), but this lies outside the scope of this thesis (Pan & Barile, 2020).
Equation 2.4 does show however, that one methane molecule could potentially result in eight free electrons. Whereas one hydrogen molecule only provides two free electrons. This is the reason why SOFCs running on fossil fuels have a larger specific energy output than SOFCs running on pure hydrogen.
The role of CO electrochemistry in IR SOFCs is still debated. Experiments have shown that when hydrogen is available, electron transfer practically always favours this route (Tabish, Patel, & Aravind, 2017). Nevertheless, the global reaction given by reaction 2.5 is valid from first principles, and this reaction is for sure relevant for SOFCs running on pure CO.
The steam reforming reaction is given by equation 2.6. Together with the Boudouard reaction and the water-gas shift reaction, this reaction controls the mixture compositions without electron transfer. In other words, this reaction still takes place at open circuit conditions.
Another variant of that is sometimes reported is given by equation 2.7, the partial oxidation of methane. This reaction requires oxygen, not oxygen ions. In case of excessive gas leakage from cathode to anode, the methane partially (or fully) combusts. Just as in equation 2.6, no electron transfer is required. The energy release from these processes might assist in maintaining the temperature inside the SOFC, but they do not contribute towards the electric power output of the cell.

$$CH_4 + 4\,O^{2-} \rightarrow 2\,H_2O + CO_2 + 8\,e^- \quad [2.4]$$

$$CO + O^{2-} \rightarrow CO_2 + 2\,e^- \quad [2.5]$$

$$CH_4 + H_2O \rightarrow CO + 3\,H_2 \quad [2.6]$$

$$2\,CH_4 + O_2 \rightarrow 2\,CO + 4\,H_2 \quad [2.7]$$

2.2 - Classification of SOFCs

Fuel cells are typically classified by two different metrics; operating temperature and electrolyte material.
Solid oxide fuel cells operate at very high temperatures compared to proton exchange membrane fuel cells for example. Table 2.1 lists some key features of both kinds of fuel cell, to highlight the difference between the two.

Compared to PEM fuel cells, the range of operating temperatures for SOFCs is roughly 500 °C. Along this wide temperature range, melting points of several materials are crossed. From both a practical and modelling point of view, it is often necessary to further specify what type of SOFC is being discussed. The distinction between intermediate-temperature SOFCs (IT) (550 °C - 800 °C) and high-temperature (HT) SOFCs (800 °C - 1100 °C) is therefore made. It should be noted that the border between these temperature ranges is somewhat vague.

	PEMFC	SOFC
Electrolyte	Polymer	Ceramic
Temperature	70 - 100 ˚C	550 - 1100 ˚C
Fuel	H_2	CH_4, CO, H_2
Mobile ion	H^+	O^{2-}
Oxidant	O_2/air	O_2/air
Efficiency (LHV)	25 - 30 %	50 - 65 %

Table 2.1 - Key characteristics for SOFCs compared to PEM fuel cells. Compiled from (Hyundai Motors FE Fuel Cell) and (Bloom Energy ES5)

2.3 - Performance of SOFCs

The performance of a SOFC can be defined in many ways. This section provides a thermodynamic viewpoint, as well as a more practical way based on the cell potential which can be used during cell operation. Typical losses in fuel cell losses can also be expressed as potentials, which can be subtracted from the open circuit voltage to obtain another way of defining the cell efficiency.
These definitions of efficiency provide a way to compare the performance of SOFCs to internal combustion engines, photovoltaic technologies and of course other types of fuel cells.
Ultimately, the resulting performance of the model can also be compared by using the definitions and concepts from this section.

THERMODYNAMIC EFFICIENCY

Just like the Carnot efficiency for internal combustion engines and Betz's law for wind energy, upper limits for the efficiency of fuel cells are defined. One common measure of a theoretical attainable efficiency is given in equation 2.8.

$$\eta = \frac{\Delta G}{\Delta H} \qquad [2.8]$$

Equation 2.8 is based on the thermodynamic properties of a process where reactants form products. The useful output of a reaction like reaction 2.8 can be measured in the difference in Gibbs free energy. ΔH by definition is invariant to temperature changes, and for gaseous product (H_2O) is 248 kJ/mol. Due to the second law of thermodynamics ΔG does vary with temperature. This dependency on temperature is shown in figure 2.2. The maximum theoretical thermodynamic efficiency of a fuel cell will therefore decrease with increasing temperature. The maximal attainable thermodynamic efficiency at 1000 °C is 71.5%. Table 2.1 reports efficiencies of only 50 - 55%. The next section briefly explains this discrepancy.

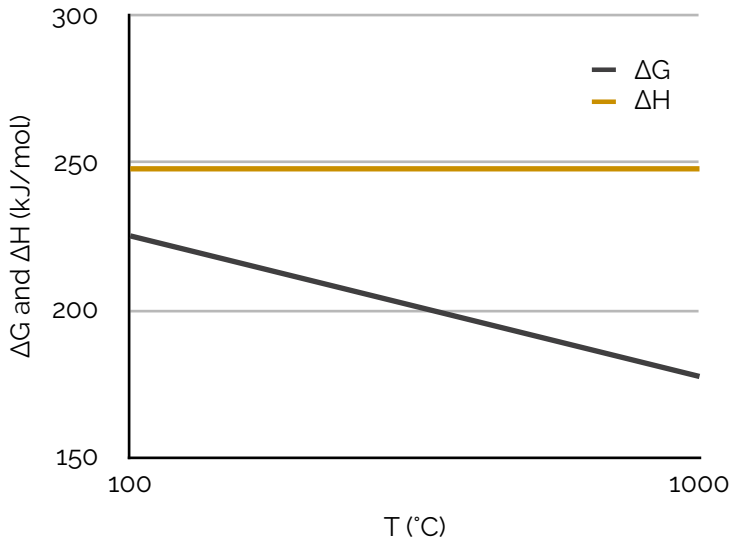

Figure 2.2 - ΔG and ΔH for hydrogen oxidation at varying temperatures

VOLTAGE EFFICIENCY

Another measurement for cell efficiency is given by the quotient of the open circuit voltage and operating voltage, as in equation 2.9. The cell potential drops with increasing current density, cause by a combination of losses described below.

$$\eta = \frac{E_{OC}}{\mathrm{E}(i)} \qquad [2.9]$$

FUEL CEL LOSSES

The cell efficiency depicted in figure 2.2 represents the theoretical maximum. Due to practical limitations when the cell starts to produce a current, the highest efficiencies are actually reached at temperatures around 900 °C to 1000 °C. These practical limitations can be categorised as activation losses, ohmic losses, concentration losses and cross-over losses. These principles are defined in most books on fuel cells, and repeated very briefly here.

Activation losses are caused by the limited rate at which electrochemical reactions take place. They are usually expressed in a potential drop relative to the open circuit voltage, that is needed to drive the reaction forwards. One of the reasons why better efficiencies are reached at elevated temperatures, is the reduction in activation energy and resulting improving reaction kinetics. Finally, the potential associated with activation losses increases with current density.

Ohmic losses are similar to the general resistance any electrical circuit experiences. Electric resistances inside the cell, stack and connecting cables all contribute to the overall ohmic losses. Just as with traditional ohmic losses, this increases linearly with current density. By far the most important contributor is the ionic resistance inside the electrolyte. In most SOFCs this is the limiting resistance, contributing the most to the ohmic potential losses. The ionic conduction improves with increasing temperature, another reason why high temperature SOFCs are generally more efficient.

Concentration losses are caused by mass transfer limitations. The reactions taking place both on the anode and cathode are surface reactions. The partial pressure of reaction products increases along

each fuel channel, and similarly the partial pressure of oxygen decreases in the air channel. These changes in partial pressures limit the reaction speed in the bulk of the channel.
Several times the stoichiometric value of air is usually supplied to the air channels to mitigate concentration losses on the cathode side. This is not an option for the fuel side, since the hydrogen or fossil fuels that not react can't be recovered without exerting additional energy. A fuel utilisation of 70% to 80% is generally accepted. When the current density increases and all the fuel is used the potential associated with concentration losses increases dramatically. The current density that is ultimately limited by mass transfer is called the limiting current density. The limiting current density increases with temperature to some extend, since diffusion is a temperature dependent phenomenon. The improved diffusion rate is countered by improved reaction kinetics though, which will still limit the maximum current density.
For porous electrodes, commonly used in fuel cells, the mass transfer limitations can become even more critical. The very small cavities in which mass transfer occurs requires special methods to model accurately. Since the overall mass transfer rate may be limited by the porous electrodes, it is clear that this requires special attention.

Cross-over losses is the collective term for fuel or air leaking to places where they negatively influence overall cell performance. This is the case when either fuel leaks through the electrolyte to the air channel, or air leaks to the fuel channel. This results in the combustion of the fuel, and this energy is not harvested by an electrochemical cell.
Another form of cross-over loss is caused by the electrolyte material. In practice, this is never a perfect electrical insulator, allowing for internal current flow that is not captured by the external current collectors.
These imperfections result in a difference between the theoretical Nernst potential and a measured open circuit potential. A schematic overview of all these losses vs. current density is given in figure 2.3. Ohmic losses increase linearly with increasing current density. Concentration losses increase significantly at higher current densities. Activation losses occur as soon current flows, but is relatively invariant to increasing current densities. Subtracting all these losses from the open circuit voltage gives the total loss at each current density.
Figure 2.4 shows how these losses affect cell performance at various temperatures. The power density curve is also drawn, showing a maximum power density at 800 °C. This coincides with the highest efficiency (52.7%) as well, according to equation 2.9.

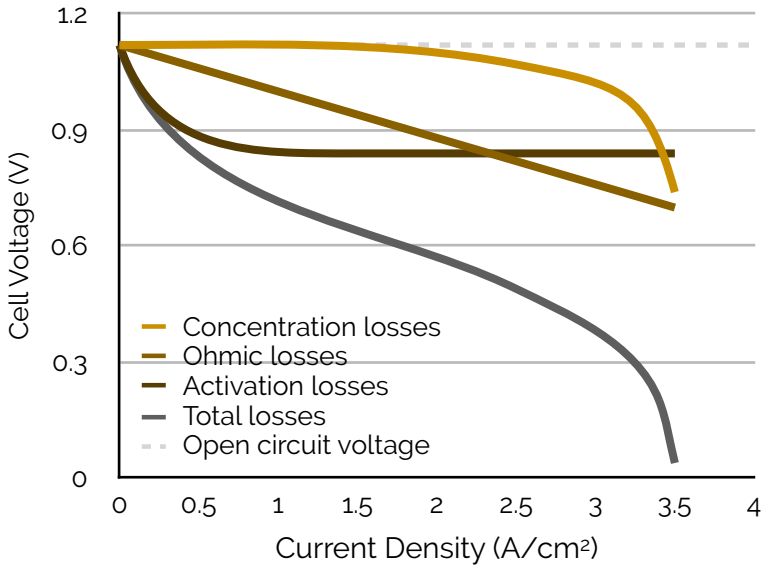

Figure 2.3 - Schematic contribution of each type of potential loss vs. current density

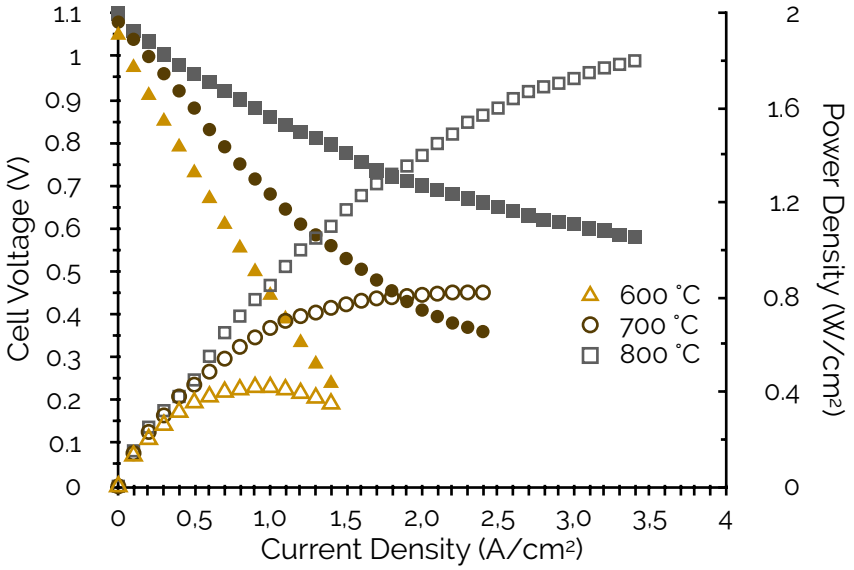

Figure 2.4 - Performance of optimised anode-supported SOFCs at 600, 700 and 800 ˚C, adapted from (Zhao & Virkar, 2005)

2.4 - Materials used in SOFCs

One of the drawbacks of fuel cells (this problem is not limited to SOFCs alone) is that they require certain specific materials. The scarcity and resulting prices of these materials put a high pressure on the unit cost of fuel cells in general. Just as in the field of photovoltaic energy, material studies focussing on increasing performance whilst lowering material cost are continuously being published.
The model in this thesis features well-known materials, for three reasons. First of all, the materials used are fundamentally sound, tried and tested. This will be shown in the following sections.
Additionally, an abundance of data ranging from temperature dependant conductivity tables to complete surface mechanisms are already developed for these materials. Finally, a wide range of experimental data can be used for validating the results emerging from the model.

ANODE MATERIALS

The catalyst on the anode side of the fuel cell, together with the electrolyte, is of critical importance for a well functioning device. This is especially the case for internal reforming SOFCs, whereby the catalytic layer has to cope with carbon deposition.
A suitable catalyst must be able to reform methane. Both a strong affinity with methane to stick to the catalyst surface, as well as the ability for the carbon products to desorb are important. Studies investigating how metallic catalyst promote methane cracking and the water-gas shift reaction show that nickel (among others) is a good candidate from this respect. See table 2.2 for a brief overview from these studies (Wu et al., 2013).

For internal reforming SOFCs, the nickel catalyst serves three goals. It acts as the electronic current collector on the anode side, needs to promote hydrogen oxidation, and finally is the catalyst for the steam reforming reactions. The steam reforming process outside SOFCs is an old and well understood process. It is developed for hydrogen production in the 1930s. The catalyst that supports this reaction at the required operating conditions is nickel. Usually the nickel is supported on a spinel made from aluminium or magnesium compounds, with a nickel loading of around 25% w/w and particle sizes smaller than 10 nm.

Catalysts	Performance
Au, Ag, Zn, Pd, Ga	Promote CO
Pt, Ni, Fe, Ti	Promote H_2
Pb, Hg, In, Sn, Cd	Promote HCOOH
Cu	Promote CH_4

Table 2.2 - Metallic catalysts promote different products from the same methane-hydrogen mixture

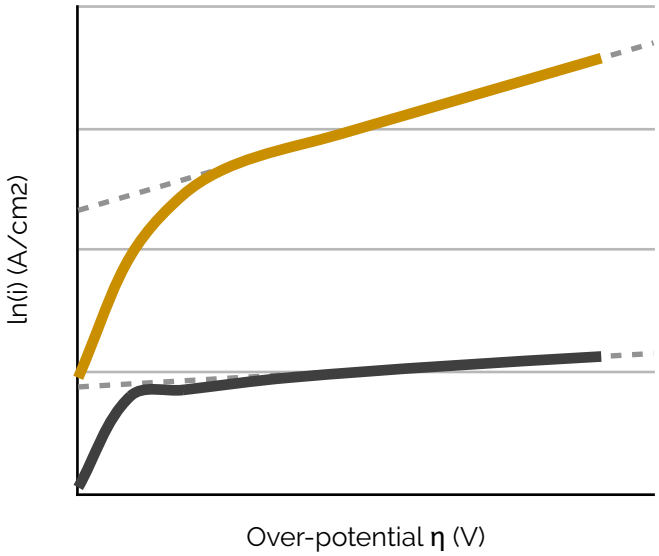

Figure 2.5 - Schematic overview of two Tafel plots for different catalysts

The catalyst on the anode side must also be able to handle the temperatures and oxidising environment it resides in. Furthermore, it must also be an excellent electrical conductor. Finally, a fast reaction rate is also desired. A way for comparing reaction rates and conductivity can be done using Tafel plots. Tafel plots, as in figure 2.5 are commonly found in literature and generally show two important features influencing the fuel cell performance. The slope of the line shows how much over-voltage (or over-potential) is required for a given increase in current density. Flat slopes are therefore desirable.
The dashed line shown in figure 2.5 are used to define the exchange current density, a metric for the activity in equilibrium. Table 2.3 lists the exchange current density for common catalysts used in SOFCs. From these tables and figures, as well as other considerations like cost and availability presented in this section, it is clear that nickel is still a viable candidate as a catalyst.

Catalyst	i_0 (A/cm^2)
Pb	2.5×10^{-13}
Zn	3.0×10^{-11}
Ag	4.0×10^{-7}
Ni	6.0×10^{-6}
Pt	5.0×10^{-4}
Pd	4.0×10^{-3}

Table 2.3 - Exchange current densities for metallic catalysts used in fuel cells

Within a SOFC environment, these specifications are largely abandoned. The nickel is no longer supported on aluminium or magnesium. The most common support for anode supported SOFCs is yttrium stabilised zirconia (YSZ), but many other materials have been proposed and tested. For this thesis, only YSZ is considered as a support material.

Several transition metals have been considered as catalyst for SOFCs. From first principles, the following metals are valid candidates; Au, Ag, Cu, Pt, Pd, Ni, Co, Ru and W. Most of these metals have been eliminated, for different reasons. The energy diagrams of noble metals show that they are not suitable to facilitate the steam reforming reaction effectively. This excludes Au, Ag and Cu.
Wolfram binds strongly with carbon and oxygen radicals, resulting in carbon deposition rates that can be mitigated.
Platinum and palladium are unfavourable in the adsorption and desorption of water. These materials are also very costly, and the commercialisation of SOFCs is most likely not possible if the anode side is solely reliant on these expensive materials.
Long term durability and stability of Co catalyst are at risk due to the poisoning by O and OH surface species. These species accumulate over time and permanently occupy site species needed for the reforming process (van Beurden, 2004).

This leaves Ni and Ru as potential catalysts for the steam reforming reaction. It should be noted that combinations of these, and other metals are valid options as well. One of the major issues for internal steam reforming at the conditions found in SOFCs, is that the reforming reaction rate is very high. This fast reaction rate is caused by excessively high nickel content on the anode surface, which is needed to achieve high enough electrical conductivity. The fast kinetics for the steam reforming reaction resulting from this design choice cause several issues. Large temperature gradients are present inside the fuel cell, due to the endothermic nature of the steam reforming process, and the exothermic nature of the electrochemical processes. This leads to significant temperature drops just after the inlets and temperature peaks near the outlets of the channels inside the fuel cell. These thermal stresses cause fractures in the YSZ support material, which leads to oxygen spillover. Local sintering and degradation of catalytic materials is also observed, which is sometimes linked to unexpected temperature peaks caused by the large amount of catalytic sites.
To mitigate these and other undesirable effects of pure nickel as the catalyst in SOFCs, other combinations of catalytic material have been tested. For example, Cu-Ni catalysts have shown overall high performance in internal reforming SOFCs. The copper surface will not promote the

steam reforming reactions, but is an excellent electrical conductor. Experiments with Cu-Ni catalysts have shown that cell degradation caused by thermal damage, and even catalyst poisoning by carbon and sulfur, is significantly reduced. The authors (Z. Wang et al., 2008) have encouraged the readers to investigate more, and stressed that the proper preparation of the catalyst is critical, since pure copper will melt in typical SOFC conditions. There are many other examples of hybrid catalytic materials that have shown promising results with respect to stable longterm power output, without sacrificing power density. Elaborating on all possible combinations, tested and untested goes far beyond the scope of this thesis.
Besides the use of a nickel alloy catalyst, adding steam also helps in the desorption of carbon. In chapter 4, a detailed explanation on the basis of thermodynamics is given.

The nickel (alloy) must be deposited on a substrate material. For convenience, the most popular substrate is the same material as the electrolyte, yttrium stabilised zirconia (YSZ). The strategy of choosing the same material for the anode substrate and the electrolyte is common, since the two layers will subsequently have similar material properties. For instance, nickel and YSZ differ somewhat in thermal expansion coefficient, but a Ni-YSZ cermet is much more similar.

As a concluding remark, the anode layer is usually the thickest layer, providing structural strength to the layered assembly. The added width allows this layer to be porous as well, and the entire surface of this layer is covered in nickel crystallines. This type of SOFC is also referred to as 'anode-supported'. This is currently one of the most researched types of ceramic fuel cell. Fuel cells that are commercially available from manufactures such as Bloom Energy, are most often electrolyte supported.

CATHODE MATERIALS

The most important function of material at the cathode side of the electrolyte is to reduce oxygen to negatively charged ions. In order to facilitate this electron transfer, the electronic conductivity must be as high as possible. The material must have chemical and dimensional stability to withstand conditions both in production and in operation.
The microstructure must also enable diffusion of gaseous oxygen into the material. This is usually achieved by enlarging the specific surface area, resulting in a porous medium.
Cathodic materials that have been successfully used in SOFCs in longterm experiments are both noble metals, and conducting perovskite oxides. For high temperature SOFCs, the most common material used is ($LaMnO_3$), substituted with elements like Sr or Ca. These elements promote p-type electronic conduction and enhance the activity for oxygen reduction. Doping the lanthanum manganite with Sr (LSM), gives the best performing cathode material for high temperature SOFCs. The conductivity is 10^{-7} S/cm at 800 °C, and this improves with increasing temperature.

At temperatures below 600 °C the performance is limited. Other cathodic materials have been proposed and tested. Lanthanum based perovskites, in combination with transition metals such as Ni, Fe or Co are still being developed. The durability of some of these compounds is still an issue.

Compared to the anodic side of a fuel cell, the cathode material is less prone to failure. This is mostly due to the fact that no carbon deposition will occur on the cathode side. For this thesis, no detailed cathodic surface mechanism is employed. Furthermore, thermal and chemical stability on the cathode side is assumed, using global material properties of LSM.

ELECTROLYTE MATERIALS

The electrolyte material is subjected to both an oxidising and reducing environment on the cathode and anode side respectively. To ensure sufficient lifetime the electrolyte material must have the following material properties.

1. Sufficient ionic conductivity; the ionic transference number must be close to unity, which also means that the electronic conductivity is near zero. This is crucial for reaching a satisfactory energy conversion efficiency. Finally, the conductivity for oxide ions must be as high as possible without giving in to the other listed requirements. This is necessary for minimising the ohmic losses in the cell.
2. Dense structure; no gasses must be able to permeate through the electrolyte layer. The electrolyte layer must be kept as thin as possible in the mean time, since the layer thickness is proportional to the ohmic los in a cell.
3. Stable microstructure; the structural consistency must be maintained at temperatures up to 1000 °C, in both oxidising and reducing environments. The thermal expansion coefficient must also match with the surrounding interfaces.

The materials suited for these demanding requirements are often oxides with low valence element substitutions, which create oxygen vacancies. Yttrium stabilised zirconia (ZrO_2) (YSZ) is the most commonly used material in SOFCs. Other materials such as enhanced CeO_2 and perovskite structured oxides have also been tried and tested. Figure 2.6 shows that the ionic conductivity for the latter materials is much higher at all temperatures. Only YSZ however has shown to be stable for long times at 1000 °C. The other electrolyte materials might be suitable for intermediate temperature SOFCs, and a lot of literature is available on the improvement of these materials. This lies outside the scope of this thesis.

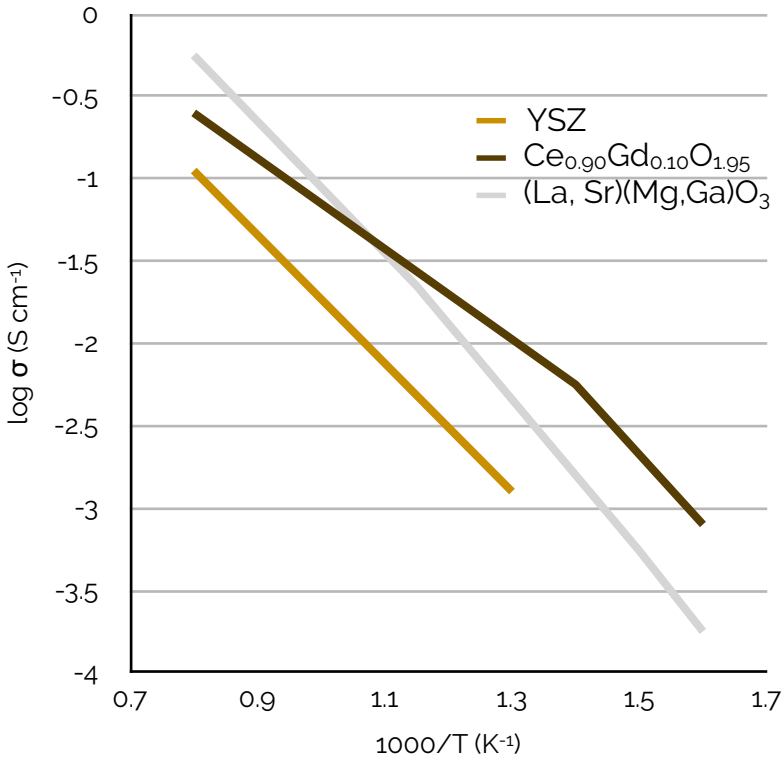

Figure 2.6 - Temperature dependant conductivity for YSZ, gadolinium doped CeO_2, and LSMG

MATERIAL SELECTION FOR THE MODEL

The model in this thesis will consist of a Ni-YSZ anode, combined with a YSZ electrolyte and a (traditional) $LaMnO_3$ cathode. Even though more advanced materials are available, this conventional setup is selected for several reasons.

Firstly, the selected materials are very well documented. As shown in this section, some sources on nickel catalyst date back almost a hundred years. Replication studies throughout the years have corrected some erroneous material properties reported in several texts. By selecting conventional materials, uncertainties surrounding the material properties are reduced as much as possible.

Secondly, the purpose of these advanced materials is often to enhance the fuel cell efficiency or performance as well as to improve the lifespan of the fuel cell. These multi-purpose material studies do not lend themselves very well as comparison to a modelling study. Furthermore, verifying these efficiency gains lies outside the scope of this thesis.

2.5 - Scale and cost of SOFC systems

SOFC systems are already commercially available. This section contains a brief overview on the type of systems that are being developed. Afterwards, the financial competitiveness of SOFC systems is compared to PEM fuel cells and conventional power generation. Solid oxide fuel cell systems that are not optimised for cost are already a viable alternative, provided the 40,000 hour lifespan can be reached (Blum et al., 2015).

The cost of a fuel cell system in combination with the projected lifetime is an important figure for the economic viability. Cost reductions in other parts of the fuel cell system may lead to a shorter required lifespan. For this reason it is important to state the current state of the technology.

PORTABLE SYSTEMS

Portable systems, producing power in the 50 to 250 W range are being developed to provide off-grid power for the military. These systems are also suited for small unmanned vehicles and drones.

PEM fuel cells were first implemented on theses scales, due to their more manageable operating temperatures. However the fuel flexibility of SOFCs, that don't require hydrogen, has been the primary reason to develop these systems.

A special system requirement for these type of systems is a satisfactory fast start up time. This can be achieved by using a tubular design with many small diameter tubes. This geometry is much better resistant to thermal shock.

Currently, these devices run mostly on propane, LPG or JP-8 military fuel. Lifespan and carbon deposition are no critical issues yet, as these devices serve as emergency short term power supplies.

TRANSPORTATION SYSTEMS

Fuel cells are being developed to replace the internal combustion engine in vehicles, trucks and ships. For the first two SOFCs have not been particularly successful, since the required power ranges (10 - 80 kW) requires large additional control systems that quickly become too bulky to put in a nimble electric town car. PEM fuel cells have been more successful on this front, clearly indicated by the fact that several hydrogen powered cars are commercially available.

The near future for SOFCs in transportation systems lies with even larger systems, replacing diesel engines in ships. In addition, smaller auxiliary power units (APU) in the 3 - 5 kW range are being developed to power secondary luxury systems in trucks and motorhomes, such as refrigerators, and microwaves.

RESIDENTIAL COMBINED HEAT AND POWER APPLICATIONS

SOFC systems designed for residential applications are being developed all over the world. These devices usually run on natural gas and provide 1 - 5 kW to a residential building. These type of systems have been deployed in Switzerland, the UK, Japan, the USA and Canada.
A major benefit of combined heat and power (CHP) systems is that the SOFC can provide heat and electrical power to a building.

LARGE SCALE POWER GENERATION

In order to replace coal firing plants, large scale systems are being developed. The power output for a single module is generally in the range of 100 - 200 kW. The modular design of SOFC systems makes it possible to install multiple modules in parallel. The first cogeneration system of 100 kW was fuelled by natural gas (where extra measures were taken to remove sulfur) and ran for nearly 40,000 hours with an overall efficiency of 46%. These tests occurred in the early 2000s. Later, systems with higher efficiencies, but worse durability where also tested.
Since then, Bloom Energy has launched several MW sized system, consisting of modules with a 200 kW capacity each. The initial efficiency of these systems is over 65%, but long term efficiencies are harder to find. These systems must ultimately compete with traditional power plants, which means that similar lifetime and cost effectiveness must be obtained.

PROJECTED COST OF LARGE SCALE SOFC SYSTEMS

An extensive study (Battelle, 2016) lists cost, economies of scale and profitability of large scale SOFC systems using the knowledge and input of many manufacturers. Both 100 kW and 250 kW systems have been investigated.

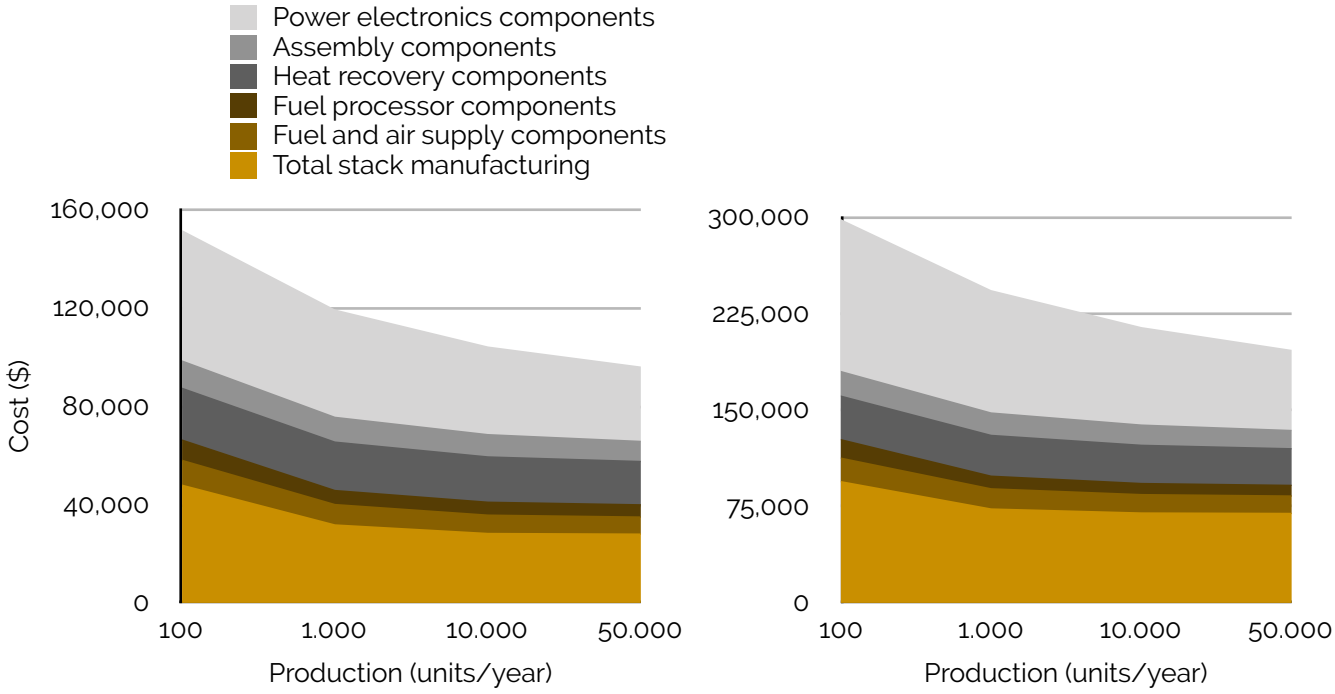

Figure 2.7 - Cost volume trends of 100 kW (left) and 250 kW (right) SOFC systems (adapted from (Battelle, 2016))

The total costs of these systems is shown in figure 2.7, figure 2.8 shows the resulting cost per generated kW. Although these numbers may vary significantly, for example by fluctuating material prices and deviating labor costs for differing countries, the underlying trends of scaling up SOFC technology become visible by these kind of studies.

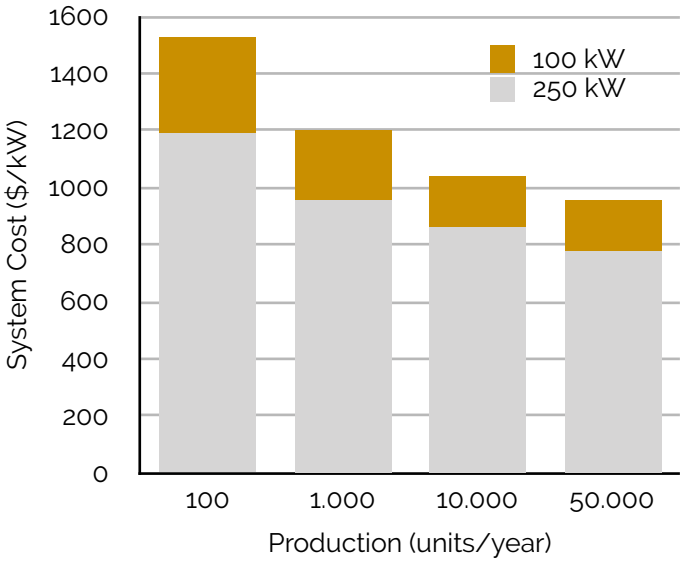

Figure 2.8 - System cost per kW for 100 and 250 kW SOFC systems (adapted from (Battelle, 2016))

A complete analysis for investing, implementation and operating cost and eventual return on investment is also provided. From this analysis, the profitability and the internal rate of return for SOFC systems can be calculated.
The results are compared by similar sized PEM fuel cell systems in table 2.4. Compared to PEM systems, SOFC systems are now projected to be more cost effective.
The authors of this report also identify the long term durability of SOFC systems to be the last practical hurdle that needs to be taken before large scale implementation is possible.

	PEM	SOFC	PEM	SOFC	PEM	SOFC	PEM	SOFC
System Production Rate	100/year		1000/year		10.000/year		50.000/year	
100 kW								
IRR after 5 years	4%	28%	14%	41%	21%	49%	25%	56%
Payback period (years)	4.44	2.47	3.40	1.95	2.91	1.71	2.64	1.56
250 kW								
IRR after 5 years	10%	38%	20%	51%	28%	59%	33%	66%
Payback period (years)	3.77	2.08	2.93	1.69	2.49	1.49	2.24	1.36

Table 2.4 - IRR of 100 and 250 kW PEM and SO fuel cell systems (adapted from (Battelle, 2016))

REQUIRED LIFE SPAN FOR SOFC SYSTEMS

At the beginning of this chapter, a required lifespan of 40,000 hours was quoted to reach economic viability of SOFC systems. Preventing carbon deposition and other cell degradation during this time is the technical challenge engineers are facing.

Since carbon deposition is a particularly complex problem it will be very likely it is never solved altogether. Therefore, we briefly consider another way to reach economic viability.

Table 2.4 shows that SOFC systems become much cheaper on a unit basis when enough systems are produced. This shortens the payback period considerably.

From an investors point of view this economy-of-scale mechanism is very attractive, since marginal cost reductions typically end up in their pockets. However, one could argue that a shorter payback period may alleviate the required lifespan of the system somewhat.

In other words, internal reforming SOFC may already be economical viable when a large enough investment is made.

3 - Challenges of SOFC design

Reasons why solid oxide fuel cells (SOFCs) aren't as prevalent yet in commercial applications, can be classified in reliability and lifetime issues. These challenges are explored in this chapter. The main focus here lies with challenges emerging when fossil fuels are used as a fuel either in a pure form, or in conjunction with hydrogen. In line with the scope of this thesis, carbon deposition is discussed first and foremost. Other factors limiting the lifetime due to the addition of fossil fuels are treated next. More general challenges that are relevant for high temperature internal reforming (IR) SOFCs are also discussed, as these failure modes might limit possible mitigation strategies for carbon deposition.

3.1 - Fuel compositions

Thermodynamic studies investigating the thermochemical stability of fuels mixed with water and additional hydrogen can be used as a solid starting point for mitigating carbon deposition. The straight forward concept here is, when it is thermodynamically impossible for solid carbon to form, little to no carbon deposition will be observed.
These analyses are performed by assuming a certain gas composition is perfectly mixed inside a reactor at a certain temperature. The final gas composition is in chemical equilibrium when the Gibbs Free energy is minimised. Figures 3.1 and 3.2 show two ternary diagrams. These type of figures can be used to illustrate mixtures of only three different atoms. Figure 3.1 shows where on this kind of diagram some common fuels for SOFCs fall. Figure 3.2 shows that practically all fuels types lie in the region where carbon deposition will occur. At higher temperatures, this becomes more prevalent (Takeguchi et al., 2002). A common solution is to add steam to the mixture. As can be seen from figure 3.2, adding steam will 'pull' a mixture below the lines indicating whether carbon deposition is thermodynamically favourable. For carbon heavy molecules, that lie deeper inside the carbon deposition region, more steam will need to be added (K. Sasaki & Teraoka, 2003).

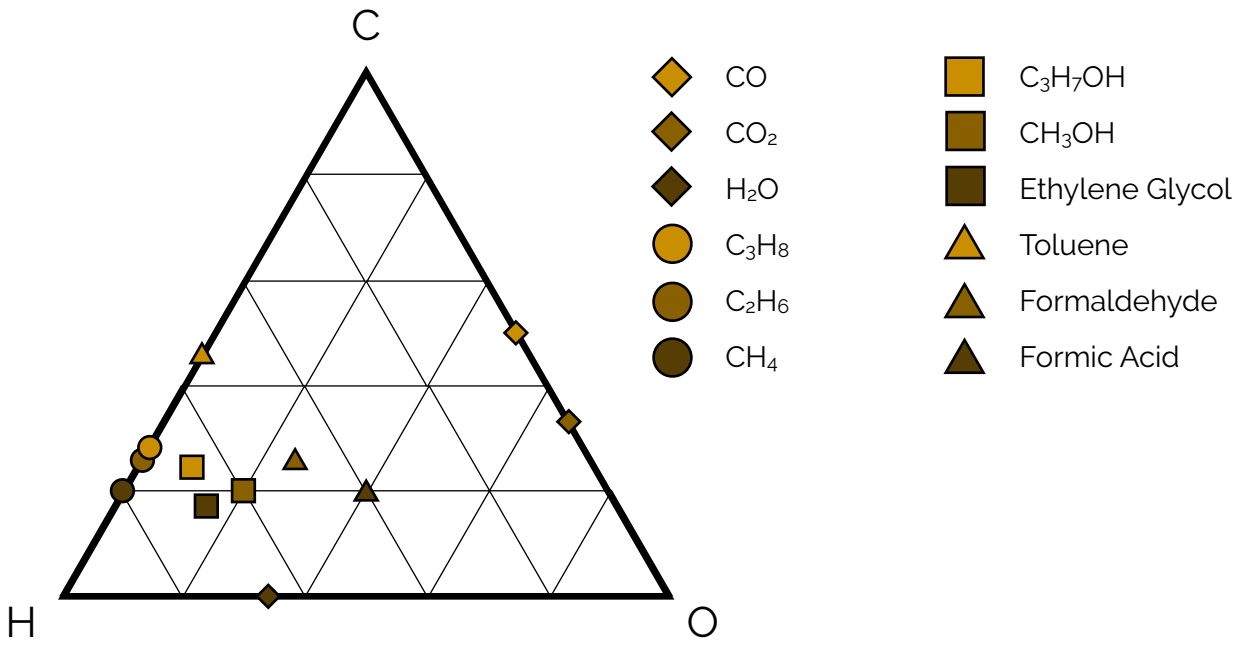

Figure 3.1 - Ternary diagram for C-H-O based fuels for solid oxide fuel cells (adjusted from (Takeguchi et al., 2002))

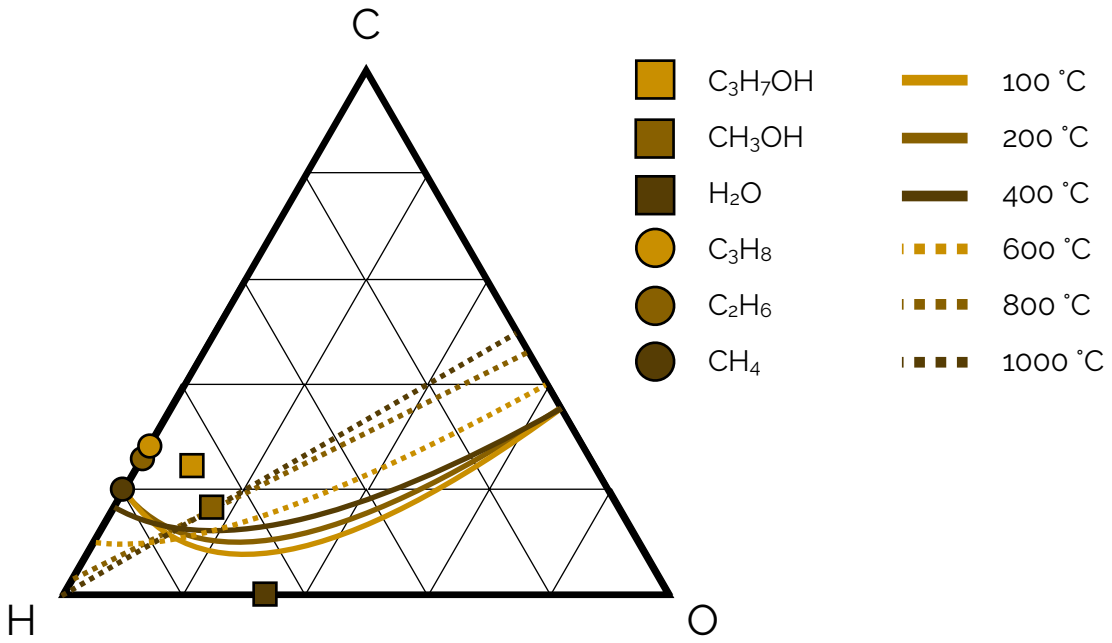

Figure 3.2 - Ternary diagram indicating region where carbon deposition is favourable (adjusted from (Takeguchi et al., 2002))

For methane, a steam to carbon ration (S/C) of 1.5 or higher is required in order to prevent carbon deposition. At higher temperatures, (800 °C - 1000 °C) this is somewhat reduced to 1.1. For hydrocarbons with higher carbon numbers, the S/C-ratio increases as well. For alcohols like C_3H_7OH and C_2H_5OH at increased temperatures, the S/C-ratio can drop below unity. For CH_3OH, the required S/C-ratio at 1000 °C is zero. This has sparked interest in using alcohols as a fuel instead of methane or other hydrocarbons (Laosiripojana & Assabumrungrat, 2007; Liso, Cinti, Nielsen, & Desideri, 2016).
These thermodynamic analyses on mixtures cannot be fully relied upon. Fuel cells are devices that do not operate at equilibrium conditions. Studies have observed carbon deposition using methane as a fuel with S/C-ratio higher than 1.5. For this reason, experiments and numerical simulations not relying on chemical equilibrium calculations are considered more powerful methods for accurately describing fuel cell behaviour (Koh, Kang, Lim, & Yoo, 2001).
It should also be noted that these diagrams are only valid when no other constituents like sulfur and nitrogen are present. In practice, some contaminants will always be present in real fuels.

3.2 - Power output characteristics

The fuel composition alters the I-V characteristics of a solid oxide fuel cell. This is important later on when discussing other failure mechanisms, that bear some relationship to the slope of the I-V curve for example.
The experimental results shown in this section will be useful for the next chapters where assumptions are made for the open cell potential. Finally, the I-V curves shown here will be used in chapter 6 where the final model is validated.
The fuel cells used in these experiments all contain nickel-based cermet anodes and zirconia-based electrolyte material, and all the experiments took place at 1000 °C. This study (K. Sasaki et al., 2002) has conducted experiments investigating the effects of a varying H_2 to CO ratio. Relevant results from this study are shown in figure 3.3a. This graph shows that CO-rich gas behaves

similarly to H_2, albeit at a slightly lower operation voltage. During the methane reforming proces H_2 and CO are formed. Both product gases will ultimately be used for generating power.
Another study compared the performance of alcohols with reformed gas (K. Sasaki, 2003). The most interesting result with respect to the scope of this thesis, is the I-V curve for reformed gas. This I-V curve reveals an experimentally verified open-circuit voltage (OCV) at zero current density. For reformed gas, this is 1050 mV, which is larger than the OCV for a standard SOFC running on pure hydrogen. This OCV can be read from figure 3.3a, and is just 960 mV. The general shape is also useful, and will be used to verify results from this model.

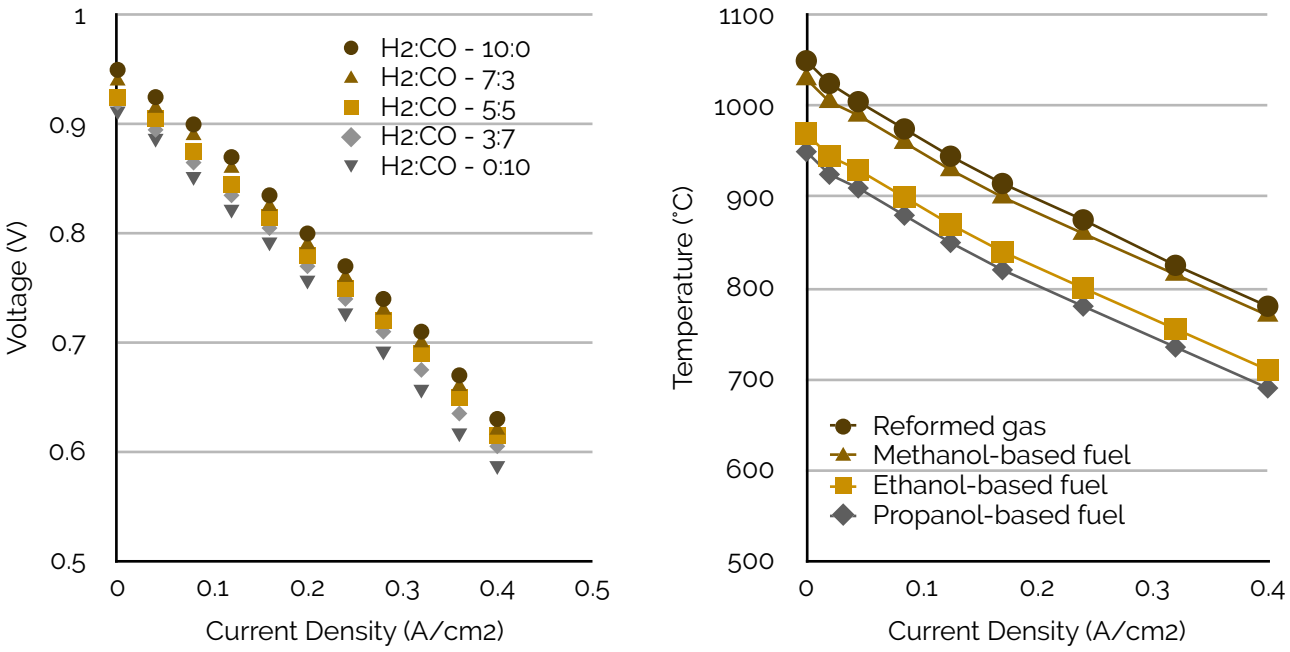

Figure 3.3a - I-V characteristics for different H2 : CO ratios
Figure 3.3b - I-V characteristics for reformed gas and alcohol based fuels.

3.3 - Fuel impurities

Fuel impurities hamper the ultimate lifetime and reliability of fuel cells. Before considering the specific failure mechanisms, the origin of these impurities is explored first. The source of specific pollutants will clarify why it might be impossible to get rid of. Other solutions then 'improving filtering processes' and 'ensuring a pure reactant stream' must be given in these cases.
Cell performance degradation can be categorised in three groups. Anode and cathode poisoning, as well as general cell contamination.

ANODE POISONING

In the case of IR SOFCs, anode poisoning is generally most predominant and critical. Pollutants enter the fuel cell along with the fuel. Depending on the origin of the methane and steam feed stream, other impurities may be present as well. Steam that is created from waste streams may contain siloxane and aromatic compounds. At temperatures found in even intermediate temperature SOFCs, these compounds form graphene and ultimately coke. Methane will contain traces of sulfur, chlorine, boron, phosphorus and higher hydrocarbon compounds, depending of its origin. These impurities pose a threat to nickel based anodes, reducing the lifetime significantly in various ways. Figure 3.4 shows degradation mechanisms found on nickel based anodes in SOFCs (Kazunari

Sasaki et al., 2011). The adsorption mechanism is by definition reversible. Revitalising or recovering the anodic surface by 'flushing' the fuel channel periodically with an appropriate cleanser can extend the lifetime of the fuel cell indefinitely. Sublimation mechanisms are more destructive. The catalytic material is broken down and is lost to the outflowing fuel stream. Chlorine poisoning is a known cause of nickel sublimation, forming $NiCl_2$. Severe carbon deposition may cause another type of sublimation mechanism, where the nickel is pushed out by growing carbon nanotubes. Deposition mechanisms cover active catalytic sites. Carbon formations in various phases, as well as siloxane and sulfur can cause irreversible depositions on nickel anodes.
Finally, some pollutants can chemically alter the nickel sites of the anode. At relative high sulfur concentration a Ni_2S_3 layer is formed, preventing hydrogen to react with oxygen ions coming through the electrolyte. Grain growth in nickel granulates caused by boron reduces the activity of cermet anodes. Phosphorus can react with nickel to form a eutectic compound, seriously inhibiting the diffusion of hydrogen to a site where the reaction with oxygen ions takes place.

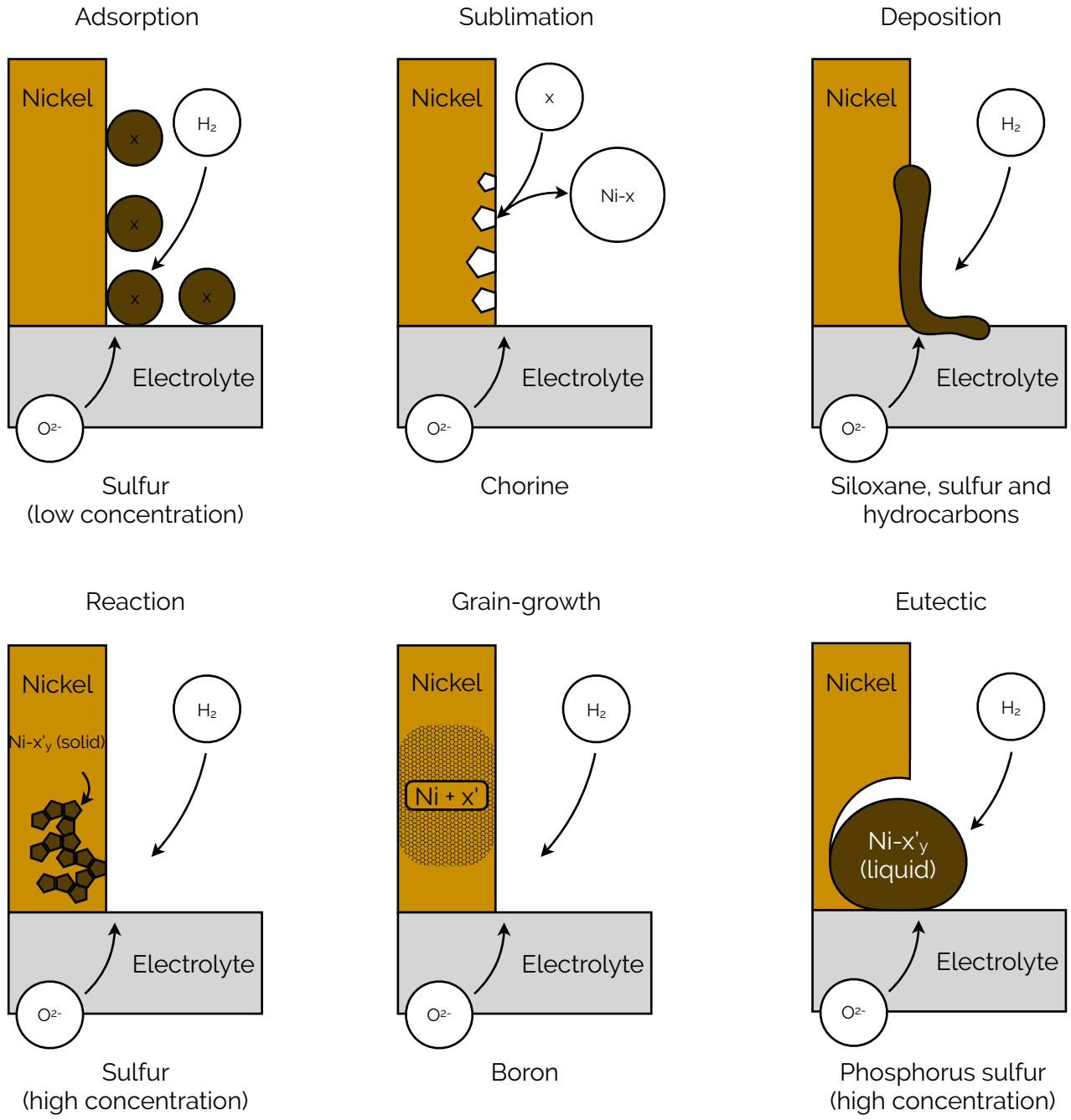

Figure 3.4 - Types of anode degradation mechanism found in SOFCs

It is clear from this figure that sulfur is involved in four of the six degradation mechanisms. Internal reforming SOFCs running on methane will have to deal with traces of sulfur. Premature fuel cell failure due to chemical processes is next to carbon deposition most often caused by sulfur poisoning.

The main reason for this is that sulfur is a poison to the catalytic activity of nickel. For long term stable operation, this is already a problem when sulfur concentrations reach the part per billion (ppb) range. Apart from long term stability, the initial cell potential of a single solid oxide fuel cell with a Ni-YSZ anode drops from 0.75 V to 0.7 V, when the H_2S concentration exceeds 300 ppb. This sulfur compound can form in the H_2 rich environment inside SOFCs, and originate from natural gas, LPG, gasoline, and other hydrocarbon based fuels prepared for fuel cells. The critical concentration of H_2S increases with temperature. Above the critical concentration, cell performance will start to deteriorate. Internal reforming SOFCs operating at intermediate temperatures are more sensitive to sulfur poisoning. It has been shown that the performance loss due to sulfur poisoning can be reversed up to 5 - 10 ppm concentrations. Beyond this point, nickel binds permanently with sulfur (Ni_3S_2), or the nickel surface sites are otherwise reformed resulting in a less active catalyst (Offer, Mermelstein, Brightman, & Brandon, 2009).
Another important insight is that sulfur poisoning can become more favourable near the outlet conditions, where most H_2 has been converted to H_2O. This can be illustrated in the phase diagram in figure 3.5. In conclusion, the skewed area enters the Ni_3S_2 region when the H_2S concentration increases and when H_2 concentration drops (right side of the shaded area). Finally, the same research shows that other nickel-sulfur compounds are not thermodynamically favourable in SOFC conditions. This can also be seen in figure 3.5.

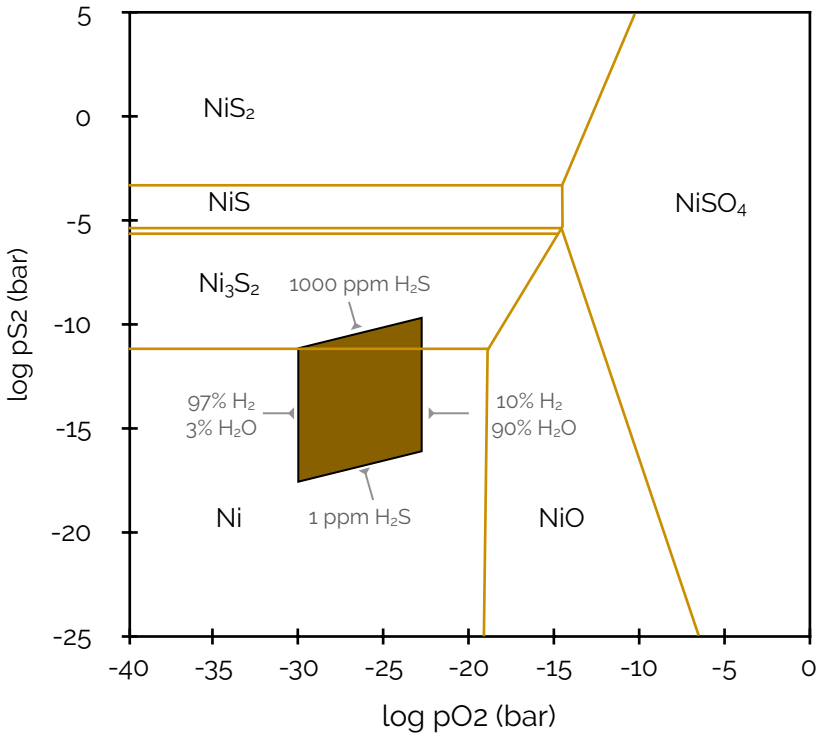

Figure 3.4 - Phase diagram for Ni-S-O systems at 600 ˚C (adapted from (Offer et al., 2009))

Mitigation of sulfur poisoning can be done by filtering the methane stream before it enters the fuel cell. The goal here is to lower the sulfur content to concentration levels where only adhesion occurs. This requires less filtering and any performance degradation caused by sulfur can be recovered (Skafte, Blennow, Hjelm, & Graves, 2018).

CATHODE POISONING

Cathode poisoning in SOFCs has been observed in some cases. Sulfur dioxide (and other SO_x compounds) is sometimes present in higher concentration than average atmospheric conditions, for instance near power plants and other large industrial sites. The sulfur compounds poison the cathode in this case, diminishing the absorbance of oxygen over time. It has been reported that salt containing fog near sea shores can have the same effect, as well as humidity in ambient air.
From the examples given, it is clear that cathode poisoning is less of an issue for IR SOFCs. Simply selecting an appropriate location for the fuel cell system can solve most problems. Controlling the humidity and filtering irregular atmosphere content to a suitable level is also well within possible means (Xiong et al., 2009).

GENERAL CELL CONTAMINATION

Cell degradation due to impurities and other malevolent compounds may not originate from either fuel stream nor air stream. In these cases, the constituents originate from the fuel cell system itself. The oxidative environment at elevated temperatures can cause heat- and electrical insulating materials to evaporate. Bonding materials, supply tubes and other structural components may be potential sources for contaminates as well. Especially cheaper and/or low quality materials may contain traces of sulfur and phosphorus compounds. (Yokokawa, Watanabe, Ueno, & Hoshino, 2019). When evaporation occurs, similar degradation might be observed as with impurities from the fuel stream. In this case the decay in performance is sometimes temporary, since the total amount of impurities in the exposed materials are finite.

ALLOWABLE IMPURITY CONCENTRATION THRESHOLDS

In order for SOFCs to obtain a reasonable lifespan, experiments have been conducted to find the allowable tolerances for specific impurities listed above. A common target for future SOFCs is 40.000 hours, with a 1/4% per 1000 hours voltage drop. Table 3.1 provides an overview. Some of these values originate from button cell experiments (K. Sasaki et al., 2013), and some of these findings have been corroborated on larger fuel cell systems.
In these experiments, the initial degradation rate in the first 1000 hours has been linearly extrapolated. Additionally, they assumed the measured degradation rate depends linearly on the impurity concentration. So the listed impurity concentration limits are somewhat primitively construed, since they do not account for any non-linear effect or deviating long-term changes in degradation rate.

Impurities	Impurity threshold with corresponding operation conditions	
Sulfur (S) - H_2S, COS, CH_3SH	700 ppb	50%-Pre-reformed CH_4 fuel at 800 ˚C
Chlorine (Cl) - Cl_2, HCl	400 ppb	3%-Humidified H_2 fuel at 800 ˚C
Phosphorus (P)	3 ppb	3%-Humidified H_2 fuel at 800 ˚C
	2 ppb	50%-Pre-reformed CH_4 fuel (S/C = 2,5) at 800 ˚C
Boron	5 ppb	3%-Humidified H_2 fuel at 800 ˚C
Siloxane	2 ppm	3%-Humidified H_2 fuel at 800 ˚C
	4 ppm	Air (dry) for $La_{1-x}Sr_xMnO_3$
Sulfur (SO_2)	0,5 ppm	Air (dry) for $La_{1-x}Sr_xCo_{1-y}Fe_yO_3$

Table 3.1 - Allowable impurity concentration for projected lifetime of 40.000 hours

3.4 - Carbon deposition

Carbon deposition in the context of IR SOFCs is a general term for solid carbon formations on the anode, reducing and ultimately blocking the operation of the fuel cell. This is the most destructive and critical failure mechanism, and therefore lies at the centre of this thesis. This section will provide a comprehensive picture on the current understanding of this phenomenon.
First some important perspectives from the field of thermodynamics are discussed. Afterwards, several theories developed in conjunction with experiments are considered as well. These proposed theories with accompanying mechanisms on carbon deposition on nickel anodes have become widespread, and can be divided in two categories.

Primary carbon deposition mechanisms are based on the reforming of a hydrocarbon. In a nutshell, the rate of carbon deposition is determined by the type of fuel, and other process parameters such as temperature, pressure and fuel composition. When these parameters are kept constant, a constant rate of carbon deposition will be observed. Many short term studies report a seemingly linear increase carbon content of 0.04% by weight after only 10 hours (Rakass, Oudghiri-Hassani, Rowntree, & Abatzoglou, 2006). Another study investigating the carbon deposition rate on temperature showed similar linear behaviour for short times for all temperatures (Watanabe, Okino, & Hanamura, 2019).

Secondary carbon deposition mechanisms are caused by changes within the reforming reactor. These phenomenon are often encountered in longterm studies. Due to specific conditions inside the fuel cell, the catalytic material undergoes a change in geometry and composition that increases the rate of carbon deposition over time. Especially changes in geometry of the catalyst layer carry inherent non-linear behaviours (Davis & Haataja, 2017). For IR SOFCs, the length of the triple phase boundary (TPB) is a key parameter for the catalytic activity, depending on the same geometry. Figure 3.5 shows schematically, how a total rate of carbon deposition might manifest as a combination of a constant and an (non-linearly) increasing rate.
The remainder of this section will discuss several theories and associated mechanisms found in literature. Experimental results have strengthened the position of some of these mechanisms, but no real consensus has been reached.

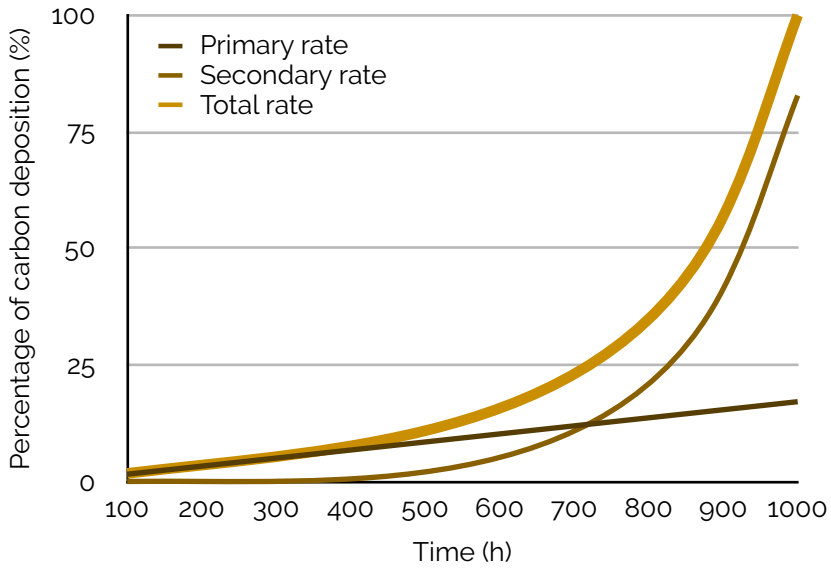

Figure 3.5 - Schematic rate of carbon deposition caused by a combination of primary and secondary mechanisms

CARBON DEPOSITION FROM REFORMING HYDROCARBONS

Carbon formation originating from the reforming process of hydrocarbons is in IR SOFCs the most prominent cause of degradation and cell failures, sometimes even within several hours of operation. Carbon formation can have many consequences for the fuel cell performance. Carbon might break up the nickel sites, block the most active radicals near the YSZ/Ni edges, and might even block the gas flow altogether.

Many theories and mechanisms to model each type of formation have been developed. The starting point for each of them is the initial adsorption of carbon. A combination of two commonly used mechanisms are shown in figure 3.6.

The compounds shown in brackets in figure 3.6 are surface species that can easily be dissolved into the gas phase. The occurrence of these surface species is inevitable when methane (or any other hydrocarbon) is used as a fuel.

Apart from catalytic surface reactions, carbon deposition can also originate from free radical gas phase condensation. This occurs at higher temperatures, starting from around 800 °C.

Once the carbon has been deposited as a single site species, it can alter the material on which it forms. Many mechanisms have been identified, but the two most important type of carbon formations for SOFC research are that of amorphous char (550 °C - 725 °C) and whisker carbon (>450 °C) (Figueiredo, 1986).

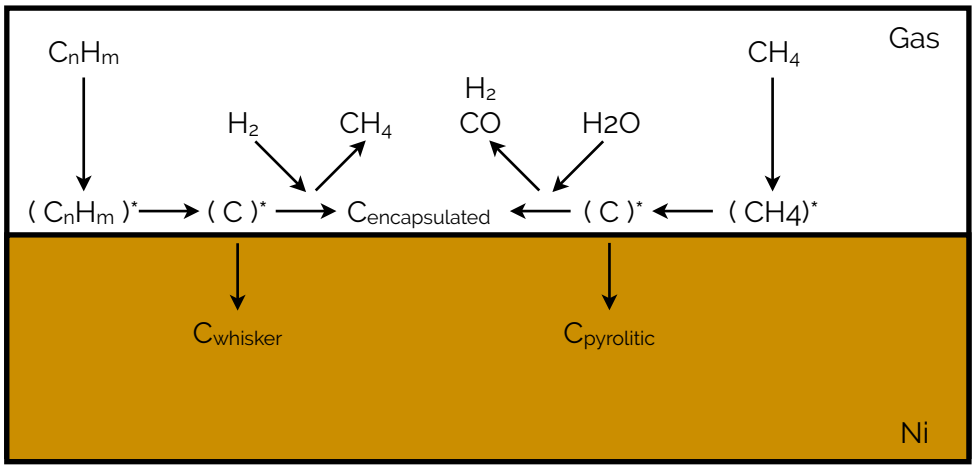

Figure 3.6 - Combined mechanisms for hydrocarbon adsorption on nickel (adapted from (Figueiredo, 1986)) and methane reforming on nickel (adapted from (Rakass et al., 2006))

These findings come from experiments (Bartholomew, 2001) that revolve around nickel catalyst samples that have been exposed to a carbon rich fuel stream, most often methane. Afterwards, these samples are analysed to find out what type of carbon is present on the sample. This is done by "burning" of the carbon with a heated oxygen stream. The temperature is gradually increased whilst monitoring the output gas composition using some kind of mass spectrometer. This is called Temperature Programmed Oxidation (TPO). By calculating the surface underneath the peaks it is also possible to estimate how much of each type of carbon was present. Furthermore, an average rate of deposition for each type of carbon can be determined by dividing the amount of carbon by the residence time the sample was exposed to the carbon rich fuel stream. An important conclusion here is that the deposition rate of carbon is dependant on temperature and time. Generally, higher temperatures will result in more dense graphite (whisker) carbon.

Experiments have shown that the interface where the crystalline nickel borders on the zirconia cermet is most susceptible for initial carbon adsorption (Watanabe et al., 2019). This is consequently

where most carbon formations start to form. Depending on the process parameters, three types of carbon formation are often encountered within reforming SOFC systems.
Encapsulating carbon formations consists of a polymeric carbon film. The process where these polymeric structures form only occurs at intermediate temperatures. Elevated temperatures beyond 500 °C will prevent this polymerase. In the scope of this thesis, no other prevention techniques are required to prevent encapsulation carbon further.

Whisker carbon formations are the most destructive and most complex to model accurately. Carbon that has been initially adsorbed at the surface can diffuse into the nickel and eventually end up underneath the crystalline structure on the cermet. The combined local pressure and temperature allows for the formation of carbon nanotubes, gradually lifting the nickel crystal from the cermet. The particle is electrically isolated from the fuel cell and rendered useless. Obviously, the shifted nickel particles are not recoverable. Whisker formation may occur in reforming SOFCs when temperatures exceed 450 °C, so special care must be taken to prevent this type of carbon formation.
A common chosen strategy for preventing whisker formations is to add other species to the nickel catalyst. Insights in material studies (Natesakhawat, Watson, Wang, & Ozkan, 2005) where nickel is doped with Al_2O_3 and CeO_2, has shown that CeO_2 might prevent whisker formations. The additional O_2 content inside the nickel particle oxidises the carbon and prevents further diffusion. Adding CeO_2 to a nickel catalyst however, reduces the activity for reforming methane. Studies are ongoing to find an optimum in CeO_2 content, estimates still vary between 1 - 5 wt% (S. Wang & Lu, 1998).
Other alloy materials such as $Ce_{0.8}Gd_{0.2}O_{2-x}$ are also being considered. The oxygen carrying alloying materials are chosen as an evolution from the research with CeO2, where an increase in activity for methane cracking is also achieved.

Another way for mitigating whisker carbon formation is by adding alkali promoters like K_2Al_2O. Carbon formation is positively influenced by low pH values on the catalyst surface. Nickel sites are positively charged in absence of sufficient alkaline species, enhancing both carbon diffusion into the crystalline structures, as well as carbon formations on the surface.
It has been shown that alkali-doped catalyst form hydroxide, with aid in the desorption or gasification of carbon. Experiments have shown that a 16% lower S/C ratio is required when catalyst with alkali promoters are present, compared to the same catalyst without K_2Al_2O (Carlsson, 2015). Just as with lanthanides doping, an excessive loading factor has the negative side effect of decreasing the catalyst activity. Even higher concentrations will cause nickel catalysts to corrode.

Pyrolytic carbon formation occurs at higher temperatures. Where the previous mechanisms relied heavily on the nickel sites and surrounding triple phases boundary, pyrolytic formations have been observed far outside the most active catalytic sites (Li, Shi, & Cai, 2011). This observation has caused uncertainty in the literature, on whether this mechanism is dependant on the presence of the metallic catalyst or not. In the latter case, pyrolytic formations are considered as non-catalytic (Li, Shi, & Cai, 2013). Most theoretical investigations agree that a free radical polymerisation reaction produces soot (Xu & Dang, 2016). This soot consists of spherical particles, that link together as more of it is produced. Eventually complex structures of carbon chains form, interchanged by larger crystalline formations. The specific features and appearance of pyrolytic carbon formations also depend on the porosity of the cermet and the local concentrations of hydrocarbon intermediates. This is an important point of attention, in order to prevent pyrolytic carbon formations in IR SOFCs, the intermediate surface species must be taken into account.
Methods for preventing pyrolytic carbon formations are similar to that of whisker carbon. Increased S/C ratio and preventing acidification of the nickel surfaces by adding alkali promoters are proven strategies to control the formation of pyrolytic carbon. Operation at elevated pressures has also led

to an increase in pyrolytic formations, so this is no longer recommended when satisfactory lifetimes are to be reached. Table 3.2 and figure 3.7 summarises this section.

	Encapsulating film	Whisker carbon	Pyrolytic Carbon
Formation	Gradual growth of C_nH_m chains on the nickel surface, encapsulating the surface with a film	Surface carbon diffuses through nickel crystallines. Whisker growth starts underneath crystal and lifts it from the cermet	Originates from the thermal cracking of hydrocarbons. Pyrolytic carbon forms from deposited carbon on the nickel surface, in combination with (local) high temperatures
Effects	Nickel sites are progressively deactivated	No deactivation of nickel for reforming. Electronically isolating the crystals, increasing ohmic resistance of cermet Structurally breaking down of catalytic layer Increasing flow resistance over channel	Nickel surface sites are encapsulated by a thicker graphitic layer of carbon Nickel sites are progressively deactivated Increasing flow resistance and pressure drop over channel
Temperature	< 500 ˚C	> 450˚C	> 600˚C
Crucial parameters	Relatively low temperature Low H_2O : C_nH_m ratio Low H_2 : C_nH_m ratio Aromatic feed	High temperature Low H_2O/C_nH_m ratio Low activity Aromatic feed	High temperature High void fraction Low H_2O : C_nH_m ratio High pressure Acidic catalyst

Table 3.2 - Overview on common carbon formations in reforming SOFCs

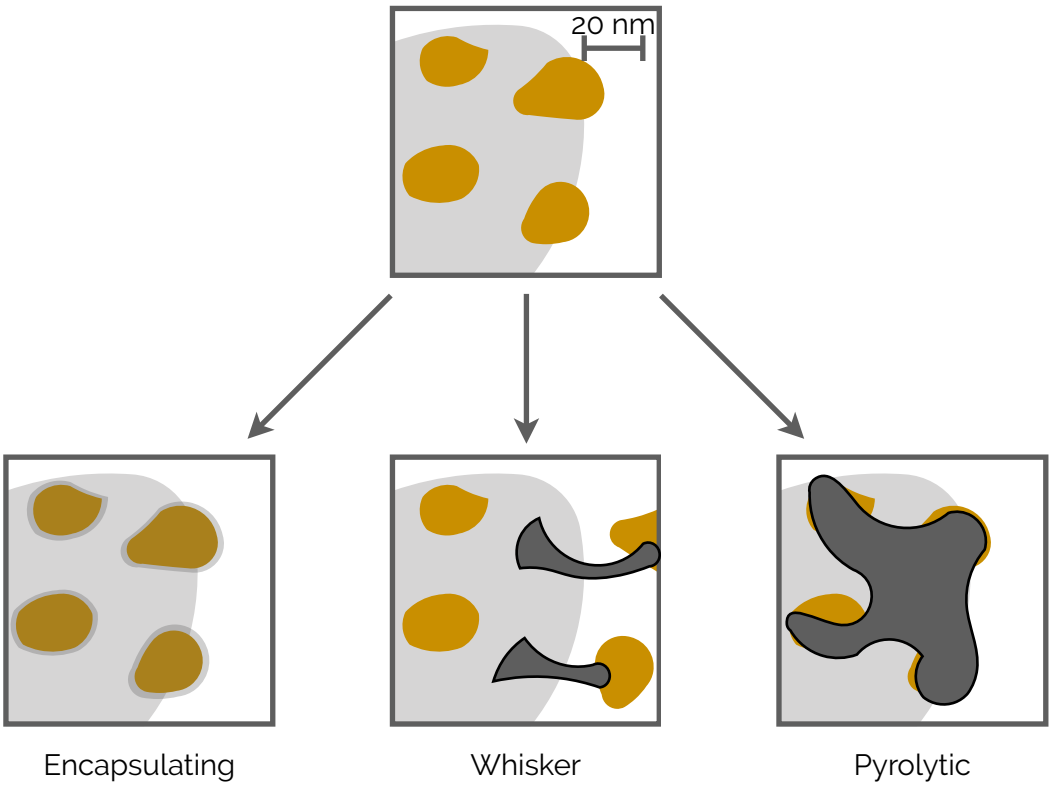

Figure 3.7 - Three common types of carbon formation on nickel in IR SOFCs

THERMODYNAMIC PREDICTIONS AND SHORTCOMINGS

By extending the same method by which the ternary diagrams in section 3.1 were produced, more predictions based on thermodynamics can be made. A common starting point is to display the equilibrium gas composition at a certain temperature and pressure. The equilibrium conditions are found by employing some kind of iterative solving technique to find the minimum Gibbs energy of a certain mixture. With these results, C-H-O ternary diagrams (figure 3.1 and 3.2) and composition plots for particular temperatures can be made. The MATLAB code for finding these equilibrium conditions is provided in Appendix A1, this was constructed by adapting a method from (de Jong, 2014). The equilibrium conditions change along the length of a fuel channel, as an increasing amount of oxygen is added proportional to the current density. At increments of 1 mm inside a 10 mm long channel, the equilibrium conditions were calculated using the same method.

The stream of oxygen ions was assumed to be directly proportional to the current density, and increasing the cell load above a certain threshold would eliminate solid carbon from the equilibrated mixture. Two critical assumptions in this model where the thermodynamic properties of carbon where taken in the condensed phase only, and the reaction where carbon oxidises to CO_2 takes place instantaneously. The existence of such a threshold has been confirmed by other experiments (Singh, Hernández-Pacheco, Hutton, Patel, & Mann, 2005).

A study using the same method (Koh et al., 2001) of Gibbs energy minimisation with Lagrangian multipliers predicted for IR SOFCs using methane, that the methane would crack, and form hydrogen and solid carbon. High amounts of carbon deposition would form accordingly, as predicted. They only considered the case of open circuit potential, so no additional oxygen was provided over the course of the channel.

Another study (Assabumrungrat et al., 2005) found thermodynamic equilibrium by relating the moles for each component to the equilibrium constants of the governing reactions. They predicted correctly that an increase in H_2 and O^{2-}-ons would mitigate carbon deposition. Hydrogen is converted to steam, which in turn shifts the water gas shift reaction towards CO_2. Consequently, less CO is now available to form solid carbon via the Boudouard reaction.

Another study (Singh et al., 2005) analysing carbon deposition in SOFCs using thermodynamic principles predicted that, with increasing temperatures, solid carbon formations will decrease. Comparing this to experimental data, for temperatures below 900 °C these predictions held. However, beyond this point carbon was deposited and this would increase with increasing temperature.

Here, defining a threshold current density was also pursuit at different other temperatures and steam contents. For a tar concentration of 1% and a steam concentration of 5% at a current density of 126 mA/cm^2, no solid carbon should form. Other experiments and models including reaction kinetics have shown otherwise (K. Sasaki & Teraoka, 2003). It seems that simple thermodynamic analysis can't predict accurately how much and even if carbon depositions would occur when all process parameters are known.

Modelling strategies that assume a mixture will instantaneously reach chemical equilibrium have one obvious shortcoming, the real rate of reaction is unknown. Even when the final composition of the mixture was correctly predicted, there would be no way of knowing when equilibrium conditions inside a reactor are reached.

Furthermore, a fuel cell in operation will never reach equilibrium conditions. This is why carbon formations form during experiments with gas compositions that should be free from any carbon deposition according to chemical equilibrium calculations.

UNSTEADY MECHANISMS THAN ENHANCE CARBON DEPOSITION

The elevated temperatures and oxidative environment inside SOFCs causes the catalytic material to deteriorate. Research as pointed to this change in catalytic material as a starting point for carbon deposition. The process where a metal clumps together due to temperatures approaching its melting point is called sintering. For nickel in SOFCs, this process occurs already at 500°C. Furthermore, water vapour accelerates this process even more. This is bad news, since adding water vapour is often offered as a solution to mitigate short-term carbon deposition.
Sintering influences the rate of carbon deposition since both are directly related to the particle size of nickel. As the sintering process increases the particle size, the total amount of TPB length decreases. The diminishing TPB length is often described by either of two mechanisms.

1. Particle migration, where entire crystallites migrate over the support and coalesce with larger crystallites.
2. Ostwald ripening, where individual atoms migrate through the support material or via the gas phase until they are captured by a larger crystallite.

The existence of both of these phenomena have been confirmed by experiments. By using a transmission electron microscope, both migrating and evaporating crystallites have been observed. Figure 3.8 summarises these findings. The processes observed here took place on a timescale of 60 seconds. The nickel particles depicted have a characteristic diameter of 10 - 40 nm (Sehested, 2006). It is important to note that the crystalline structures outside the dashed circle where unmoved during this time.

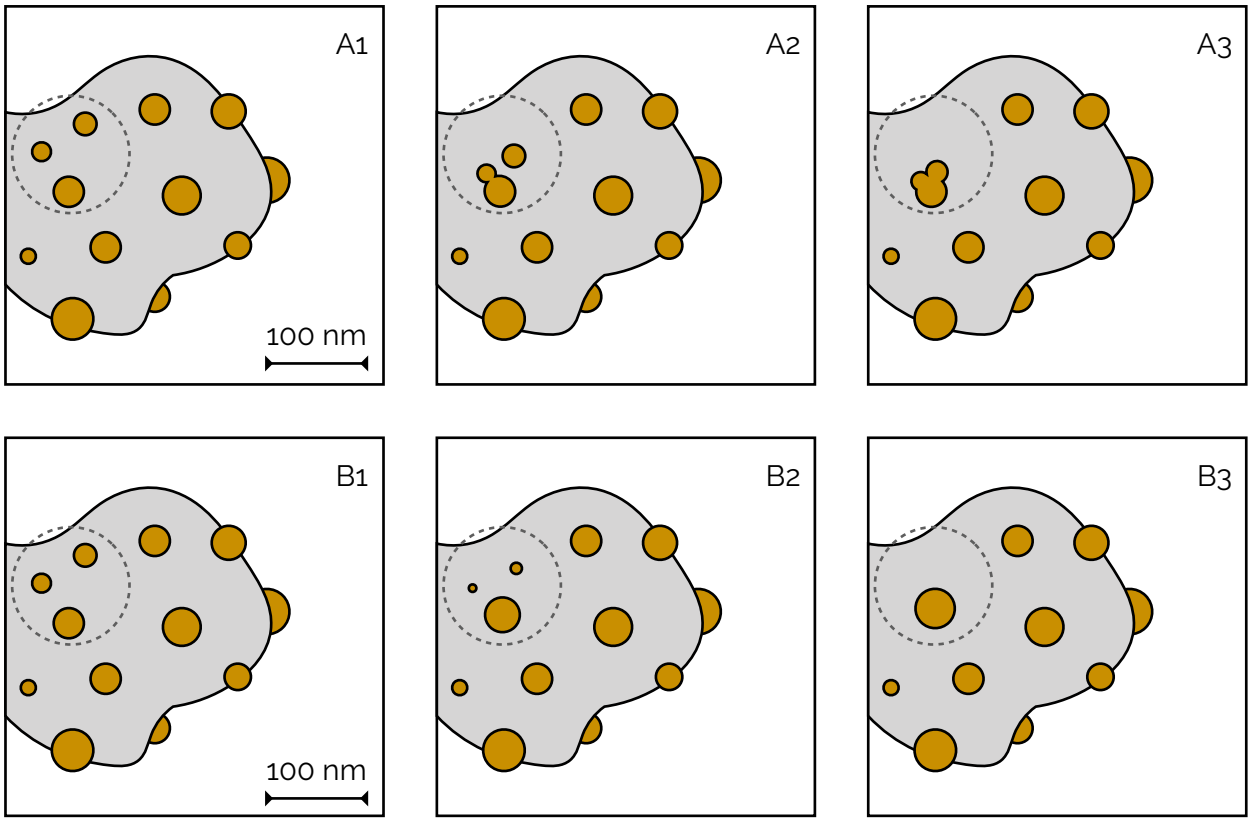

Figure 3.8 - A: Sequence of crystallite migration. B: Sequence of Ostwald ripening Schematic depiction of experiments taking place at 600 ˚C, adjusted from (Sehested, 2006)

The same temperatures and conditions that enable particle migration, also cause the nickel catalyst to form volatile compounds. These volatiles are no longer catalytically active, and the metal is permanently lost to when these compounds vaporise. For IR SOFCs, steam and carbon monoxide are the two main culprits forming hydroxyls ($Ni(OH)_2$) and carbonyls ($Ni(CO)_4$) respectively. Figure 3.9 shows how a carbon monoxide rich environment may cause the formation of metallic carbonyl.
The rate at which hydroxyls and carbonyls form in SOFCs is not yet known due to ill-defined adsorption stoichiometric and a strong coupling with sulfur poisoning. Nevertheless, it is deemed a much slower process than other forms of catalytic deactivation (Bartholomew, 2001).

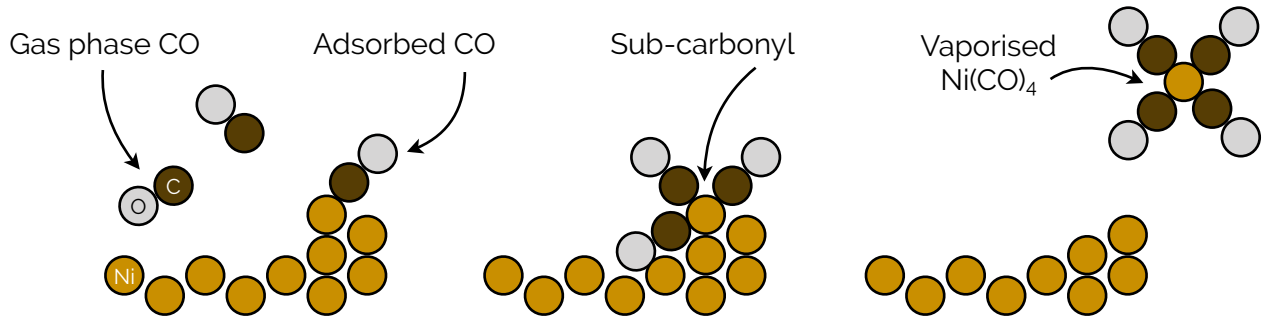

Figure 3.9 - Formation and vaporisation of $Ni(CO)_4$ at the surface a nickel crystallite (adjusted from (Bartholomew, 2001))

All of the mechanisms described here alter the geometry, and amount of available catalyst. This in turn results in less active area for the same amount of methane (assuming constant fuel flow conditions for all times). This results in an increasing rate of carbon deposition over longer times.
Primary carbon deposition must be mitigated by selecting appropriate process conditions, such as steam content, methane content, temperature and catalyst loading, whilst keeping impurity concentrations within limits. Secondary carbon deposition must be prevented by creating robust catalytic coatings, impervious to sintering processes and formation of various volatiles.

MEASURING THE AMOUNT AND TYPE OF CARBON FORMATION

In the previous sections, different types of carbon formations have been described. These types of formations have been described here rather clinical and clear-cut, but in reality a continuous mixture of phenomena can be observed.
Experiments have been developed in order to distinguish between carbon formations. This is a vital step in improving the lifespan of the fuel cell. After all, how can you mitigate carbon deposition when the specific type of formation is unknown.
Different methods have been developed and used in order to accurately determine both the amount and type of formation. In recent years, DRT analysis (Distribution of Relaxation Time) and ADIS (Analysis of the Difference in Impedance Spectra) have been used extensively. These are types of electrochemical impedance spectroscopy methods, and can be used to measure multiple types of failure modes in IR SOFCs simultaneously.

1. Nickel micro-structural evolution.
2. Changes in volume of nickel phases caused by redox cycling, see section 3.6.
3. Carbon and sulfur poisoning

Using the ADIS method, a complex equivalent circuit is composed that acts the same way as the cermet. The impedance of an unused Ni/YSZ anode differs from a degraded one, and changes in impedance are caused by one or more phenomena enumerated above.

The accuracy of this method depends on the number of elements in the equivalent circuit (resistances, capacitance and inductors). The circuit must be sufficiently complex to describe the cermet. The shortcoming here is that the number of elements that identifies the correct amounts of degradation is not known a priori.
That being said, equivalent circuit analysis methods are more established, easier to implement and able to identify types of degradation with low-quality data. Figure 3.10 shows how an equivalent circuit can be composed from the ADIS method, assuming the circuit consists of five elements. Note that the value of each component changes with varying current density (Takeguchi et al., 2002).

With the DRT analysis, the cermet under investigation is charged. The transient response to natural discharge (relaxation) is ultimately investigated. No assumptions to the number of elements have to made with DRT, making this method suitable for quantifying processes that overlap in the impedance spectra. The shortcoming of this method is that it requires high-quality data, making it more difficult and expensive to obtain accurate results.

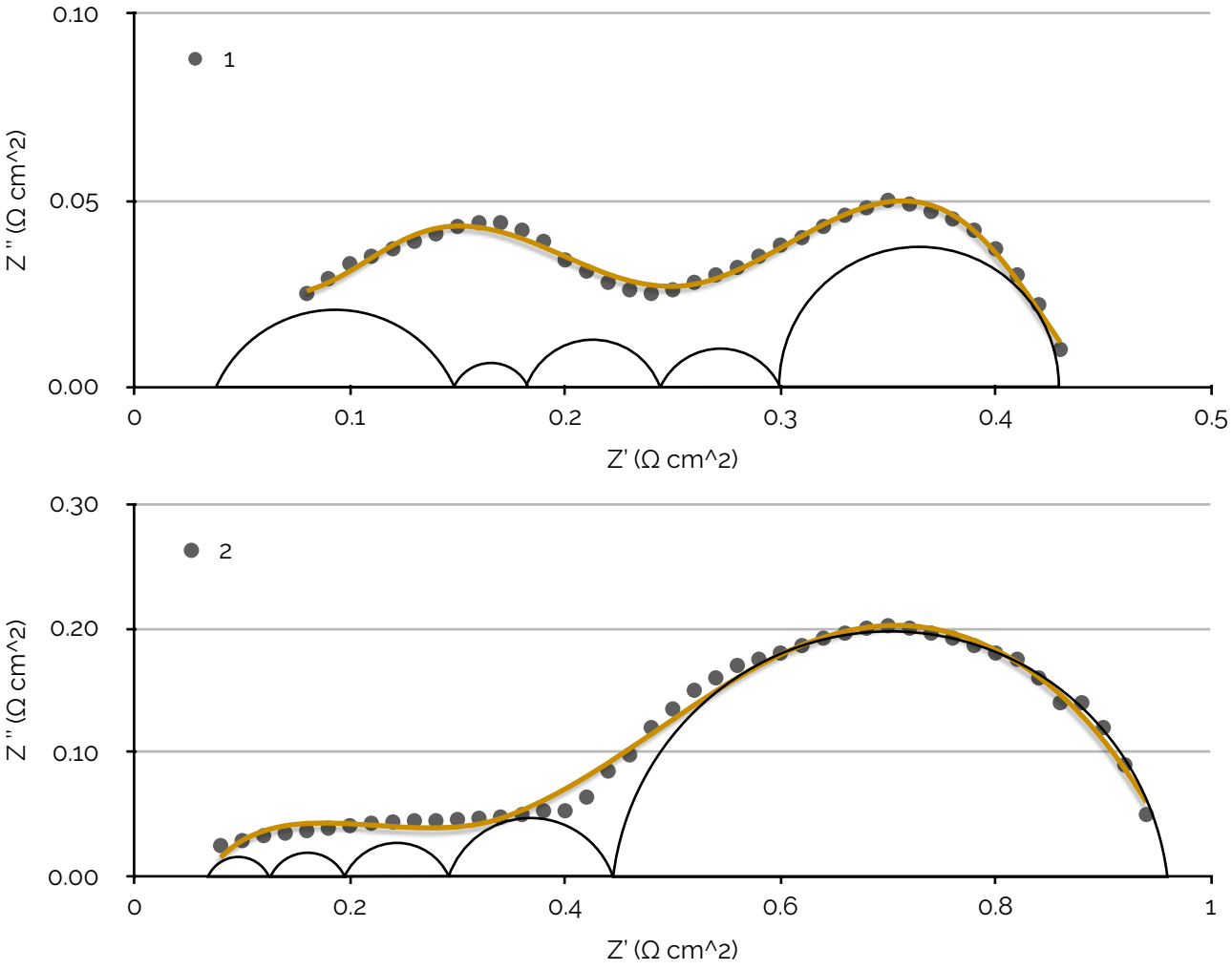

Figure 3.10 - Impedance spectra of Ni-YSZ electrode at (1) OCV and (2) electrolysis current density of 2.0 A/cm² using 45% H_20, 45% CO_2 and 10% H_2. Circles represent inductances and the line is the combined inductance aimed to match the measurements taken (dots). (Tao, Ebbesen, & Mogensen, 2014)

3.5 - Thermal degradation

In the previous sections, several chemical degradation mechanisms have been discussed. The lifetime of a SOFC can be significantly shortened by failure due to thermal stresses.
Thermal stresses occur when components expand further due to increasing temperature than physically allowed by the surrounding components. Both material type and geometry are important factors to limit thermal stress. An important design parameter is the thermal expansion stress-free strain, given by equation 3.1.

$$\epsilon_t = \alpha (T - T_0) \qquad [3.1]$$

The symbol α is defined as the coefficient for thermal expansion (CTE) and T_0 is a reference temperature. Temperatures below this reference will result in expansive strain, elevated temperatures give compressive strain.
The reference temperature is often set at the temperature at which the part is produced. When the part cools down, initial residual stresses will be present in the material. At operation conditions, these residual stresses will be minimised again.
The second source of thermal stress in planar SOFCs occurs when two or more plates with a deviating CTE are bonded together. The structure will now only expand as much as the stiffest component allows. The additional stress in the constraint plate(s) is now given by equation 3.2, which is valid for continuous plates without uniform material properties, sufficiently far away from the corners of the plate.

$$\epsilon_e = \frac{\sigma (1 - \nu)}{E} \qquad [3.2]$$

The symbol E is Young's modulus of the material, and υ is Poisons's ratio. The total strain in a layer can be approximated by adding both strains together. From this, it is clear that widely varying CTE's and fracture sensitive materials are susceptible to thermal fractures. Table 3.3 lists the relevant material properties of YSZ, and nickel loaded YSZ. From this table, it can be seen that the CTE for yttrium stabilised zirconia is lower than the nickel containing variants (both reduced and oxidised states). This means that the thin and strong electrolyte will experience compressive stress, which is a good bases to suppress fractures.
The amount of residual stresses inside 8YSZ electrolyte material, confined by the rest of a planar SOFC at room temperature is around 600 MPa. After reduction of NiO to Ni, this is only 450 MPa (both values compressive). This has been measured by x-ray diffraction. It is suggested that lower value of residual stress in reduced state is due to an increase in porosity, as well as the transformation from rigid NiO to a more ductile Ni (Sun, Rudkin, & Atkinson, 2009). Figure 3.12 (1) and (2) in the next sections show how this has been observed. Fuel cells operating at 900 °C to 1000 °C have almost negligible amounts of residual stress inside the electrolyte plates.

Material	CTE (ppm K^{-1}) (25 - 1000 °C)	Young's Modulus, E (GPa)	Fracture Toughness, K_{IC} (MPa $m^{1/2}$)	Critical Stress, σ_c (MPa)
8YSZ	10.5	215	1.7	416
3YSZ	10.8	211	5.7	770
NiO/YSZ	12.8	70	1.7	90
Ni/YSZ	12.5	30	2.5	75

Table 3.3 - Material properties of YSZ and nickel containing variants

STRESS DUE TO TEMPERATURE GRADIENTS

Another form of thermal stress is found inside the same material, which is exposed to local thermal gradients. For IR SOFCs, the net endothermic surface reactions for methane reforming are compensated by the net exothermic hydrogen evolution. From a global perspective, an internal reforming cell operates near thermal equilibrium. But when these reactions take place sequentially at different locations along the fuel channel, thermal gradients will still occur.
FEM studies have shown that tensile stresses due to thermal gradients can exceed 40 MPa, which is a value close to the critical stress for Ni/YSZ (Clague, Marquis, & Brandon, 2012).

3.6 - Redox cycling

Besides thermal degradation, another physical failure mode of SOFCs is caused by redox cycling. This phenomenon has been most recently discovered by new imaging technologies, that have made it possible to observe changes in the microstructure of de electrodes under varying operating conditions. The most damaging change in the anode electrode occurs when nickel oxidises to NiO, and is consequently reduced. The volume difference between the two nickel states is roughly 70%. Ceramic cermet assemblies may crack due to this cyclical expansion and contraction, similar to material stresses caused by thermal expansions.
Another effect of redox cycling is once again the agglomeration of nickel crystallines, resulting in a reduction of active surface area and consequently less activity towards the reforming reaction. This result is similar to some chemical failure modes discussed in section 3.5. The fact that the most obvious consequences of redox cycling could also be described by chemical and thermal effects, has lead to some disagreement in literature when this phenomenon was first described. Well-designed experiments and excellent imaging technologies have led to a general acceptance of redox cycling mechanisms in SOFCs. Figure 3.12 shows how redox cycling may cause the electrolyte to crack. Depending on the thickness of the electrolyte, another failure mode is de-lamination where the electrolyte cracks along the length of the material. Studies investigating the decrease in power output due to redox cycling have concluded that increased temperatures increase the rate of performance drop. Using results at 750 °C as a base line, degradation was roughly 2 times slower at 700 °C and 5 times slower at 600 °C (Wood, Pastula, Waldbillig, & Ivey, 2006). For IR SOFCs, generally running at temperatures beyond this range, redox cycling could be a detrimental failure mechanism.

CAUSES OF REDOX CYCLING

In order to the anode inside a SOFC to function properly, it must be reduced prior to operation. This reduction takes place in the absence of oxygen. The reduced state is vital, since oxygen ion conduction is greatly enhanced in this state. The nickel (or other metallic catalysts) that remains is also in the appropriate state for efficient operation.
In the event where oxygen is reintroduced to the anode, this layer is once again reduced. This completes the first redox cycle. In principle, this oxygen can have three places of origin.

1. Non-ionised oxygen from the cathode side might diffuse through a relative coarse section of the electrolyte layer
2. Oxygen might leak in from outside the fuel cell stack
3. Oxygen enters via the fuel channels in the case of a shutdown

Whilst the first two might be solved by creating air-tight cells and stacks, the latter one will always be a possibility. Maintenance, shutdowns or changes in fuel feed will allow for atmospheric conditions

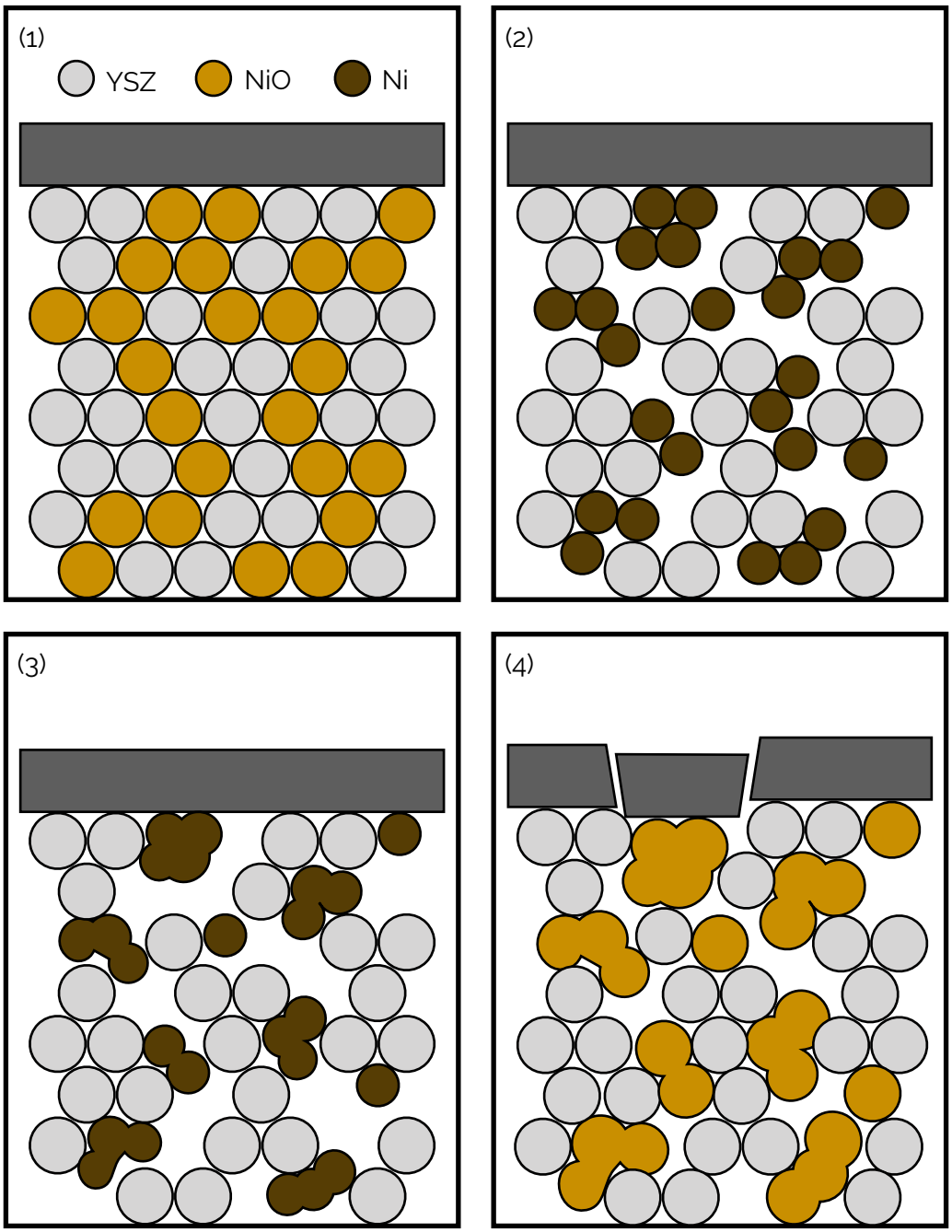

Figure 3.12 - Redox mechanism in Ni/YSZ cermets showing (1) the sintered state, (2) the immediate reduced state, (3) the long-term reduced state, (4) the re-oxidised state with defects in the electrolyte

to reach the anode side of the cell. During the lifetime of a system, a stack might go through several redox cycles, where the anode might be exposed to air for several hours.
The anode and electrolyte must be protected against permanent damage and performance drop, so that a targeted lifetime can practically be reached.

DESIGN STRATEGIES TO WITHSTAND REDOX CYCLING

Solutions mitigating damage and performance drop due to redox cycling can be divided into two categories. Firstly, changing system parameters and adding systems around the fuel cell stack that prevent the fast and uncontrollable re-oxidation of the anode cermet. One example of a system solution that might prevent damage by a redox cycling is by purging the fuel channels of the stack

with steam in the event of a shutdown. Steam purges of six hours show no degradation, compared to an air (atmosphere) purge, where a drop of 11% has been observed in the same amount of time. The steam could be generated by boiling water during the shutdown, using the heat still present in the system. This idea does not add much complexity, costly and exotic materials to the overall system.
Furthermore, interesting results have been found in the second category, where materials and general stack design result in a better resistance to redox cycling.

One solution has taken inspiration from the protective oxide layers on metals such as aluminium. A physical oxidation barrier can be created by depositing a fine layer of nickel on the bottom of the anode layer by using a physical or chemical deposition process. This nickel layer oxidises and densifies, protecting against further oxygen diffusion into the more vital parts of the anode cermet.

Other solutions are all based on changing the anode micro-structure. By using an anode layer of 300 µm meticulously divided into sublayers with a thickness of ~10 µm with decreasing nickel loading towards the electrolyte, some improvements to the degradation rate have been shown.
Dividing the anode layer into sublayers of different porosity have shown more potential. The porosity at the electrolyte side must be highest, to allow for more expansion and changes in microstructure.
Finally, gradually pre-oxidising the anode layer at significantly lower temperatures of around 500 °C seemed to work best. Table 3.4 compares the percentage drop of a V-I curve test and a steady-state hold test per redox cycle to the baseline case at 750 °C (Waldbillig, Wood, & Ivey, 2007). All previously mentioned strategies are listed, apart from the steam purge approach where no degradation was observed.

Test Type	Degradation (%) V-I Curve Test	Degradation (%) Steady-State Hold Test
Baseline (750 ˚C)	10.8	8.5
Oxidation barrier	8.8	7.9
Gradient in nickel loading	7.8	7.6
700 ˚C redox	5.4	3.2
Gradient in porosity	4.2	3.5
550 ˚C pre-oxidation	3.3	2.2
600 ˚C redox	2.2	0.9

Table 3.4 - Relative effect in improved resistance against redox cycling degradation compared to a baseline anode at 750 ˚C

3.7 - Conclusions

This chapter described chemical and physical phenomena that limit the lifetime of IR SOFCs. It is important that a complete overview is given here, since some mitigation strategies for one failure mode, promote other failure modes. Even recent studies have proposed to poison the anode with sulfur compounds purposefully, since some experiments have shown that this increases the resistance against redox cycling. This recommendation goes against earlier works focussing on chemical

degradation. In order to achieve the targeted lifetimes, all failure modes as well as their causes and solutions must be known to researchers.

This part of the literature study aimed to find all failure modes of SOFCs, caused either directly or indirectly by carbon formations inside the fuel cell.
A short list of conditions that must be respected in order to reach the desired lifespan of 40,000 hours has been compiled from the sections in this chapter.

- The temperature inside the fuel cell must be kept above 500 °C to prevent encapsulating carbon formations. This will lead to decreasing catalyst activity, which triggers whiskers formations as well. When the nickel content is too high (to aid in the electrical conductivity of the cell) the methane reforming reaction might occur very locally. This endothermic process might cause cold spots below 500 °C, and trigger the irreversible carbon formation process.
- When temperatures get above 450 °C, whisker and pyrolytic deposition can occur. To prevent this, the H_2O/CH_4 ratio must be kept above 2. This does not only applies for the inlet gas composition, but throughout the entire fuel cell. A model, which accurately predicts the reaction rate may help to ensure this ratio is respected throughout the fuel cell.
- Temperature gradients must be limited. Methane reforming will cause local cold spots, whilst places with higher H_2 concentration produce hotspots. A combination of both phenomenon might lead to thermal failures. A model of an entire cell might help to localise troublesome areas where thermal stress might exceed the capabilities of the materials used.
- The nickel catalyst must be imbedded in the YSZ in such a way that it can withstand the operating conditions. The grain size and site density must be carefully controlled. It is recommended that the nickel site density lowers towards the electrolyte to prevent redox cycling due to trace oxygen leaking through from the cathode side. Near the top of the anode layer, site density should be maximised.
  The grain size must be predictable as well. Too big (400+ nm) will result in much less triple boundary length. Grains that are too small (10 - 20 nm) will be lost due to Oswald ripening or particle migration. When the nickel catalyst structure changes over time, this leads to performance loss. A scalable technique must be developed to permanently embed nickel particles of roughly 100 nm, in increasing density in YSZ.
  The microstructure and precise composition of the catalyst is not modeled and lies outside the scope of this thesis. But it should be noted that the microstructure of all functional layers in the fuel cell are just as critical in order to reach the desired life time.
- The cell must be almost 100% reliable. Every time the fuel cell is opened for upkeep or repair, a redox cycle might permanently damage the electrolyte layer. Oxygen can now crossover to the anode and cause further damage such as re-oxidation of the anode.

4 - Modelling strategies

This chapter contains the second part of the literature study, and focusses the remaining study goals. Section 4.1 and 4.2 are focused on the question of what type of model is best suited to model carbon deposition. In section 4.3 to 4.5, the overall complexity of the model is determined by exploring model setups ranging from 1D to 3D. Finally, in section 4.6 two strategies for modelling chemical reactions are discussed.

In this chapter several modelling strategies are presented. In recent years, there's an increase in CFD models involving SOFCs. Typically models consist of a single channel or unit cell, simulating all or some of the complex phenomena inside the fuel and oxygen channels and all supporting layers in between them. The other type of fuel cell model involves an entire fuel cell stack or system. These kind of models are used in general balance of plant calculations and are not discussed in this chapter.

In this chapter, modelling strategies and concepts are discussed with the main objective in mind. What kind of model is best suited for modelling carbon deposition inside internal solid oxide fuel cells? The scale and complexity of model must be determined. In the next chapter the chosen modelling strategy is presented without much further justification than given here.

4.1 - Physical modelling and empirical modelling

A mathematical model describes a representation of reality, by processing on or more input variables. This definition of a model is so broad that it is not very insightful.
A distinction between physical modelling and empirical modelling can be made. The difference between these modelling philosophies is significant and fundamental. Every time someone decides to create a model, choosing between a physical model or an empirical model should be the first step.

PHYSICAL MODELS

Physical models use the laws of physics along with conservation equations to transform an input signal into an output signal. For example, a model of a velocity gradient of hydrogen inside a fuel cell channel be estimated by using conversation of mass and momentum and an initially known velocity profile.

This might sound as a bulletproof strategy, but resulting concentration profiles in the simple model described above can already deviate greatly from reality. Why is this?
Because the model only contains the equations the user decided to put in. In modelling theory, this is referred to as apriori modelling or "white-box" modelling. White-box (as oppose to black-box) modelling, because we know exactly which equations (or input processors) are present inside the box. In this case, the input velocity might be high enough for turbulence to play an important role. The creator of the model *assumed* turbulence could be neglected. Therefore, only parabolic velocity profiles can emerge from this model.

In physics and mathematics, these type of models are most often used. The main benefit of knowing what is inside the model, is that the creator of the model has full control and can enable or disable certain physical phenomena by choice. For example, heat conduction, convection and radiation are always present. But inside a model radiation can be ignored, by simply deleting the equation of heat transfer by radiation. When the output still closely represents reality, it can be concluded that

radiation can be ignored. This furthers our understanding of this heat transfer problem. These type of conclusions can only be made by using a physical approach.

A major drawback of this approach is that the model is only as complex as the creator can make it. An internal reforming fuel cell is a complicated thing to model; fluid dynamics, chemistry, thermodynamics and physics are all involved. At a certain point too much interdisciplinary research might be required to implement each aspect accurately, especially when time and money constraints are present (Milewski, Świrski, Santarelli, & Leone, 2011).

EMPIRICAL MODELS

These type of models use historical input and output data, to construct a fitting model in between. For example, a set of operating conditions of a fuel cell such as temperature, mass-flow and pressure can be linked to experimental (empirical) results or output conditions such as cell voltage and fuel utilisation.
The model that results from the empirical method is a black-box model, we don't exactly know what goes on inside. In essence, the model imitates nature and tries to find dependencies between temperature and cell voltage without using physical concepts such as heat conduction or molecular vibrations.

Empirical models rapidly grow in popularity. This is due to advancements made in this direction. Neural networks, genetic algorithms and in more general terms artificial intelligence form the basis of the latest empirical modelling strategies.
These models have been used to successfully predict incredibly complex phenomena in economics, demographics, social studies but also physics and the operation of (SOFC) fuel cells (Milewski & Świrski, 2009) (Ma, Zhang, Lin, Cong, & Yang, 2021).

To illustrate how these types of models fundamentally differ from physical models, the following example highlights the strengths of the empirical approach.
Large cities struggle with the collection and processing of waste. In an ideal scenario, the people working at garbage collection services can predict how much waste is present in every street throughout the city. Empirical models have been used to accurately predict precisely this. This is based on hundreds of demographic variables such as household income, how many persons live in a household, the proximity of high schools, hospitals and police stations, along with data of how much waste has been collected in the past.
A time series neural network (to account for seasonal changes in waste output) can accurately predict this vast and complex problem. Modelling such a complex system by using a physical approach is impossible.

Internal reforming fuel cells feature many physical phenomena that are highly interconnected. The added complexity of carbon deposition could be too complex to model accurately.
It is possible to collect all experimental data on SOFC performance, along with their respective operating conditions and let a neural network (with a sufficient amount of hidden layers) to construct a black box that can accurately imitate the corresponding results. When this black box also accurately predicts the fuel cell performance with operating conditions not used as an input, a working and correctly functioning model has been created.

TYPE OF MODEL USED IN THIS THESIS

For this thesis, a physical model will be created for two reasons. One of the goals of this thesis is to find out what physical phenomena can be ignored. This can't be done when an empirical model is

employed. Furthermore, a lot of preceding studies have already answered a lot of subquestions that can be readily be used as import parameters in a physical model.
The second reason is that this thesis is written for the degree of process engineering, where understanding of physics, fluid dynamics and transport phenomena are used in advanced process design.

4.2 - Physical modelling based on the Nernst equation

A physical model of a SOFC has to deal with multi-phase physics taking place on the fuel cell surfaces. This includes heat transfer together with electrochemical reactions, as well as charge transport by conduction inside the cell. Mass transport from the inlet to the outlet, as well as mass transfer from one element to another.
These physical phenomena are changed by the geometry and several other parameters. The main parameters are shown in figure 4.1. Many physical models of SOFCs have already been created, and all of them have used these parameters (Kakac, Pramuanjaroenkij, & Zhou, 2007).

The geometry of the fuel cell can be planar or tubular, but in either case the geometry is not complex. But modelling the way they operate is difficult to model, mainly because of the vast amount of coefficients that need to be defined. Many variants of SOFC are being developed, and they are made from varying materials that are still being improved and studied.
The anode, cathode and electrolyte layers can widely vary in porosity and micro-structure (such as surface area and triple boundary length), even within the layers themselves.

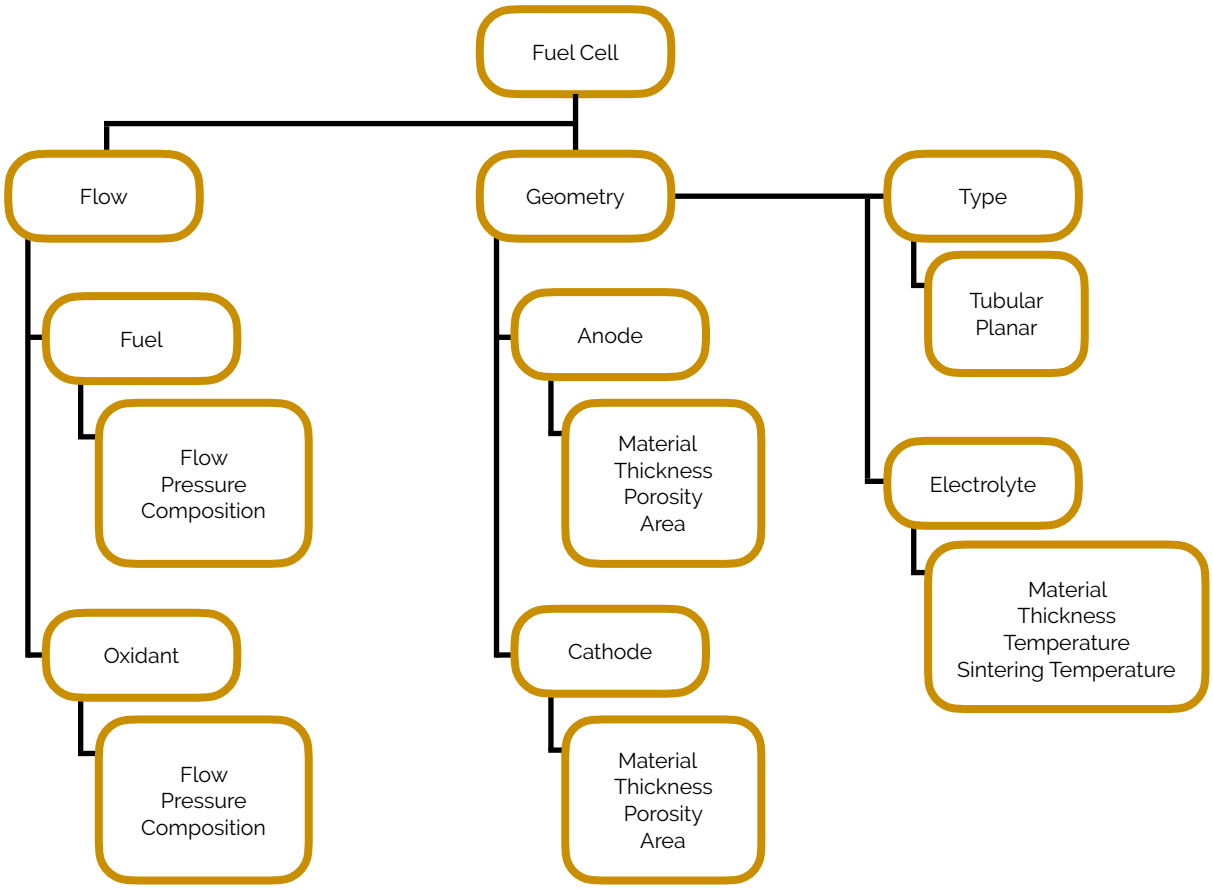

Figure 4.1 - Main parameters of a SOFC model

A model is therefore often only accurate for one specific type of SOFC at a narrow operating window. For researches it is difficult to replicate or alter the models used because only the results are shared.

The physical SOFC models are all mainly based on the Nernst equation, along with the concepts of activation, ohmic and concentration losses. The model designed or this thesis will embrace this same approach, mainly because of the lack of well documented alternatives. This approach has resulted in models that replicate experimental data very well, at least when the models and experiments are done within the same research group. The models show generally much more poor agreement with experimental data when compared to other experiments. This is due to numerous factors which are difficult or even impossible to determine (Virkar, 2005).

TRANSIENT AND STEADY STATE MODELS

Two subtypes of physical models are transient and steady-state models. In the latter case, all conditions such as inputs, material properties and other operating conditions are constant in time.
Steady-state models are usually first considered, because this modelling scheme requires less computing power. Furthermore, a transient model has more ways of diverging than a steady-state model.

Only when a problem absolutely requires a transient scheme, it should be chosen. Some examples when this is the case are the following.

- When fluid flows are so turbulent, they cannot be accurately modelled by statistical averaging such as the RANS method. In this case, transient LES or hybrid DES formulations give more accurate results (Hanjalic, Kenjeres, Tummers, & H.J.J, 2008). For example, some flows around bodies result in unpredictable vortex shedding with vortices the size of the bodies themselves. Even though all conditions are essentially constant, a transient approach is still required.
- When input parameters substantially change over time, such as day-night cycles or changing wind conditions. For example, to see how a bridge performs under changing weather conditions.
- When materials or material properties change over time. For example, when a piece of log burns the material changes over time from wood to charcoal. Some of the mass leaves the domain in the form of combustibles.

The main goal of the model developed in this thesis is to find areas inside the fuel cell channel that are more vulnerable to carbon deposition. This can be done with constant inlet conditions, with a low volume flow so that laminar conditions are maintained. Carbon deposition (a transient, material altering process) will not be simulated.
Only when carbon deposition itself needs to be modelled, the transient scheme is required. This model will only show where the first carbon depositions are likely to occur, based on local conditions.

TIME- AND LENGTH SCALES RELEVANT FOR SOFC MODELLING

An important challenge of modelling all covering all physical aspects of an SOFC, which take place across greatly variable length scales. Table 4.1 gives an overview. In this thesis, a fuel channel is the largest length scale in the domain. Take note that for modelling complete SOFC systems, even larger scales must be taken into account.
In literate two types of SOFC modelling can be observed.

1. Studies that focus on one specific aspect listed in Table 4.1. For the smallest length scales i.e. surface chemistry simulations, CANTERA is commonly used.
   For structural changes in the microstructure of porous media DENIS is used. This program can also be used to model the heat, mass and charge transport in the surrounding flow domain.

2. Studies that aim to model all aspects in one program, that being proprietary CFD code or readymade programs that can deal with all facets of a SOFC system in one way or another. Examples here are MATLAB, SIMULINK, and ANSYS. In practice, this means that the surface chemistry and local electrode behaviour are partially simplified, implied or even ignored.

Level	Length and time scales	Chemistry	Transport	Modelling approach
Surface	10^{-8} m 10^{-6} s	Surface chemistry	Surface diffusion	Mean field kinetics
Electrode	10^{-4} m 10^{-2} s	Thermal and redox cycling	Porous multiphase mass and charge transport	Continuum transport and percolation therory
Fuel Cell	10^{-2} m 10^{0} s	Gas-phase chemistry	Laminal flow Heat convection	Heat, mass and charge transport
Stack	10^{-1} m 10^{2} s	-	Laminal flow Heat conduction and radiation	General CFD codes
System	10^{0} m 10^{4} s	-	Mass and energy fluxes	Process simulators

Table 4.1 - Typical length- and time scales relevant for all-encompassing SOFC models

4.3 - 1D modelling strategy

Solid oxide fuel cell models already exist in many forms. One of the most common type is a 1D model. These models can be very robust from a mathematical viewpoint, and partial analytical solutions may exist when boundary conditions are set straightforward enough. For a 1D approach, it is required that all governing equations are solely expressed in one coordinate direction.

The most obvious shortcoming of 1D-models is that the model either completely ignores flow along the channel, or neglect all phenomena perpendicular to the electrolyte. Neither approaches will be very accurate in the end. In order to find local conditions that might lead to carbon formation, a multi-dimensional approach must be taken.
This can be done in two ways. The first method is to expand the entire domain to two dimensions. In this way, a coupled two dimensional system of equations must be solved. This has similar features and drawbacks to the 3D approach discussed in section 4.5, and therefore omitted in this thesis.
Another method is the 1D + 1D strategy, which is elaborated on in the next section.

4.4 - 1D + 1D modelling strategy

The model equations and notation in this section are adopted from non-published lecture notes from the course "Electrochemical Energy Storage" taught at Delft University of Technology in 2020 (J.W. Haverkort, 2020). Figure 4.2 shows how the domain of a fuel cell is typically divided so that a 1D + 1D model can be employed. For clarity, only the anode side of the fuel cell is drawn. All physical quantities are conserved in each domain. The concentration of methane is shown in Figure 4.2, the same could be done for other variables like temperature, pressure and current density.
The distance that methane travels in the flow direction is 9 cm. The diffusive lengths in the x-direction all the way to the electrolyte are much smaller, usually only 0.1 mm to 50 µm.
By dividing the flow channel into small blocks with a length to the width of the diffusion and catalyst layer, the concentration in the z-direction can be assumed to be constant in each block section. This is a valid assumption when concentration changes in the z-direction are several orders of magnitude smaller than concentration changes in the x-direction. This creates two separate 1D problems instead of a 2D problem.

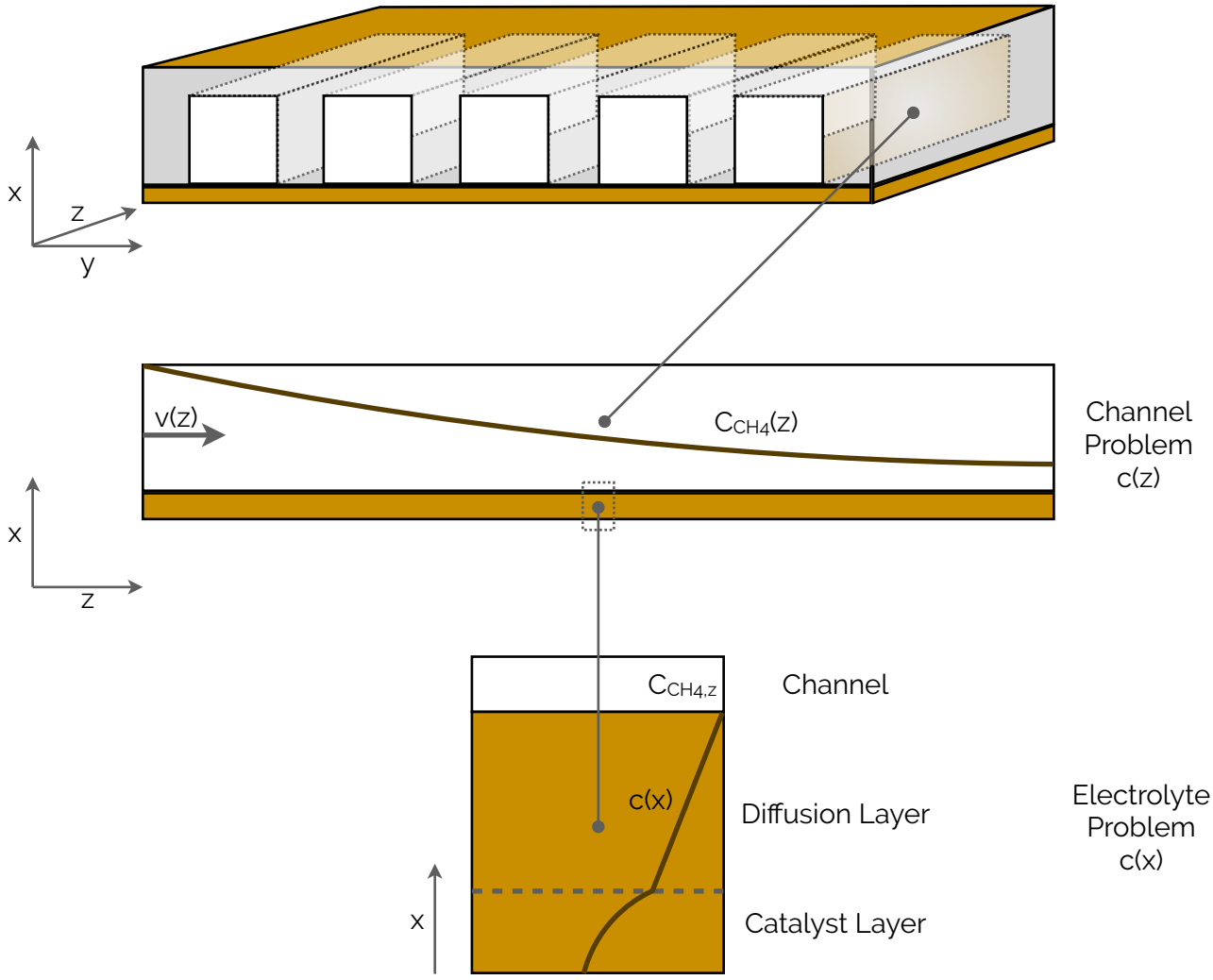

Figure 4.2 - Schematic of 1D + 1D model, showing the axial channel model and perpendicular diffusion model, adapted from (J.W. Haverkort, 2020)

CHANNEL PROBLEM

For further illustration, a brief description of a general channel model is provided here. The same coordinate system (x-z) is used as in figure 4.2, and the conserved quantity of concentration is also used.

The diffusion equation (equation 4.1) governs the concentration profile inside the channel. The flow velocity is denoted by v (m/s), the diffusivity coefficient by D (m^2/s). Using the boundary conditions and (known) velocity profile shown in figure 4.3, the mean concentration c_m is defined as in equation 4.2. The mean velocity is given by u (m/s) and the virtual thickness of the channel is defined as d (m). At the top of the channel, the flux is zero since this wall is impermeable. At the bottom, the flux is finite but still unknown (N).

A common trick in these kind of transport phenomena problems, is convert the boundary conditions and governing equations to dimensionless numbers. In case of concentration profiles the Sherwood and Graetz number may be used, as in equation 4.4 and 4.5. The Sherwood number is similar to the Nusselt number in heat transport problems, and the Graetz number is similar to the Péclet number. Equation 4.1 can be rewritten to equation 4.6, by using relative concentrations defined by equation 4.3 as part of the dimensionless set of variables.

With an expression for the wall concentration (c_w), a general solution can be found for equation 4.6. This is done by solving the electrolyte problem separately.

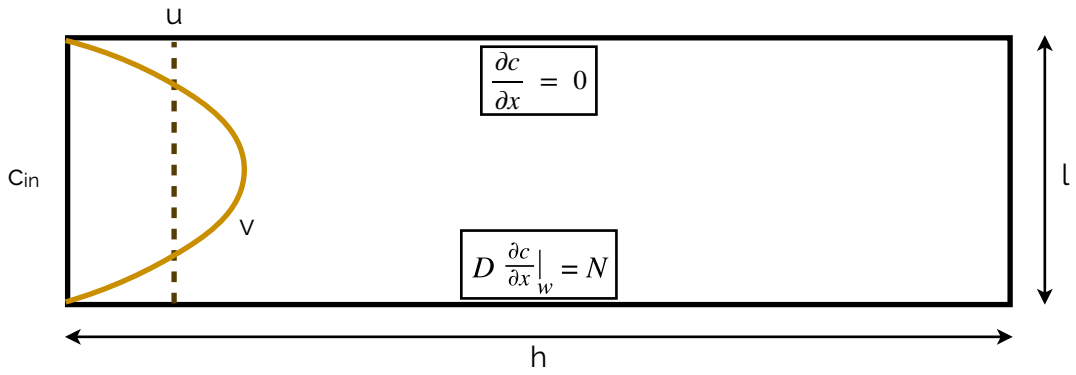

Figure 4.3 - Boundary conditions and velocity profile for general channel problem, adapted from (J.W. Haverkort, 2020)

$$v \frac{\partial c}{\partial z} = D \frac{\partial^2 c}{\partial x^2} \quad [4.1]$$

$$c_m(x) = \frac{1}{u\,d} \int_0^l v c \, dx \quad [4.2]$$

$$\bar{c}_m = \frac{c_m}{c_{m,\,in}} \quad [4.3]$$

$$Sh = \frac{lN/D}{c_m - c_w} = \frac{\overline{N}}{\bar{c}_m - \bar{c}_w} \quad [4.4]$$

$$Gz = \frac{u l^2}{h D} \quad [4.5]$$

$$Gz \frac{d\bar{c}_m}{dz} = -\overline{N} = -Sh\left(\bar{c}_m - \bar{c}_w\right) \quad [4.6]$$

ELECTROLYTE PROBLEM

The electrolyte problem is illustrated in figure 4.4. Just as displayed in figure 4.2, only the anode half is drawn. This side consist of the flow channel, anode support layer and catalyst layer. The diffusion of the species throughout these media can be modelled in several ways, depending on the type of material and porosity. From figure 4.4 and assuming the flux inside diffusion layers is conserved, equation 4.7 can be derived. Where Sh_d is the Sherwood number for the diffusion layer (equation 4.8), and k is the reaction kinetic constant, which is converted to the dimensionless reaction constant in equation 4.9.

For the more porous and isotropic diffusion layers, linear diffusion models (Fick's law) are often used. For dense YSZ, Knudsen diffusion is a common modelling approach. Here, the microstructure of YSZ is estimated by assuming it consists of long, cylindrical pores. In the case when the concentration gradient is parallel to these pores, diffusion is determined by the mean free path inside of the pores. The effective diameter of the pores are the only variable that determines the resulting diffusivity. In cases when the concentration gradient is perpendicular to the pores, no diffusion can take place. This assumption is compatible with the 1D + 1D approach, since the local concentration gradients in the z-direction are assumed to be zero.

Going back to figure 4.4, the separate layers with separate diffusion mechanisms (or mass transfer resistances) could be viewed as three electrical resistance in parallel. The overall mass transfer is expressed analogously in equation 4.10.
Using equation 4.6, the concentration profile along the channel can be solved as a function of ⟨S⟩ and Gz, which contain all information of each diffusion mechanism per layer, reaction mechanism in the catalyst layer and channel dimensions. ⟨S⟩ is the running average along the channel length, defined by equation 4.12.

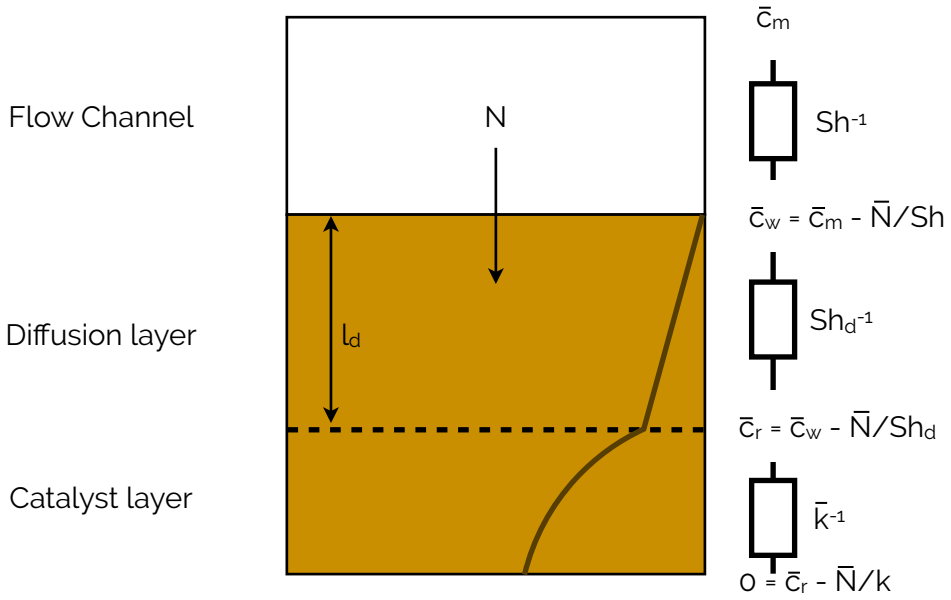

Figure 4.4 - Schematic for the electrolyte problem, represented as three separate resistances in series, adapted from (J.W. Haverkort, 2020)

$$\bar{N} = Sh\left(\bar{c}_m - \bar{c}_w\right) = Sh_d\left(\bar{c}_w - \bar{c}_r\right) = \bar{k}\bar{c}_r = S\bar{c}_m \qquad [4.7]$$

$$Sh_d = \frac{D_d}{D}\frac{l}{l_d} \qquad [4.8]$$

$$\bar{k} = \frac{kl}{D} \quad [4.9]$$

$$\frac{1}{S} = \frac{1}{Sh} + \frac{1}{Sh_d} + \frac{1}{\bar{k}} \quad [4.10]$$

$$\bar{c}_m = e^{-\frac{\langle S \rangle}{Gz}\bar{z}} \quad [4.11]$$

$$\langle S \rangle(\bar{z}) = \frac{1}{\bar{z}} \int_0^{\bar{z}} S(\bar{z})\, d\bar{z} \quad [4.12]$$

Using this model combined with the channel model from the previous section, a complete 1D + 1D model of a fuel cell channel can be defined. Finding a relation between the current density and the cell voltage is the goal of this endeavour, this is discussed in the next section.

COMPLETE CELL MODEL

A schematic overview of a complete fuel cell is shown in figure 4.5. The cell voltage and current density relationship is given by equation 4.13. Here, the open circuit voltage from section 4.1, and the mean concentration profile are ultimately used to describe the entire cell.
Electronic resistance inside the current collectors is almost non-existent, since these materials are excellent electrical conductors. No electronic losses are therefore considered in equation 4.13.
In order to explore equation 4.13 a bit further, the cathodic over-potential is ignored as well.

$$E_{cell} = E_{oc} - (\eta_a - \eta_c) - jAR \quad [4.13]$$

Since AR, E_{cell} and E_{oc} are all assumed to be constant, which means that as the current density j decreases in the z-direction the over-potential must increase. At high current densities near the entrance of the fuel channel, much of the available over-potential is lost to ohmic losses. When the reactant concentrations are mostly depleted near the end of the channel, more activation over-potential is needed to maintain the same current density. This is not possible, so the current density constrainedly decreases. This reduces the ohmic losses, so more of the available over-potential is left for activation losses.

An expression for the current density (equation 4.14) can be made by assuming first order Tafel kinetics. Firstly, $\mathscr{E}$ is the effectiveness factor $\langle c \rangle / c_0$, which is an important performance factor when modelling porous electrodes. Both "a" and "L" are geometric properties of the electrode, the effective surface area and the total length of the electrode respectively. Finally, j_* is the exchange current density. Using Faraday's law $N = j/nF$, equations 4.15 and 4.16, the dimensionless flux shown in equation 4.16 can be constructed.

$$j = \mathscr{E} a L j_* \bar{c}_r \cdot e^{\bar{\eta}} \quad [4.14]$$

$$j_l = \frac{nFDc_{in}}{l} \quad [4.15]$$

$$\bar{j}_* = \frac{\mathscr{E} a L j_*}{j_l} \quad [4.16]$$

$$\overline{N} = \frac{j}{j_l} = \bar{c}_r \bar{j}_* e^{\bar{\eta}} = \bar{c}_r \bar{k} \qquad [4.17]$$

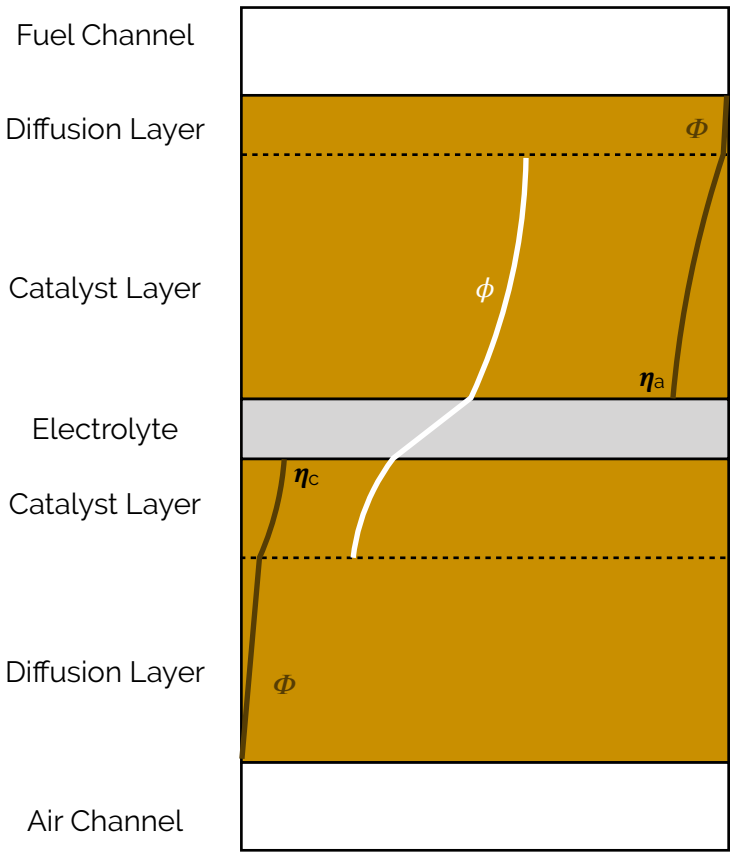

Figure 4.5 - Schematic for complete cell model. Anode and cathode activation overpotentials are shown along with schematic electronic (**Φ**) and ionic (**ϕ**) potential differences, adapted from (J.W. Haverkort, 2020)

This dimensionless flux can be now be used in equation 4.18, which has been derived from the general from 4.13 by using equation 4.19 and 4.20. The only new variable is b, which is the Tafel slope in the standard Tafel equation. Equation 4.10 can now be rewritten to equation 4.22, using equation 4.21.
The overall mass transfer coefficient (1/S) is now dependant on the current density, and the newly defined expression for the over-potential. This can be used to find a modified expression for the dimensionless flux. A global relation between current density and cell voltage is the result in equation 4.23. By further simplifying this equation, some analytical solutions can be found. Otherwise the equation must be solved numerically. Even though this is a 1D-model, physical variables for the porous electrode, geometrical variables for the length and width of all the layers and channels, as well as first order reaction kinetics and Tafel kinetics are used in this model.

$$\eta = \Delta\overline{V} - \overline{N}\,\overline{R} \qquad [4.18]$$

$$\Delta\overline{V} = \frac{E_{oc} - E_{cell}}{b} \qquad [4.19]$$

$$\overline{R} = \frac{A\,R\,j_l}{b} \qquad [4.20]$$

$$\bar{k} = \bar{j}_* e^{\bar{\eta}} \quad [4.21]$$

$$\frac{1}{S} = \frac{1}{Sh} + \frac{1}{Sh_d} + \frac{1}{\bar{j}_* e^{\Delta\overline{V} - \overline{N}\overline{R}}} \quad [4.22]$$

$$\overline{N} = \bar{j}_* \left(\bar{c}_m - \frac{\overline{N}}{Sh + Sh_d} \right) e^{\Delta\overline{V} - \overline{N}\overline{R}} = \frac{jl}{nFD\bar{c}_{m,in}} \quad [4.23]$$

$$\Delta\phi = \frac{jL}{\kappa} \quad [4.25]$$

$$\Delta\Phi = \frac{j}{AR} \quad [4.26]$$

$$\eta_c = -b_c \cdot \ln\left(\frac{j}{j_{*,c}}\right) \quad [4.27]$$

$$\eta_a = b_a \cdot \ln\left(\frac{j}{j_{*,a}}\right) \quad [4.28]$$

This set of equations can be used to find the electronic($\boldsymbol{\Phi}$) and ionic ($\boldsymbol{\phi}$) potential differences, as well as the activation over-potential at the anode and cathode. The global current-voltage relation of the fuel cell can also be constructed.

ADVANTAGES AND SHORTCOMINGS

The complete cell model discussed in this section could be used as a first estimate to find variations local current densities, diffusion rates and flow velocities. With some minor simplifications (neglecting some internal resistances), some analytical solutions could be defined as well.
Furthermore, all the one dimensional equations in this section are suited to be discretised in a straightforward manner. Fast convergence and robust performance are practically guaranteed, when the discretised system is solved by using and implicit scheme. The one dimensional framework also prevents the possibility of numerical diffusion and other numerical artefacts that naturally occur in 2D or 3D systems.
This modelling approach bridges the gap between 1D models and multidimensional models. It has been taught by Willem Haverkort in a course about modelling the storage of electrochemical energy. The modelling approach discussed in this section is not yet published. A 1D variant of this work, only focussing on the expression for the effectiveness factor ($\mathscr{E}$) can be found in some of his published work (J. W. Haverkort, 2019).

The 1D+1D approach has some important shortcomings as well. From figure 4.2 it can be seen that the y-directions is ignored. The area between the channels, where the bipolar plate makes contact with the support layers is not included in the domains. In reality, this is where the current will flow to the current collector at the top of the cell. The model will return some form of 'average' current density in the y-direction.
Another drawback is that with this method, the reaction order and kinetics must be known a priori. For a methane reforming SOFC, this is not that straightforward, since the local current density is coupled with the reaction kinetics. Creating a system of equations the current density depends on the reaction kinetics and vice versa leads to unstable behaviour where infinite solutions may exist.

Two solutions to this problem are found in literature. The first is to assume the reaction rates do not depend on the local current density. This simplification is too great to accurately model a fuel cell. The second option often employed is to assume the voltage applied at the terminal surface is constant everywhere. This is the only simplification needed to resolve a comprehensive fuel cell model.

4.5 - 3D strategies

Three dimensional (3D) models are much more complex than their 1D + 1D counterparts. All equations are evaluated in the three dimensional domain. The diffusion equation in 1D and 3D are shown in equation 4.29 and 4.30 respectively. Only extremely simplified geometries, boundary conditions and constant material properties are solvable analytically, resulting in a solutions containing either error functions or Fourier series. A realistic fuel cell model requires more complex geometries, boundary conditions and variable material properties, so in general it is not possible to explore the governing equations analytically in this case.

$$\frac{\partial c}{\partial t} = D\frac{\partial^2 c}{\partial x^2} \qquad [4.29]$$

$$\frac{\partial c}{\partial t} = D\left(\frac{\partial^2 c}{\partial x^2} + \frac{\partial^2 c}{\partial y^2} + \frac{\partial^2 c}{\partial z^2}\right) \qquad [4.30]$$

The solution is to use numerical methods. The first step is to discretise the system of equations. For 1D-systems this is somewhat cumbersome, but can be achieved by writing your own solver program. Discretising a 3D-system is much more complex. Fortunately, suitable commercial CFD programs exist. In fuel cell literature, almost all 3D studies are at least partially done in such CFD program e.g. ANSYS Fluent.

FUEL CELL MODELLING IN ANSYS FLUENT

The strategy for solving the electrochemistry of the fuel cell in Fluent follows the works of other studies. The surface over-potential at the surfaces of the electrolyte (both anode and cathode side) are the driving force for the electronic and ionic flux. Equation 4.31 governs the electron transport to the current collectors and throughout the solid material in the porous media. The material conductivity (s = solid, e = electrolyte) is given by σ_x. Equation 4.32 describes the same behaviour, but only for the O^{-2} ions through the electrolyte. The R values in these equations represent source terms and are non-zero inside the catalyst layer. The sign of the source terms change at the anode and cathode according to the definitions in equation 4.33 and 4.34. Finally, source terms on the anode and cathode side are defined by equation 4.35 and 4.36 respectively. In these equations, $\boldsymbol{\zeta}$ is the specific active surface area (1/m), and γ is a concentration dependant exponent, and the transfer coefficient is defined by $\boldsymbol{\alpha}$. The subscripts "a" and "c" stand for anode and cathode respectively. These equations are basically forms the Butler-Volmer equation. The driving force in this model is the activation over-potential, the difference in potential between the current collectors (solid) and electrolyte.

$$\nabla\left(\sigma_s \nabla \phi_s\right) + R_s \qquad [4.31]$$

$$\nabla\left(\sigma_e \nabla \phi_e\right) + R_e \qquad [4.32]$$

$$R_s = \begin{cases} -R_a\ (<0) & anode\ side \\ R_c\ (>0) & cathode\ side \end{cases} \quad [4.33]$$

$$R_e = \begin{cases} R_a\ (>0) & anode\ side \\ -R_c\ (<0) & cathode\ side \end{cases} \quad [4.34]$$

$$R_a = \left(\zeta_a j_a^{ref}\right) \cdot \left(\frac{[H_2]}{[H_2]_{ref}}\right)^{\gamma_a} \cdot \left(e^{\frac{\alpha_a F \eta_a}{RT}} - e^{-\frac{\alpha_c F \eta_a}{RT}}\right) \quad [4.35]$$

$$R_c = \left(\zeta_c j_c^{ref}\right) \cdot \left(\frac{[O_2]}{[O_2]_{ref}}\right)^{\gamma_c} \cdot \left(-e^{\frac{\alpha_a F \eta_c}{RT}} + e^{-\frac{\alpha_c F \eta_c}{RT}}\right) \quad [4.36]$$

The mass balance in Fluent is balanced around the defined inlets and outlets. For a fuel cell model, additional terms from the electrochemistry are defined by equations 4.37 to 4.39. These are source (and sink) terms for H_2O, H_2 and O_2. The molecular weight of species x is defined as $M_{W,x}$ (g/mol), and F denotes the Faraday constant (A/mol).
The total electrical current produced in the anode, cathode and triple phase boundary is the same. In Fluent this is expressed by the volume integral in equation 4.40.

$$S_{H_2O} = -\frac{M_{W,\,H_2O}}{2F} \cdot R_a \quad [4.37]$$

$$S_{H_2} = \frac{M_{W,\,H_2}}{2F} \cdot R_a \quad [4.38]$$

$$S_{O_2} = \frac{M_{W,\,O_2}}{4F} \cdot R_c \quad [4.39]$$

$$\int_{anode} R_a\, dV = \int_{cathode} R_c\, dV \quad [4.40]$$

The final important physical aspect of the electrochemistry is the heat source, equation 4.41. An additional heat source is added to each volume element where electrochemistry takes place. The enthalpy change (when positive) of the reaction is added together with heat generation by ohmic heat loss. Finally, the product of the transfer current and activation over-potential on the anode or cathode (depending on the local cell zone definition) is subtracted from the heat source. This capacitive energy storage does reduces heat production.

$$S_h = h_r + I^2 R_{ohm} - R_{a,c}\eta_{a,c} \quad [4.41]$$

All the fuel cell equations have been described. Note that all equations governing the surface reforming are completely decoupled and separately added to each cell. This process is governed by a CHEMKIN mechanism, where each individual surface reaction is

ADVANTAGES AND SHORTCOMINGS

Fluent is a powerful CFD program with practically limitless possibilities. Compared to the single equation found in section 4.3 where only a couple of variables may be adjusted, models can become much more complex in Fluent.
This is essential to explore local conditions inside the fuel channel. These local conditions are the key to find out how carbon deposition originates. Besides the fuel cell module described in this section, the surface chemistry model in the next section together form the basis of the model strategy used in the remainder of this thesis.

Fluent has some inherent and practical shortcomings as well. Inherent to 3D discretised systems, is the effect of numerical diffusion. This is illustrated in figure 4.6. Depending on the order and scheme used, numerical solvers may interpolate values incorrectly. Figure 4.6 displays two temperature streams, one hot and one cold. The diffusion (or mixing) of these streams can be disabled in simulations by setting the diffusion coefficient to zero. No mixing should be observed, which is the case when the fluid flows perpendicular to the cell faces (left image). The right image does show mixing, even though this is physically prohibited. This effect is called numerical (or false) diffusion. The effect of numerical diffusion is most pronounced when a gradient is at a 45° angle to the cell faces. This may be the case near the surface of the anode for the species concentration and temperature.

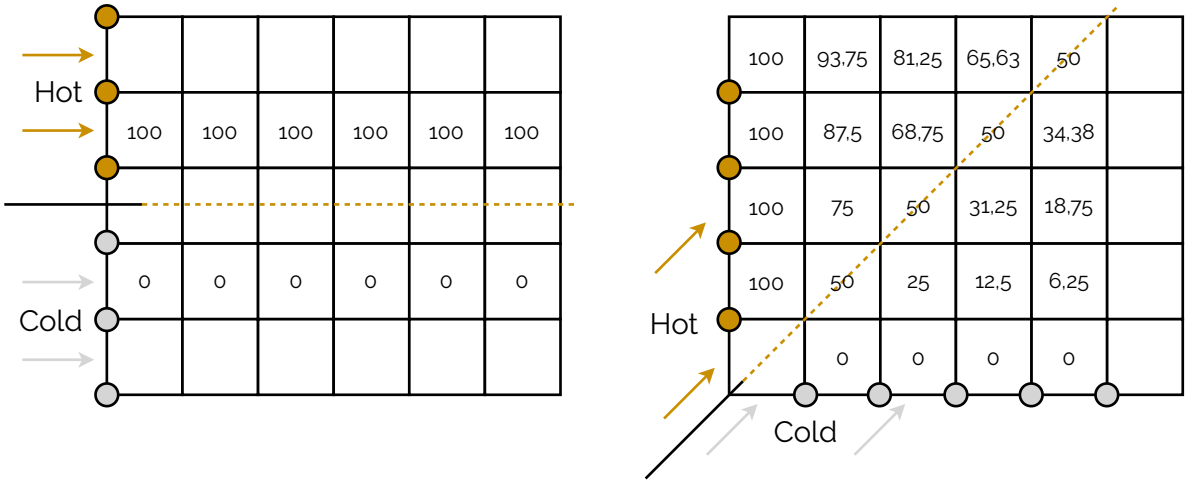

Figure 4.6 - Schematic illustration of numerical diffusion, a numerical phenomenon which takes place when the mesh does not coincide with the flow direction

Another important shortcoming of highly complex systems, is that (part of) the physics may become decoupled when iterating towards a converged solution. This decoupling can have many causes, such as too stiff relaxation factors or unexpected behaviour that directly interfere with boundary conditions. Appendix A3.4 provides further insight in specific cases encountered during the solving process, and how to prevent and fix decoupling as well.
In terms of practical shortcomings, much more knowledge and skill is required to correctly use CFD programs such as Fluent. In involves much more than simply discretising a 1D equation.
The complex, and not very well documented, nature of Fluent can also lead to a 'black box' effect, where the user is not sure whether the software is correctly calculating a physically accurate solution. Appendix A3 provides concrete examples to somewhat mitigate this experience for beginning users.

4.6 - Modelling chemical reactions

Besides the fuel cell modelling schemes discussed so far, different approaches could be taken for modelling the methane reforming mechanism. During this reforming reaction, methane is converted to CO_2, CO H_2 and H_2O. Somewhere during this process, free carbon can permanently damage the anode surface by forming ever growing carbon formations.
It is therefore of vital importance that this facet of the model is complex enough to potentially find regions where carbon depositions can form.
For this thesis two methods are explored. The first method omits reaction rates all together, by calculating the chemical equilibrium of the gasses that are fed to the fuel cell. From there a final overall reaction rate might be assumed or alternatively, it may be assumed that the gasses reach equilibrium instantaneously.
With the second method a reaction rate is simulated. This is done by simulating all possible intermediate surface reactions in the Arrhenius format, with coefficients determined by density functional theory.

CHEMICAL EQUILIBRIUM BY GIBBS ENERGY MINIMISATION

The thermodynamic theory on chemical equilibrium says that the Gibbs free energy must be at the global minimum. The Gibbs free energy of formation can be calculated using thermodynamics. Alternatively, tabulated data is available to skip this step, table 4.2 lists verified tabulated values (Silveira, 2017).
To illustrate the complete picture, with formulas 4.42 to 4.48, similar values as in table 4.2 can be calculated at non-tabulated temperatures as well. The accuracy of this calculation will mainly depend on the accuracy and number of the coefficients for the specific heat (equation 4.46). Higher order polynomials are used to maintain accuracy along a wider temperature range.

$$\Delta G^0 = \sum G^0(prod) - \sum G^0(reac) \quad [4.42]$$

$$G^0 = \Delta H - T\Delta S \quad [4.43]$$

$$\Delta H = \sum H(prod) - \sum H(reac) \quad [4.44]$$

$$\Delta \mathrm{S} = \sum \mathrm{S}(prod) - \sum \mathrm{S}(reac) \quad [4.45]$$

$$\sum c_p = \sum a + b \cdot T + c \cdot T^2 \quad [4.46]$$

$$\Delta H = \Delta H_{298K} + \int_{298}^{T} \sum c_p dT \quad [4.47]$$

$$\Delta S = \Delta S_{298K} + \int_{298}^{T} \frac{\sum c_p}{T} dT \quad [4.48]$$

	CH_4	CO_2	CO	H_2	H_2O	O_2
600 K	-25.01	-396.7	-165.8	0	-214.2	0
700 K	-16.41	-398.1	-175.8	0	-209.1	0
800 K	-8.002	-399.8	-186.1	0	-203.9	0
900 K	-0.132	-401.8	-196.5	0	-198.1	0
1000 K	7.932	-404.2	-207.1	0	-193.2	0
1100 K	15.35	-406.8	-217.9	0	-187.9	0
1200 K	22.34	-409.7	-228.7	0	-182.4	0
1300 K	28.89	-413.0	-239.7	0	-177.0	0

Table 4.2 - Gibbs free energy of formation (kJ/mol) of each considered species at different temperatures, compiled from (Silveira, 2017)

A minimisation algorithm with the proper constraints can find the equilibrated mixture composition given a certain temperature, pressure and initial mixture composition.
This is a useful result to have for two reasons.

- The equilibrium conditions can be compared to simulations if another method is used. By comparing the results, it can now be seen if and where equilibrium is reached.
- In some cases where the reaction kinetics are so fast, equilibrium can simply be assumed to manifest instantaneously. When this is the case there is no need to simulate the complex reaction kinetics, since it will not make the model any more accurate.

From these two reasons it can be concluded that further investigation into the chemical equilibrium conditions is useful either way.

SURFACE CHEMKIN AND DFT

CHEMKIN is a framework where heterogeneous chemical kinetics at gas-surface interfaces are analysed. Initially developed to further the understanding of chemical vapour deposition in the early 90s, the CHEMKIN framework is more widely used today.
Using this modelling method, it is possible to find the kinetic rate-of-progress of a mixture. The number of sites and the amount of species across all phases (bulk, gas-phase and surface) is conserved. All kinds of surface reactions may be used in the model, advection reactions, surface-surface reactions and dissolution reactions. For each reaction, it may be specified to what degree it is reversible. The CHEMKIN framework requires that each reaction is defined by the general Arrhenius expression, equation 4.49 (Coltrin, Kee, & Rupley, 1991). The kinetic reaction rate k_f (mol/s) results from the Arrhenius constant A_r, temperature T (K), temperature exponent β, activation energy E_a (J/mol) and the universal gas constant R. (J/mol/K). Some examples of the surface mechanism used are listed for clarification, all reactions and corresponding parameters are listed in a table in Appendix A2.

$$k_f = A_r T^{\beta} \exp\left(-\frac{E_a}{RT}\right) \qquad [4.49]$$

$$CH_4 + Ni(s) \leftrightarrow CH_3 + NiC(s)$$

$$NiHC\,(s) + Ni\,(s) \leftrightarrow NiH\,(s) + NiC\,(s)$$

$$2\,NiH\,(s) + NiO\,(s) \leftrightarrow 2\,Ni\,(s) + H_2O$$

In order to create an accurate model with the CHEMKIN algorithm, the correct surface reactions with accompanying coefficients must be supplied. A relatively new method for obtaining these coefficients is by using Density Functional Theory. This theory is based around the fundamental behaviour of individual atoms and electrons. Going back to table 4.1, this is the appropriate length scale to evaluate surface kinetics.
For IR SOFCs, a complete surface mechanism for the methane reforming has already been developed by (Hecht et al., 2005), and reused in slightly adjusted form by (Yurkiv, 2014). It goes far beyond the scope of this thesis to recreate the surface mechanism from scratch. The adjusted version of this surface mechanism is used in the final model, to simulate the methane reforming process inside the fuel channels. This mechanism is available at ("Detchem.com," 2021). Appendix A4 lists the downloadable text files as well. They are slightly modified so that they're compatible with the latest version of Fluent (19.x).

ACCURACY OF DENSITY FUNCTIONAL THEORY CALCULATIONS

The basis of DFT lies on the fundamental equations of quantum mechanics. This fundamental nature makes it possible to predict a wide variety of material properties ranging from thermal conductivity to the colour of the material.
In some cases, these results are perfectly reproduced in experiments. In order cases not so much. The important question that must be answered is, how accurate are DFT calculations? A book on DFT provides some answers (Sholl & Steckel, 2009).
The overall accuracy of this theory depends on multiple ideas that need to be considered separately. A useful distinction between physical and numerical accuracy is a good starting point. For physical accuracy, the difference in a certain material property between DFT predictions and experimental results are compared. Numerical accuracy is a measurement for how well a calculation is converged. The distinction between these abstract concepts are illustrated in figure 4.7 as well.

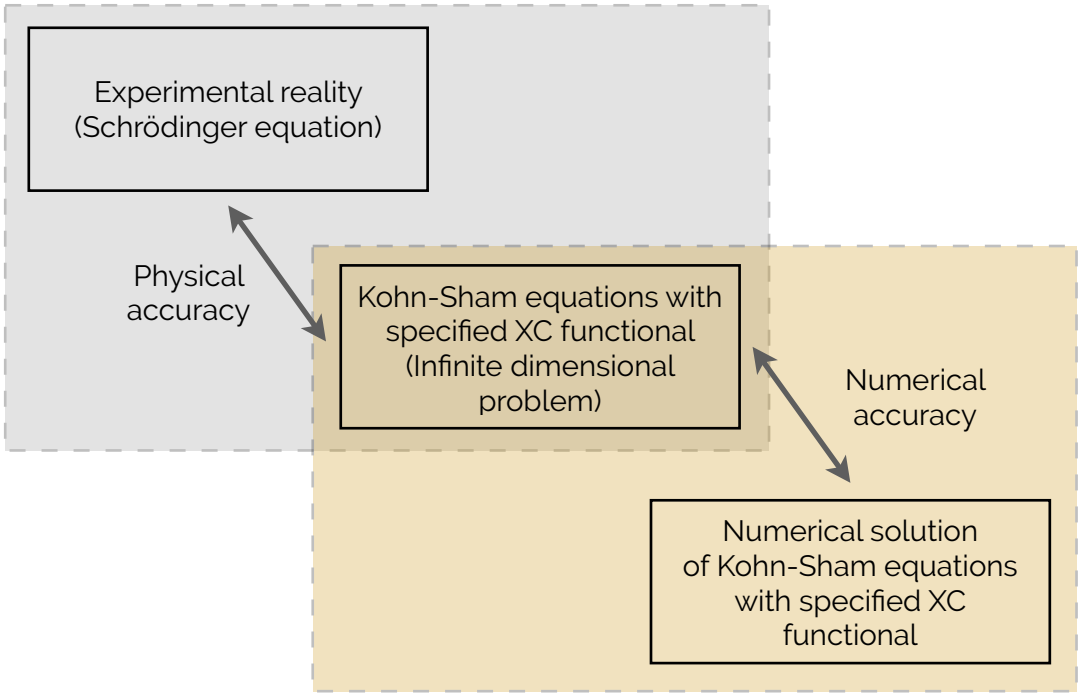

Figure 4.7 - Illustration of the distinction between physical and numerical accuracy of DFT (adjusted from (Sholl & Steckel, 2009))

Numerical accuracy is assessed by how well a calculation is converged. Just as in CFD problems, much time and attention is put in the numerical accuracy problem.
At the core of each DFT calculation, the ground-state for the electrons of a well-defined atomic nucleus is determined. This is done mathematically by solving the Kohn-Sham equation for a periodic set of identical nuclei (set of unit cells). This problem in the continuous form has infinite dimensions because the single-electron wave function in the Kohn-Sham equation are continuous functions of the spatial coordinates. Any solution found numerically, uses an approximate estimation of this otherwise continuous wave function.
To assess the accuracy of a numerical calculation, all the approximations that are invoked must be examined separately. For plane-wave DFT calculations the critical estimations are the number and density of k-points used to sample the k-space, and the energy cutoff used to define the plane wave numerically. This cutoff is similar to a cutoff made to the tails of a normal distribution.
When both the energy cutoff and k-point density are high enough, the numerical solution can converge to the true mathematical solution.
The KS equations are solved iteratively, which means each iteration the convergence is compared to a specified convergence criterion. It is obvious that this criterion must be sufficiently strict as well.

There is no cut-and-dry answer to the degree of physical accuracy of a DFT prediction. Predictions can be accurate to well within a 1% mean absolute error in some cases. In others, mean absolute errors compared to experimental data are over 10%.
For small and simple molecules, such as methane, hydrogen and other gaseous species found in IR SOFCs, better physical accuracy can be achieved. The unit cells that are evaluated in DFT assume inner electron shells are inert. This simplification has no effect on small elements, as there is no inner electron shell present. The inaccuracy in results start to grow when atoms and molecules that incorporate transient metals and beyond are considered. This is the reason why not many DFT studies can be found on lanthanides and actinides.
To determine the physical accuracy beyond this trend is somewhat hampered, by two causes.

1. Many studies using DFT calculations are only interested in relative performance of a material. In material selection studies, density functional theory can reliably predict that material A will be significantly better than material B and C. In most cases this result is good enough, and no absolute comparison to real experiments are required and therefore omitted.
2. In other cases it is not even possible to compare a DFT prediction with experimental data directly because there isn't any. DFT is used to explore the material properties of a practical infinite amount of alloys and reaction mechanisms. Experimental data that is unambiguously comparable to the DFT prediction may not be available.

The chapter on the accuracy of DTF calculations concludes with the remark that in order to make meaningful judgments about the physical accuracy, you must become familiar with the state-of-the-art literature (both computational and experimental) in the field of interest. This lies outside the scope of this thesis. Both (Hecht et al., 2005) and (Yurkiv, 2014) compared the reaction mechanism to experimental results and concluded that this mechanism does a good job in reproducing the data and certainly captures all the trends observed inside methane reformers.

4.7 - Conclusions

This chapter concludes the literature study. With the information provided in this chapter, a modelling approach is chosen.
From the first two sections, we can conclude that a physical, steady-state model based on Nernst equation is the best approach. There's no need for a transient scheme, as this creates unnecessary complexity and possibly for divergent behaviour.

The model will be created in ANSYS Workbench, with SpaceClaim ICEM CFD and Fluent. The appropriate length scales can be created in these meshing softwares. Fluent has the capabilities to run 2D cases, 3D cases and implement the CHEMKIN reaction mechanism as well.
A 3D modelling approach is selected, because the fuel cell module and surface mechanism require a 3D domain.

With this selection of approaches, solving schemes and programs a model can be created that can handle all physical processes relevant for the fuel cell operation and methane reforming in one coupled system of equations.
Areas where carbon deposition might occur first can be identified based on local conditions such as temperature, pressure, and mole fractions of the various products and reactants. With the use of the CHEMKIN reaction mechanism, all intermediate surface species can also be calculated.

5 - Model description

This chapter explains how the model has been set up. Geometry, cell zones and boundary conditions are all shown first. All physical constants and variables that are required to solve all the equations listed in the previous chapter are also given here. All the used conservation equations are also listed here.
Before the model is solved, a mesh study showing mesh independence is also provided in this chapter. All the results are covered in the next chapter. For the complete picture on how to replicate or re-run this model, see the Appendix A3 at the end of this thesis. Some (common) errors and technicalities specifically for this model are also documented in Appendix A3.4.

5.1 - Conservation equations

The conservation equations that the solver works with are listed in this section. The electron and ion conservation equations, and other depending equations related to the fuel cell module have already been discussed in chapter 4 (equations 4.31 and 4.32).
Besides conservation of charge, the model also respects the conservation of energy, momentum and mass. In this section each equation is further explained.

CONSERVATION OF ENERGY

The steady-state energy conservation equation solved by Fluent is shown in equation 5.1. This is the equation evaluated in the fluid domains. For the solid regions, equation 5.2 is valid. The collective term E, defined in equation 5.3, consists of the sum of energies in the form of enthalpy (h), pressure (**p**) and kinetic energy (v). For incompressible ideal gasses, equation 5.4 defines the sum of sensible enthalpy of a species. The sum itself represents the enthalpy of the mixture. The last term in equation 5.4 is added, because of the assumption that the mixture behaves as an incompressible ideal gas. The (effective) conductivity is defined by κ. In case of turbulent flows, this term consist of two separate conductivities. In order to leave the equations in a familiar form, the density ρ is also shown. But by combining equation 5.4 and 5.3, the density is no longer present in the set of equations. The diffusion flux J_j of all species j are added in the next term in the energy equation. Viscous dissipation of energy is covered by the final term.
Finally all the source and sink terms removing energy from the system are added by S_h. In this case, the heat of the reactions defined by equation 5.5 are added. The enthalpy of formation of species j is defined by h_j^0, M_j is the molecular weight and $\mathscr{R}_j$ represents the volumetric rate of creation (or consumption) of each species in molar units. No other heat sources are present in the model.

$$\nabla \cdot \left(\bar{v} \left(\rho \mathrm{E} + p \right) \right) = \nabla \cdot \left(\kappa \cdot \nabla T - \sum_j h_j \bar{J}_j + (\bar{\tau} \cdot \bar{v}) \right) + \mathrm{S}_h \qquad [5.1]$$

$$\nabla \cdot \left(\bar{v} \rho h \right) = \nabla \cdot \left(k \nabla T \right) \qquad [5.2]$$

$$\mathrm{E} = h - \frac{p}{\rho} + \frac{v^2}{2} \qquad [5.3]$$

$$h = \sum_j Y_j \cdot h_j + \frac{p}{\rho} \qquad [5.4]$$

$$S_h = -\sum_j \frac{h_j^0}{M_j} \mathscr{R}_j \quad [5.5]$$

CONSERVATION OF MOMENTUM

Fluent solves the momentum equation defined by equation 5.6. Gravity is enabled in the model and is taken into account by the ρ•g term. External forces (F) are not present in this case, but Fluent also adds forces acting on the fluid caused by porous zones in this term. Porous zones are present in the model, and this is where these forces are evaluated.
The stress tensor τ is the sum of all the forces acting along the surfaces of the small control volume. The viscosity is denoted by μ. The second term inside the brackets is the effect of volume dilation, the unit tensor is defined by I in this equation.

$$\nabla \cdot (\rho \cdot \bar{v} \cdot \bar{v}) = -\nabla p + \nabla \cdot (\bar{\bar{\tau}}) + \rho \cdot \bar{g} + \bar{F} \quad [5.6]$$

$$\bar{\bar{\tau}} = \mu \left[(\nabla \bar{v} + \nabla \bar{v}^T) - \frac{2}{3} \nabla \cdot \bar{v} I \right] \quad [5.7]$$

CONSERVATION OF MASS AND CONTINUITY

Equation 5.8 is the general conservation of mass equation, valid for both compressible and incompressible flows. The source terms S_m consists of several local sources and sinks for oxygen, hydrogen and water added by the fuel cell module. This way, Fluent allows the user to transfer mass from one species to another (the essence of chemical reactions). Since all the mass remains in the continuous phase e.g. no evaporation to a dispersed phase occurs, the sum of all these sources and sinks is zero over the entire domain. This is shown by equation 5.9.
The CHEMKIN mechanism also supplements this term with all the species that are formed and consumed during the methane reforming process. The source terms added by the fuel cell operation are defined by equations 5.10 to 5.12. For more details on these equations, see section 4.5.

$$\nabla \cdot (\rho \bar{v}) = S_m \quad [5.8]$$

$$S_m = S_{H_2O} + S_{H_2} + S_{O_2} = 0 \quad [5.9]$$

$$S_{H_2O} = -\frac{M_{W,\,H_2O}}{2F} \cdot R_a \quad [5.10]$$

$$S_{H_2} = \frac{M_{W,\,H_2}}{2F} \cdot R_a \quad [5.11]$$

$$S_{O_2} = \frac{M_{W,\,O_2}}{4F} \cdot R_c \quad [5.12]$$

5.2 - Geometry

The model consists of two fluid channels, both with an inlet and outlet. In all figures, the top channel is the fuel channel (anode side) and flows from left to right. The bottom channel (cathode

side) is the air channel, air flows from right to left. This type of setup is called counter-flow. Other options are co-flow, or when the channels are perpendicular to each other cross-flow. The left-right naming convention is consistent throughout the text as well, and can be seen in figures of the y-z plane such as figure 5.4. The physical dimension and characteristics of the geometry are shown in figure 5.1 and table 5.1 below. Figure 5.1 shows the front view of the domain. The length of the channels in the direction of the page (z-direction) is 90 mm. This is the only dimension not shown in this figure.

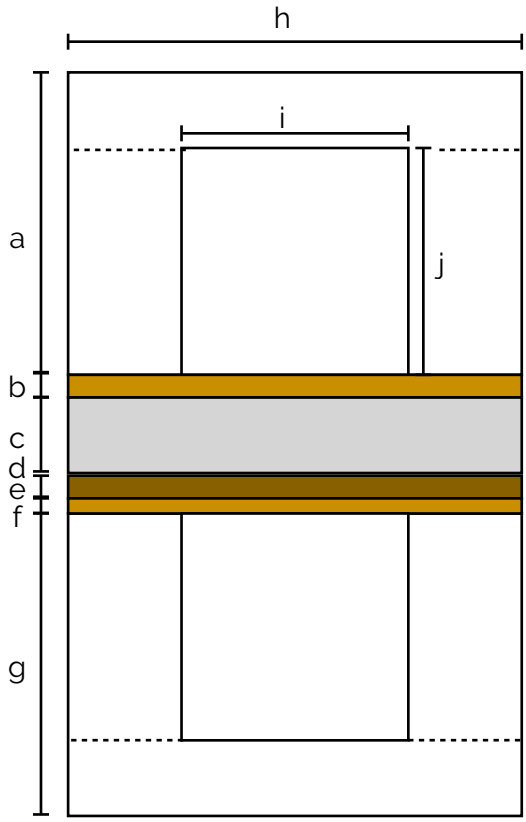

Figure 5.1 - Overview of channel and layer geometry in the x-y plane

	Name	Length (mm)		Name	Length (mm)
a	Anode Current Collector	$1{,}2 \cdot 10^{0}$	f	Cathode Support	$1{,}3 \cdot 10^{-2}$
b	Anode Support	$2{,}0 \cdot 10^{-2}$	g	Cathode Current Collector	$1{,}2 \cdot 10^{0}$
c	Anode Catalyst	$4{,}0 \cdot 10^{-1}$	h	Global Width	$2{,}0 \cdot 10^{0}$
d	Electrolyte	$8{,}0 \cdot 10^{-3}$	i	Channel Width	$1{,}0 \cdot 10^{0}$
e	Cathode Catalyst	$2{,}5 \cdot 10^{-2}$	j	Channel Height	$1{,}0 \cdot 10^{0}$

Table 5.1 - Dimensions of domain in the x-y plane

5.3 - Cell zones

Figure 5.2 shows the cell zones and table 5.2 lists important characteristics unique to each zone. In order to setup the fuel cell mode, according to the Fluent manual, the porous media (zones C, D, F, and G) could be modeled as either a solid or a fluid as long as this choice is made consistent throughout the model. This might be true, but in combination with the surface chemistry in some of the same domains, only the fluid type works. The electrolyte is set to fluid as well, to allow for ion transport. In all other aspects such as heat transfer, it is modelled as a solid. The current collectors are all solid materials.

Block	Cell zone name	Type	Bock	Cell zone name	Type
A	Anode Current Collector	Solid	F	Cathode Catalyst	Fluid
B	Fuel Channel	Fluid	G	Cathode Support	Fluid
C	Anode Support	Fluid	H	Air Channel	Fluid
D	Anode Catalyst	Fluid	I	Cathode Current Collector	Solid
E	Electrolyte	Fluid			

Table 5.2 - Overview of cell zones and their corresponding types

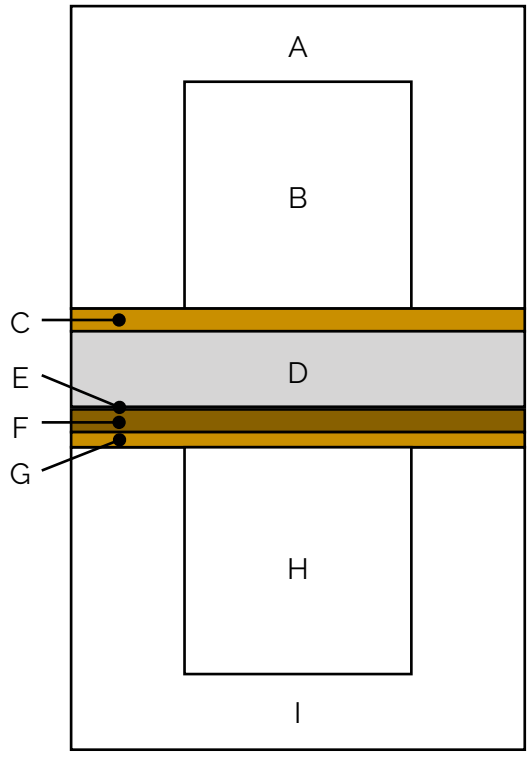

Figure 5.2 - Distribution of cell zones, in the x-y plane. Cell zones stretch out over the entire domain in the z-direction

5.4 - Boundary conditions

Figure 5.3 and 5.4 show all boundary conditions in each subdomain. For case 1 and 2 (see section 5.5), the model is run in a co-current flow, with both inlets set to "fuel" on the left side. The mixture composition is different however, this is done to replicate the study by Hecht et al. as closely as possible. In case 3, the model is run in a counter-current flow, with fuel flowing from left to right and air from right to left.

ACTIVE SURFACES FOR REFORMING MECHANISM AND ION TRANSPORT

For each surface that separates solid from fluid zones or are part of the overall domain border, the wall boundary condition is chosen. Additionally, the surfaces of the electrolyte are defined as walls as well, so that the methane reforming mechanism can take place on the anode side of the electrolyte. The wall boundary condition also prevents gasses to migrate through the electrolyte, as this zone is modelled as a fluid. As stated in the ANSYS User Manual, the oxygen ions can migrate trough any surface encompassing the electrolyte, when the electrolyte is set as a fluid domain. These surfaces are indicated by the coloured dashed line in figure 5.3.
The coloured solid surfaces (extending into the sheet along the z-axis in figure 5.3) is where methane reforming can take place with the surface mechanism can take place.

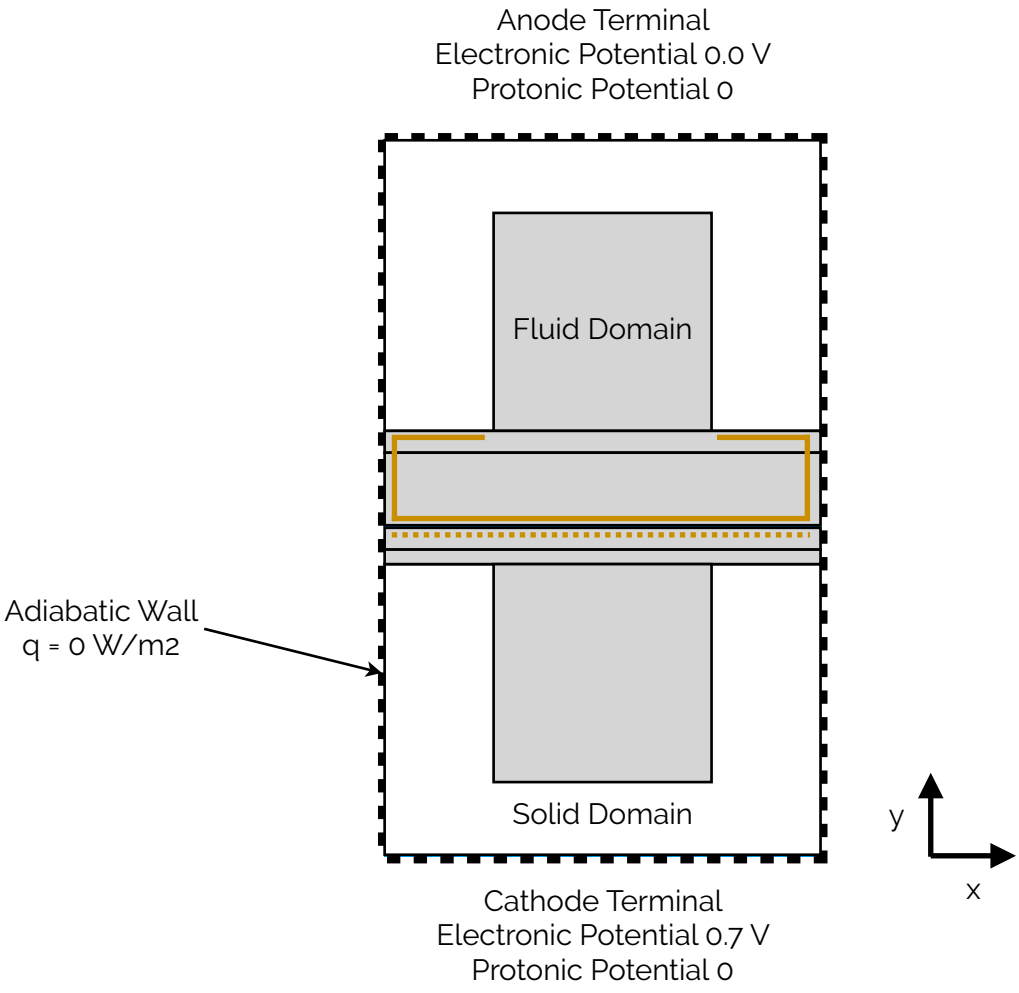

Figure 5.3 - Boundary conditions viewed from x-y plane

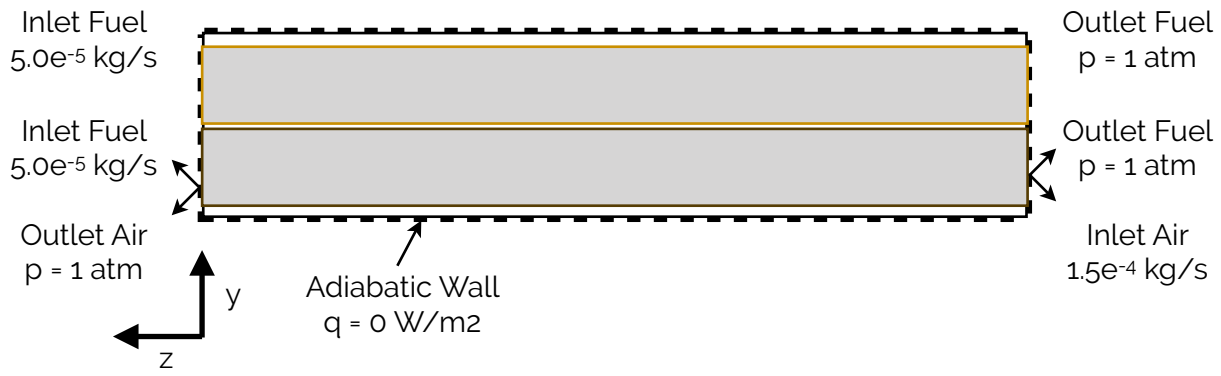

Figure 5.4 - Boundary conditions viewed from y-z plane

5.5 - Mesh study

In order to judge the results on their physical accuracy, a couple of important features of the model must be evaluated. In this section, it will be shown that the mesh used provides results that are independent of the mesh parameters.
Both the flow characteristics and the reforming mechanism are run with three different meshes, traditionally called coarse, medium and fine. The absolute mesh sizes are chosen such that the medium and fine mesh result in the same solution, where small deviations within reasonable limits are allowed. The mesh dimensions and features such as cell count are shown in table 5.3.

Item	Course	**Medium**	Fine
Type	Hexahedral	**Hexahedral**	Hexahedral
Nodes	288,754	**486,838**	1,641,618
Size	23.4 Mb	**47.6 Mb**	247.2 Mb
Orthogonality	0.74	**0.88**	0.94

Table 5.3 - Mesh sizes en quality

The overall quality of the mesh increases as the mesh is refined, because relatively more cells are added in the z-direction than both the x- and y-direction. The fine mesh consists of cells resembling perfect cubes, whereas the course mesh is build up of more oblate rectangles.
The quality of all the meshes is high to very high in terms of orthogonality and aspect ratio. This is due to the hexahedral mesh type with flow all flow directions perpendicular to a cell face. The overall domain is similarly shaped as a single cell, so there is zero skewing or warping necessary for any of the mesh cells.

For the medium mesh is qualitatively just as good as the finer variant. This has been tested for all cases. Consequently, all the remaining studies have been done with the medium sized mesh. The fuel cell module hasn't explicitly been tested for mesh independence. Since mesh independence for the surface mechanism has already been demonstrated, it is not necessary to show this for the fuel cell model as well.

5.6 - Case setups

Three different cases are run using the model described. Each case uses the some unique boundary conditions as described in this section. All model characteristics discussed up to this point are valid for all three cases.
The first case simulates the same case as in the studies in where the surface mechanism was developed. The results are compared to these studies to verify this part of the model has been setup correctly. The initial fuel composition is listed in table 5.4. The accompanying mass flow rate per inlet are listed in table 5.5. The mass flow rate scales proportional to the projected area of the inlet. This ensures that the inlet velocities are the same. All resulting mean inlet velocities are in the order of ~1 m/s.
Cell zones C to G are set to 100% porosity, meaning there are no solids to interfere with the fluid flow. Furthermore the walls encompassing the electrolyte are set to internal walls, so that the gasses from the top and bottom channel can freely mix.

The second case tests the surface mechanism of methane reforming on a different fuel composition. This fuel composition is more common in SOFCs during standard operation. Otherwise, the case setup is identical to the first.

Finally, the complete fuel cell is enabled. Fuel flow and oxygen flow are setup as described in section 5.3. The fuel composition is identical as to case 2, but now enters pre-mixed through a single inlet. The cell zones C to G are now setup to represent a complete fuel cell, with respect to porosity, ionic and electronic conductivity. The variables that are used in this particular case are listed in table 5.6.

INLET CONDITIONS PER CASE

Each case uses slightly different inlet conditions. As shown in figure 5.4, case 1 and 2 feature a co-flow setup and case 3 a counter-flow setup. Figure 5.5 shows the front view of every inlet to clarify where the gasses enter and leave the domain. The inlets and outlets are numbered from top to bottom (1 to 6). To replicate the studies done by Hecht and Yurkiv, some inlets are disabled in the first two cases. In the third case, only the electrolyte is setup as a wall.

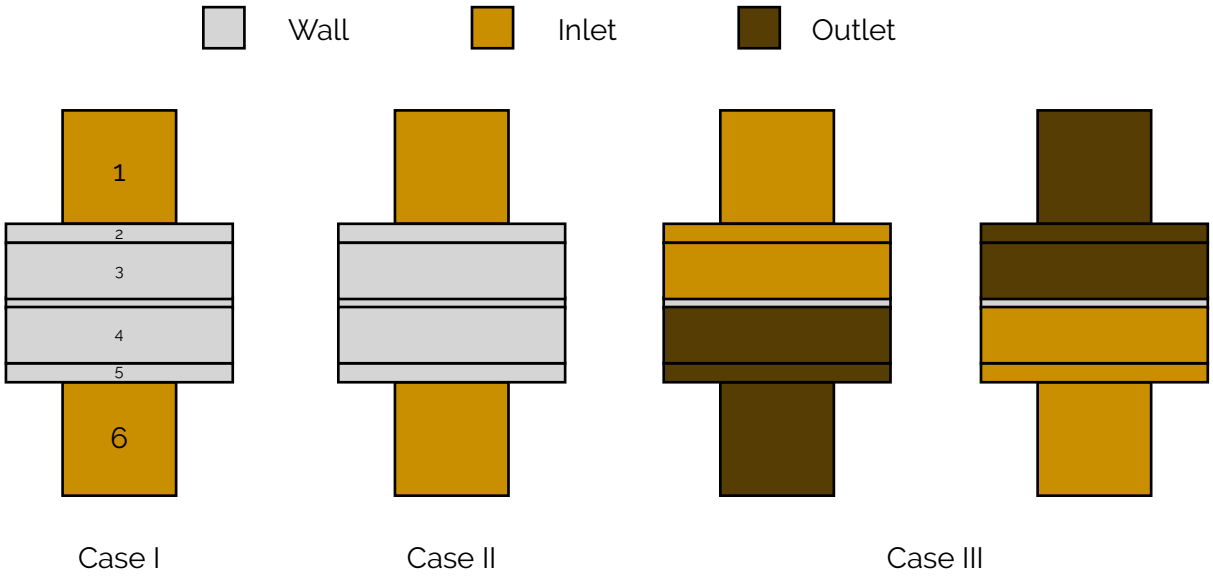

Figure 5.5 - Front view of inlets for each case

	Case 1					Case 2		Case 3			
n	CH4	H2O	H2	CO2	Ar	CH4	H2O	CH4	H2O	O2	N2
1	0.2	0	0.028	0	0.772	1	0	0.34	0.66	0	0
2	-	-	-	-	-	-	-	0.34	0.66	0	0
3	-	-	-	-	-	-	-	0.34	0.66	0	0
4	-	-	-	-	-	-	-	0	0	0.21	0.79
5	-	-	-	-	-	-	-	0	0	0.21	0.79
6	0	0.5	0	0.5	0	0	1	0	0	0.21	0.79

Table 5.4 - Fuel composition for each inlet per case

Inlet	Case 1 Mass Flow [kg/s]	Case 2 Mass Flow [kg/s]	Case 3 Mass Flow [kg/s]
1	2E-04	1E-07	1.6E-08
2	-	-	8E-10
3	-	-	2E-08
4	-	-	1.3E-08
5	-	-	2.5E-08
6	2E-04	2E-07	5E-07

Table 5.5 - Mass flow rate for each inlet per case

Parameter	Value	Unit
Cell Voltage	0.700	V
Cell Open Voltage	1.034	V
Thermal Conductivity	$4.54 \cdot 10^{-2}$	W/m•K
Porosity anode	0.3	-
Porosity cathode	0.85	-
Diffusivity	$3 \cdot 10^{-5}$	m^2/s
Anode Reference Density	10000	A/m^2
Anode Concentration Exponent	0.5	-
Cathode Reference Density	20	A/m^2
Cathode Concentration Exponent	1	-
Exchange Coefficient (all)	2	-
Total Leakage Current	0	A
Electrolyte Projected Area	1.80	m^2
CO Electrochemistry source	Disabled	-

Table 5.6 - Parameters fuel cell mode used in Case III

6 - Results & Discussion

In this chapter the results of three simulations are presented. Firstly, just the reforming mechanism without any cell potential is simulated. It is important to verify that the reforming mechanism is showing the similar results as in earlier studies (Hecht et al., 2005), (Yurkiv, 2014). These studies used another CFD program, but the same operating conditions.
The next study uses another gas composition, more suitable for SOFC operation. This second case serves as an intermediate to the third case, where the fuel cell module is activated as well. For each case the change in mixture composition in the channel is shown, as well as the temperature fluctuations inside the channel and the site species concentrations.

The usefulness of chemical equilibrium calculations was discussed in chapter 4. In order to verify if the CHEMKIN surface mechanism works, we can compare these results with each other. To find the composition of a gaseous mixture at equilibrium, no complex CFD model is required.
A simple MATLAB script (shown in Appendix A1), combined with the Gibbs free energies of formation as provided in chapter 4 are enough to find the gas composition at chemical equilibrium for the inlet conditions used in the Fluent cases afterwards. See figure 6.1.

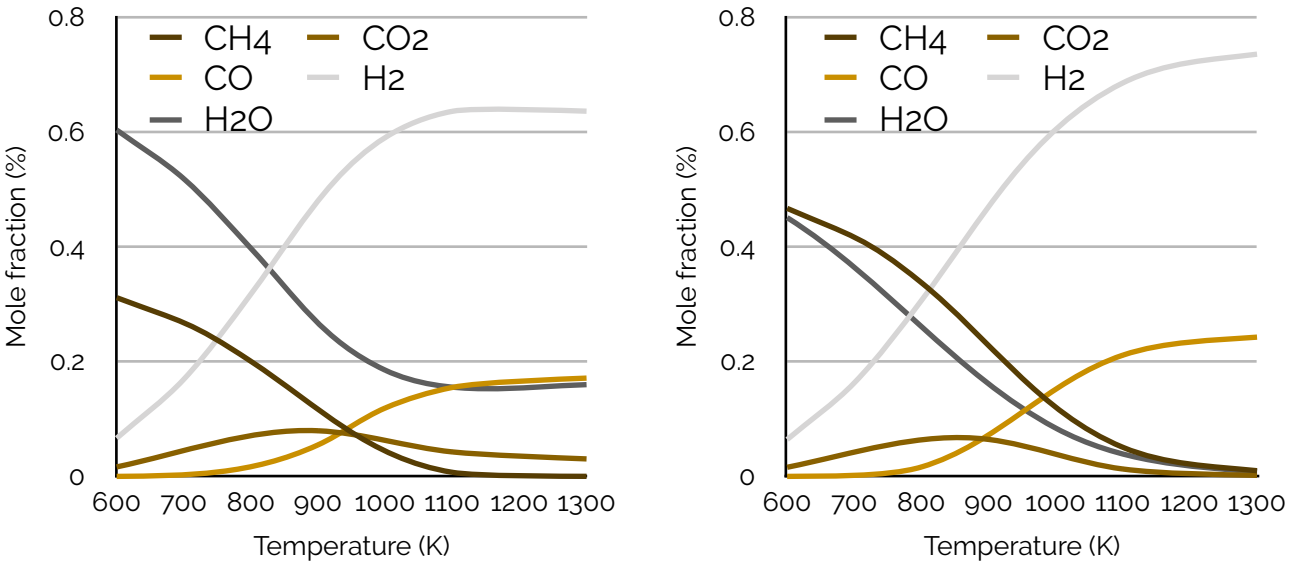

Figure 6.1 - Chemical equilibrium of methane and water mixtures at p = 1 bar and varying temperatures. S/C ratio 2:1 (left) and S/C ratio 1:1 (right)

6.1 - Case I

This case reproduces the results from (Hecht et al., 2005) and (Yurkiv, 2014). Figure 6.2 shows the temperature distribution inside the channel. The upper channel is defined by cell zones B, C, and D, shown in figure 5.2 in the previous chapter. The inlet of this upper channel is numbered as 1, in figure 5.5. The lower channel consists of zones F, G, and H, with inlet number 6. The average temperature in the x-y plane is used at each increment along the z-axis.

The inlets are depicted on the left side at z(0) and the gases exit the channel on the right side only (at z(0.09). This will be the case most plots in this chapter. The channel length is given on the x-axis in meters. The total channel length is 0.09 m.

The endothermic nature of methane reforming is clearly visible. This plot shows the surface average of the temperature in the upper and lower channel. The temperature in the upper channel dips further, because the active surface where reforming takes place is located on the upper channel. Ultimately, the temperatures of both channels converge to a single value mainly due to diffusion.

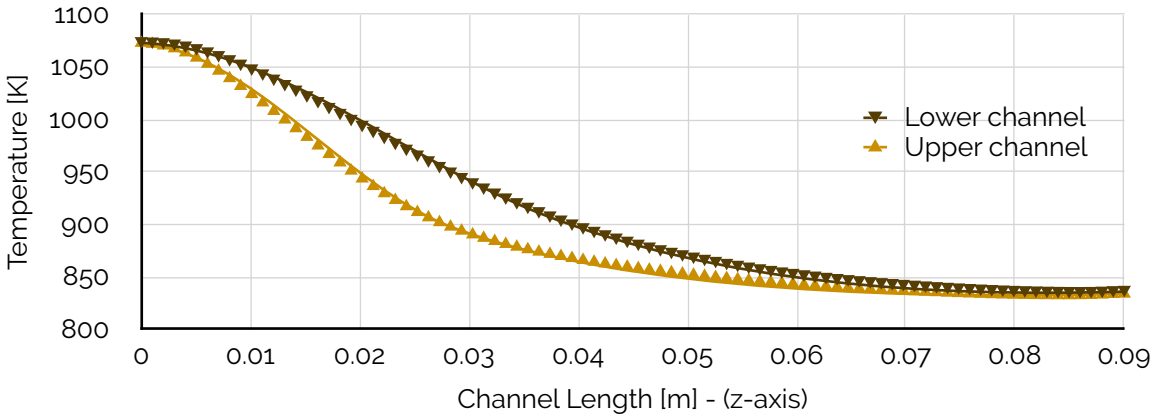

Figure 6.2 - Averaged temperature distribution along upper and lower channels

Figure 6.3a and 6.3b shows the progress of reforming inside the channel. As can be seen in table 5.4 in the previous chapter, the top channel is fed with methane, argon and trace amounts of hydrogen. The bottom channel is fed by carbon dioxide and water is a 1:1 ratio. These values can be seen on the left side of the figures. The rate of reforming can be estimated from these figures, in combination with the mass flow rates and other operating conditions.

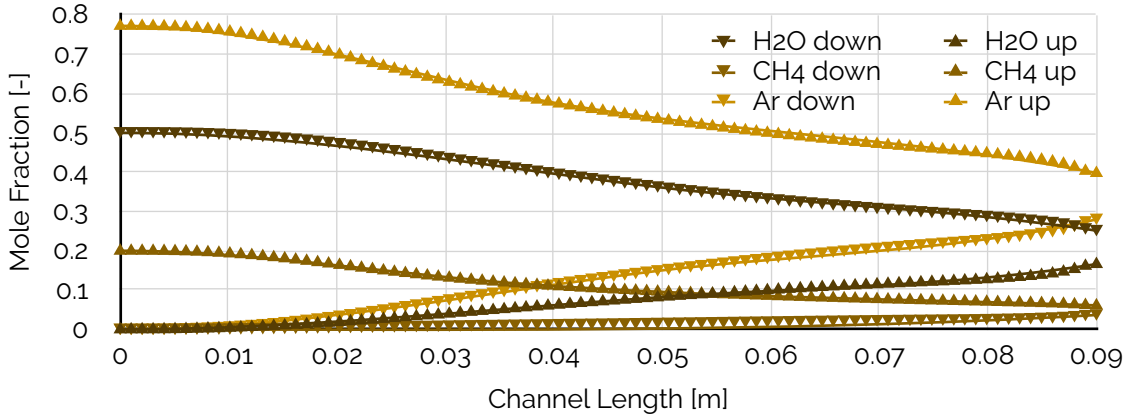

Figure 6.3a - Averaged species distribution along upper and lower channels for H_20, CH_4 and Ar

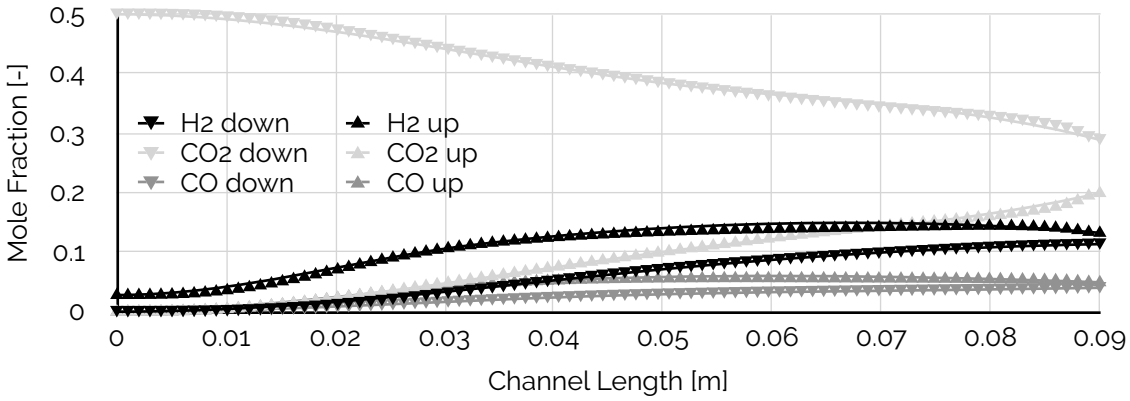

Figure 6.3b - Averaged species distribution along upper and lower channel for H_2, CO_2 and CO

COMPARISON TO PREVIOUS STUDIES

This simulation with identical operating conditions has been done before. Results from these studies are compared to this simulation in Figure 6.4. This figure is adapted from (Hecht et al., 2005). The x-axis has been converted to SI-units used in Fluent.

This has been approximated by equation 6.1, which can be used to convert from (kg/s) to (sccm) (standard cubic centimeters per minute). The approximation lies in the assumption that the compressibility factor (Z_n) of the mixture is unity in these conditions. This is valid since the temperatures are relatively high and the pressure throughout the channel is near atmospheric conditions.

The results of this simulation are plotted in the figure. The lines and dots overlap very well. This shows that the conversion rate is the same in both studies. Furthermore, since all dots match their corresponding lines, it also shows that the same relationship between these species (which can only vary via the reaction mechanism) is realised.

$$1\ \frac{kg}{s} = 6.0 \cdot 10^7 \cdot \frac{Z_n \cdot R \cdot T_n}{p_n \cdot M}\ SSCM \qquad [6.1]$$

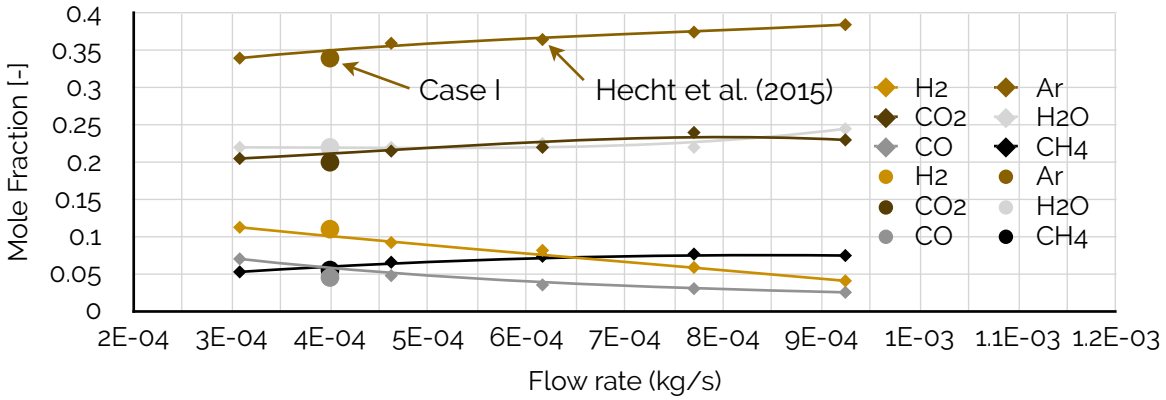

Figure 6.4 - Outlet conditions of Case I compared to results of equivalent study

SURFACE SITES DENSITY

An important metric resulting from this simulation is the resulting surface site coverage throughout the channel. Initially, all sites are free nickel. Methane and the other species can attach to these sites and participate in the surface kinetics. Reformed species leave the surface and a free nickel site is left behind. It turns out that only 4 species out of 13 make out the bulk of the site concentration. This is corroborated by several studies shown in table 6.1. In each case, the same four species came up as the main surface species present.

The site coverages in the x-y directions at a certain point inside the channel where practically constant. For pure nickel, the site coverage increased along the channel since less methane is present in the mixture to bind to an empty nickel site. The other species in table 6.1 increased in coverage along the z-direction.

	Blaylock et al. 1997	Janardhanan & Deutschmann, 2006	Hecht et al., 2005	Hoffman et al. 2018	Case I
Ni	0.77	0,58 - 0,66	0,60 - 0,70	0,76 - 0,77	0,28 - 0,59
H*	0.15	0,10 - 0,15	0,05 - 0,12	0,05 - 0,07	0,26 - 0,48
CO*	0.077	0,19 - 0,25	0,10 - 0,30	0,05 - 0,11	0,15 - 0,25
O*	$3{,}5 \cdot 10^{-4}$	n/a	0,00 - 0,15	0,07 - 0,11	$3{,}0 \cdot 10^{-4}$ - $6{,}7 \cdot 10^{-4}$

Table 6.1 - Fractions of site species coverage over the entire channel compared to other simulations (coloured solid surfaces in figure 5.3)

Finally, the methane reforming surface species fractions are plotted in figure 6.5. The absolute values of these fractions are very small, otherwise they would have been listed in table 6.1 as well. The absolute values seen in this plot are therefore probably not accurate. The order of magnitude of the residuals is in the same range as these site coverages. It is clear from these minute concentrations and the fact there are still many empty nickel sites, that this part of the reforming process is not rate determining. Naturally, if the carbon coverage increases it would become the rate determining factor eventually.

Furthermore, the species concentrations decrease as more hydrogen atoms are separated from the methane. The final step, where CH* is split into C* and H* results in two species that both

accumulate much more. This concentration of C* is an important starting point to investigate resulting carbon formation further.
Most studies don't provide local conditions (temperature and species composition) but assume that inlet temperature and chemical equilibrium are accurate enough.
The figures in this section and the next, prove that these assumptions are not accurate and provide more reasonable values as well.

Figure 6.5 displays some numerical artefacts at the end of the channel. The site coverages suddenly drop a few orders of magnitude. This is due to how Fluent calculates the surface coverage density. The outlet shares a vertices with a wall where no surface chemistry is allowed to take place. Because of this, site coverages along this vertices are assumed to be zero in the averaged weighted area calculation.

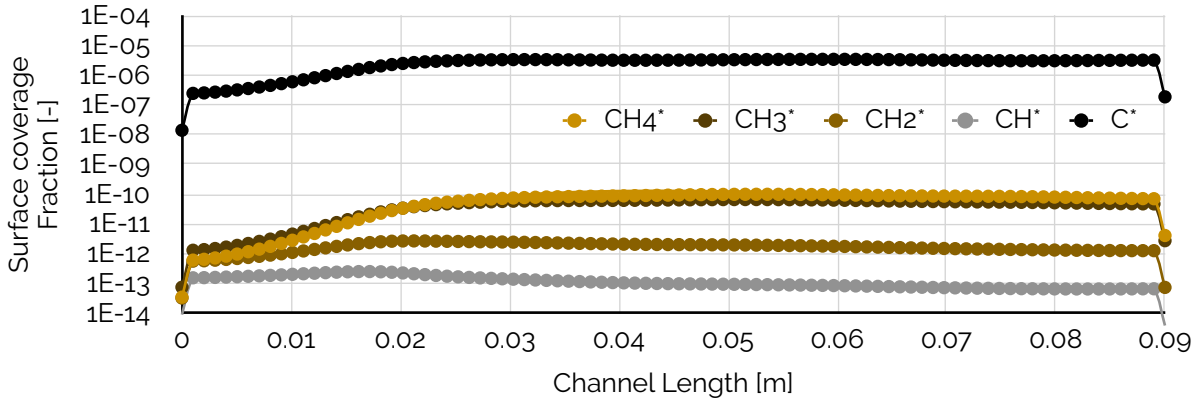

Figure 6.5 - Surface species of some species involved in methane reforming

SIMULATION OVERVIEW

The simulation was run for 20.000 iterations. After this point, no changes in the solution were detectable, the residues did not further decrease as well. The residues decreased steadily without any oscillations. The under relaxation factors where increased as the simulation progressed towards convergence. This was done by necessity, the solution will diverge if too high under-relaxation factors are used to soon in the solution process. This is shown in table 6.2. The final residues from each equation (for each case) are listed in table 6.6 at the end of this chapter.

URF	Iterations 0 - 500	Iterations 500 - 2.000	Iterations 2.000 - 20.000
Pressure	0.3	0.3	0.3
Density	0.5	0.5	0.5
Body Forces	0.5	0.5	0.5
Momentum	0.5	0.7	0.7
Species	0.5	0.9	0.999
Energy	0.7	0.9	0.99

Table 6.2 - Evolution of under-relaxation factors throughout the simulation

6.2 - Case II

This case differs only slightly from the first. The goal of this simulation is to further verify that the surface mechanism works correctly, but in this instance with a more realistic gas composition used in SOFCs. These details are given in the previous chapter.

COMPARISON TO CHEMICAL EQUILIBRIUM

In the previous section some results were compared to identical and similar studies. For this case study, the results are compared to chemical equilibrium of the species involved.
To ensure this equilibrium can be reached, the inlet mass flow is greatly reduced in this case. Figure 6.6a and 6.6b show the species distribution along the channels (same definition as in case I). The dashed lines in the same style represent chemical equilibrium of the species at those conditions (see also figure 6.1 for chemical equilibrium).

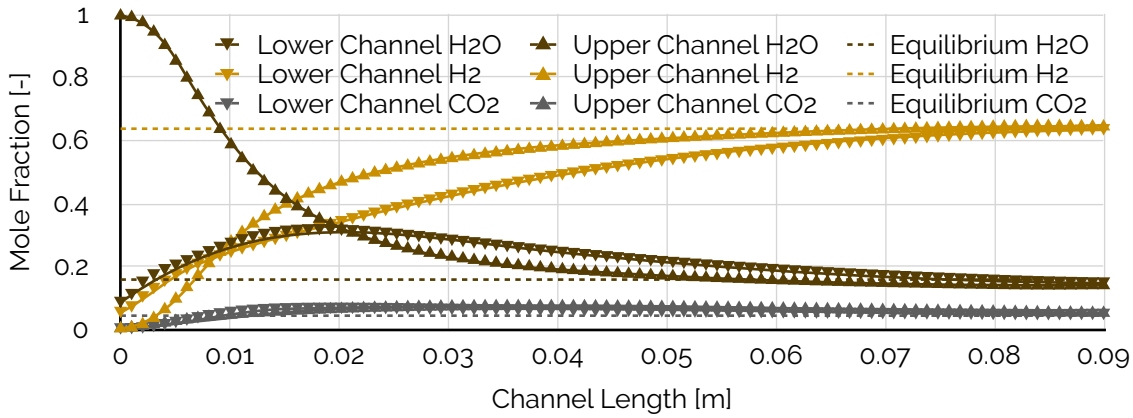

Figure 6.6a - Averaged species distribution along upper and lower channels for H_20, H_2 and CO_2

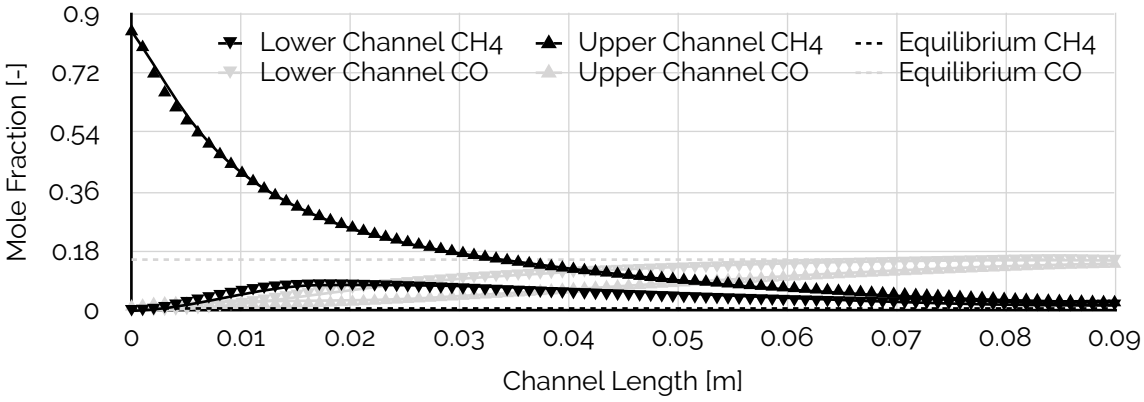

Figure 6.6b - Averaged species distribution along upper and lower channel for CH_4, CO_2 and CO

ESTIMATING ACTIVATION ENERGY AND REACTION ORDER

From the figures above, the operating conditions and equation 6.2, the activation energy for the overall reaction can be estimated. In literature, values for this activation energy and assumed reaction order vary quite substantially.

The reaction order can be estimated from the rate at which CH_4 is consumed. This is plotted again in figure 6.7. The half-life (the rate at which the concentration is halved) is plotted in this graph as well. It can be observed that the half-life remains constant, so it may be assumed that the reaction is first order in respect to the methane concentration. Only the time of the first halving is shorter. This is because the methane not only reacts, but also spreads to the bottom channel, as can be seen in figure 6.6b. As soon as the methane has dissipated, the concentration halves every 22.2 mm.
The average velocity inside the channel is 1.16 m/s. This is the averaged weighted velocity at the outlets of the channel. The concentration of methane is halved after at 22.2 mm inside the channel. The rate constant at 1073K for the overall reaction can be calculated by using equation 6.3 and is 36.21 s^{-1}. The same simulation has been done to obtain an estimate of the rate constant at 973 K and this resulted in 12.48 s^{-1}. Equation 6.4 can now be used to estimate the activation energy of the methane reforming reaction. The result is listed among other reported values adapted from (Fan, Van Biert, Thallam Thattai, Verkooijen, & Aravind, 2015) and (Mogensen, Grunwaldt, Hendriksen, Dam-Johansen, & Nielsen, 2011) in table 6.3.

$$k = A e^{-\frac{E_a}{RT}} \quad [6.2]$$

$$t_{1/2} = \frac{\ln 2}{k} \quad [6.3]$$

$$E_a = \frac{R \cdot T_1 \cdot T_2}{(T_1 - T_2)} \ln\left(\frac{k_1}{k_2}\right) \quad [6.4]$$

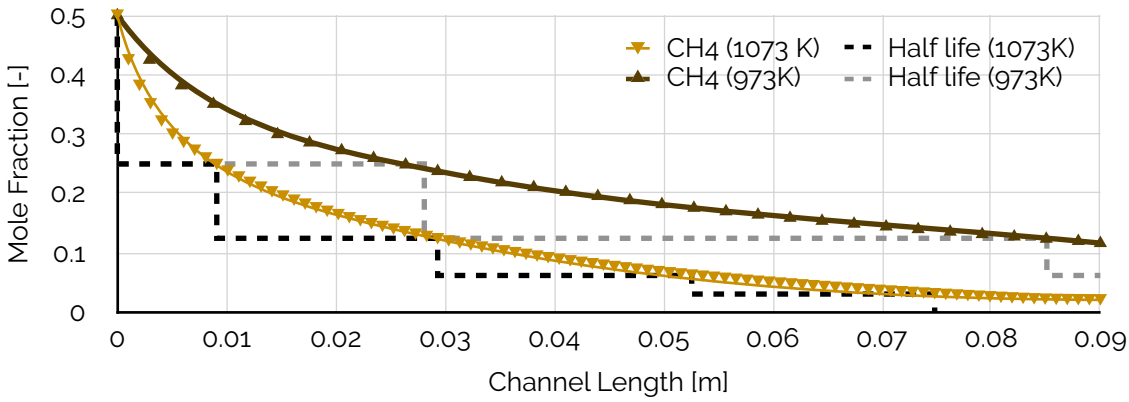

Figure 6.7 - Consumption of methane along the channel for 1073 K and 973 K

Study or Simulation	Rate Constant Expression	Reported Activation Energy
Case II	$k = p[CH_4]$	92
K. Achmed et al. 2000	$k = p[CH_4]^{0.85} \cdot p[H_2O]^{-0.35}$	95 ± 2
G. Brus et al. 2012	$k = p[CH_4]^{0.98} \cdot p[H_2O]^{-0.25}$	117
D.L. King et al. 2008	$k = p[CH_4]$	113 - 124
A. Lee et al. 1990	$k = p[CH_4]^{1.00} \cdot p[H_2O]^{-1.25}$	74 - 98

Table 6.3 - Comparison of reported activation energies in literature

SIMULATION OVERVIEW

The simulation was run for 45.000 iterations. The residues decreased steadily without any oscillations. It took slightly longer for this case to converge, since no inert gas was used here. It took a lot longer for the species equations to converge over the entire domain. The under-relaxation factors where increased as the simulation progressed towards convergence. This is shown in table 6.4. The final residues from each equation (for each case) are listed in table 6.6 at the end of this chapter.

URF	Iterations 0 - 500	Iterations 500 - 2.000	Iterations 2.000 - 45.000
Pressure	0.3	0.3	0.3
Density	0.5	0.5	0.5
Body Forces	0.5	0.5	0.5
Momentum	0.5	0.7	0.7
Species	0.5	0.9	0.999
Energy	0.7	0.9	0.99

Table 6.4 - Evolution of under-relaxation factors throughout the simulation

6.3 - Case III

The correct operation of the fuel cell module is the second half next to the surface mechanism. Case III simulates both models simultaneously.
The setup of this case is quite different with regard to inlets, outlets and gas composition, see the previous chapter for all the details.

SPECIES DISTRIBUTION

Figure 6.8a and 6.8b display the species distribution in the anode and cathode channel respectively. As listed in table 5.6 in the previous chapter, CO electrochemistry is disabled. It is assumed that CO oxidises with oxygen (not with oxygen ions), and therefore no additional charge-transfer occur via locally produced CO. In Fluent, the option exists to ignore CO electrochemistry to ensure this assumption holds. This is in agreement with a theoretical study on the contribution of CO electrochemistry in SOFCs (Hanna, Lee, Shi, & Ghoniem, 2014), and experimental data on the outlet gas composition.
The mole fraction of CH_4 at the outlet of the fuel channel is 0.1. This would correspond with a fuel utilisation factor of 80%. The mass flow rate of the cathode channel is much larger, this additional air flow helps to cool the channel. Because of this excess air flow, the mole fraction of oxygen drops much less than the water mole fraction increases. When a perfect stoichiometric oxygen supply was supplied a clear relation between these lines would be visible.

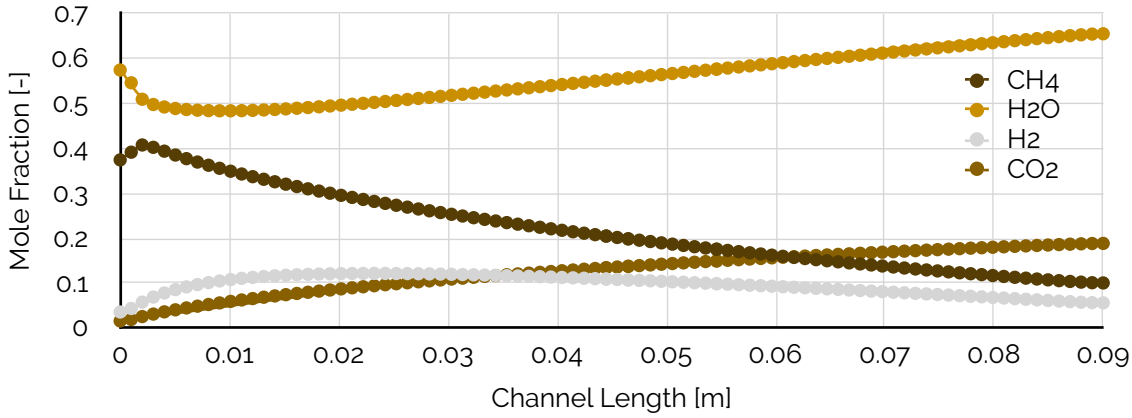

Figure 6.8a - Averaged species distribution along anode channel for CH_4, H_20, H_2 and CO_2

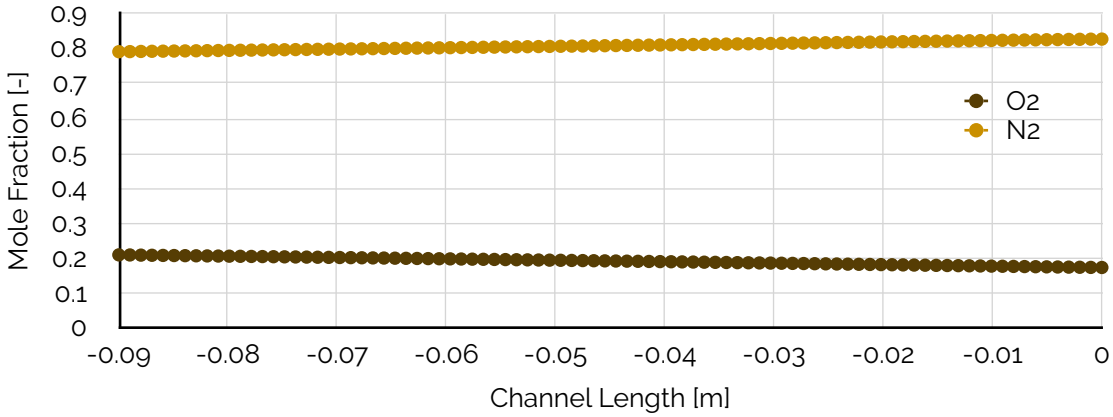

Figure 6.8b - Averaged species distribution along cathode channel for N_2 and O_2

CURRENT DENSITY COMPARISON

Figure 6.9 shows how the current density varies along the channel length. This figure plots how many electrons travel through the middle of the electrolyte layer (in the y-direction). The negative value is correct, as the electrons move from anode to cathode. In the domain used, this direction is negative. The average value over the entire length is 0.259 A/cm^2.

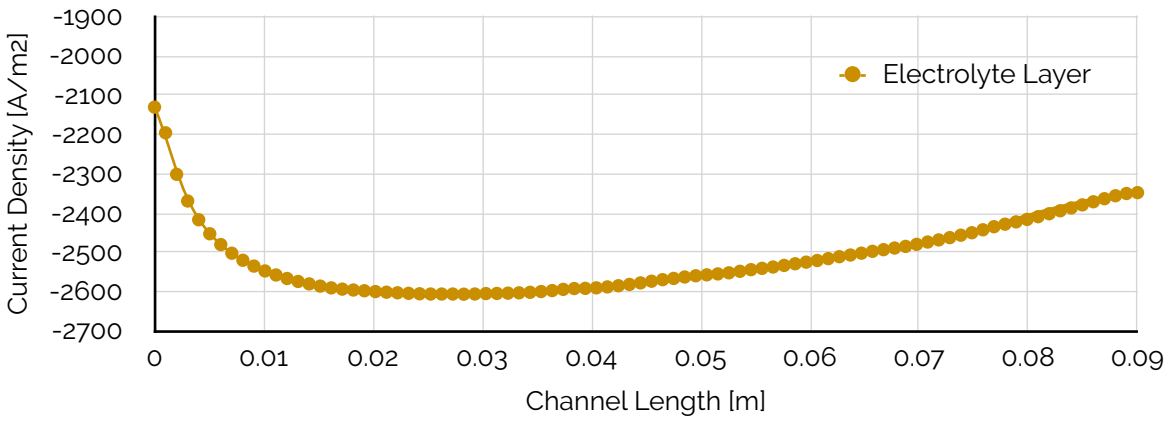

Figure 6.9 - Averaged current density through electrolyte layer

SIMULATION OVERVIEW

The simulation was run for 95.000 iterations. The residues decreased steadily without any oscillations. Compared to the other two cases, it took longer for this case to converge. The model in case III features several complex mechanisms, so this was expected. The under-relaxation factors where increased as the simulation progressed towards convergence. This is shown in table 6.5. The final residues from each equation (for each case) are listed in table 6.6 at the end of this chapter.

URF	Iterations 0 - 2.000	Iterations 2.000 - 10.000	Iterations 10.000 - 95.000
Pressure	0.3	0.3	0.3
Density	0.5	0.5	0.5
Body Forces	0.5	0.5	0.8
Momentum	0.5	0.5	0.6
Species	0.5	0.9	0.999
Energy	0.7	0.9	0.999
Electric Potential	0.25	0.5	0.9
Protonic Potential	0.25	0.5	0.9

Table 6.5 - Evolution of under-relaxation factors throughout the simulation

6.4 - Discussion

The results for each case are reflected on in this section. For a modelling study the main question should always be, to what extend are the results meaningful and accurate? This is discussed below.

CASE I AND II

The results of the first case show very similar results as the studies this model was based on.
Both in terms of reaction rate and surface coverage, the models agree with each other. The only obvious deviation here is the surface coverage fraction of H*. In no other studies where these relatively high values observed. Since this model was run for the least amount of time, this might be because the surface species needed more iterations to converge.
The endothermic nature of the process is also verified and shown in figure 6.2, this is something which was omitted in other studies. The temperature drop is substantial, 322 degrees. The channel is considered perfectly insulated and the mass flow is relatively high, so all 206 kJ/mol must be subtracted from the fuel feed.
The exothermic nature of the fuel cell processes (both chemical reaction and Joule heating) would counter this cooling effect, so it is not expected that such large temperature gradients occur inside a SOFC in operation. Note that this temperature also changes the density (and subsequently the flow velocity) of the mixture. Incompressible ideal gas is used in these cases which means the gasses cannot be compressed by pressure acting upon the fluid, but temperature variations will change the density of the mixture.

The second case expands on the promising results from the first. The species CH_4 and H_2O are mixed in a 1:2 ratio and reach chemical equilibrium precisely as predicted by Gibbs Energy minimisation in Chapter 3. The overall reaction rate can be determined using these result as well. This is an unknown when the Gibbs Energy minimisation method is used. The second case shows that equilibrium is reached, with the resident time and mass flow used in this simulation.
The simulation was also performed using a 1:1 mixture, and in this case the mixture also reached the predicted chemical equilibrium values. These results have been omitted because they provided no other insights than this.

The methane concentration decreases along the channel with a constant halving time. This means the reaction is close to a first order reaction with respect to the partial pressure of methane. This is an assumption made in many other studies as well. Other sources provide slightly other reaction orders, but these are always close to a first order form.

The activation energy for the reaction can be determined as well. This is an important value to model reaction kinetics in a simpler way, so it is important that these values are accurately reported. The calculated activation energy lies close to the results reported in other works. These values vary still quite a bit, from 74 to 124 kJ/mol. This is because the final value also depends on the reaction order assumed, along with the other inaccuracies that may reside in the model.

CASE III

The mass balance in the simulation is preserved. This is an important point, because the coupling of the reforming mechanism where hydrogen is produced and the electrochemistry where hydrogen is consumed can be verified by this observation.
Figure 6.7a shows how the (1:2) ratio between CH_4 and H_2O quickly changes as the reforming mechanism starts to produce CO, CO_2 and H_2. Oxygen ions are added to the mixture as well, so that no CO is present in the channel. The mole fraction starts to rise again as hydrogen and oxygen ions start to produce electricity.

The shapes of the hydrogen mole fraction in figure 6.7a and the current density in figure 6.8 are clearly similar. It would seem that local current density depends on the available hydrogen concentration.
Another observation from figure 6.8 is that the current density may fluctuate in the order of 20%. This might result in thermal stresses in larger stacks, where many channels such as these are combined.

The anode voltage has been kept at a constant 0.7 V, the average resulting current density was 0.25 A/cm^2. The power density in this simulated IR channel is thus 0.175 W/cm^2. This value lies well within the ranges of power densities reported in many other studies at similar temperature (Lipman, 2019).
The voltage used is considered to lie in an excellent operating window, and is therefore used in many other works as well (van Biert, 2020). A complete I-V curve could be constructed by running the model on other voltages. This proved to be too time consuming, and is therefore not part of this thesis.

The gas composition that is formed by the reforming mechanism seem to be accurate. It is therefore likely that the species distribution on the active surface is also realistic.
Two carbon containing sources are present on the active surface; carbon monoxide and methane derivatives including pure carbon.

Carbon monoxide is present in a large fraction, see table 6.1. This could be a lurking cause for carbon deposition when an oxygen ion deficiency occurs. Studies (Offer et al., 2009) have already highlighted the relation between current density (and thus oxygen ion flux) and carbon deposition.
When enough oxygen ions are available at the anode surface, reaction 6.5 can occur. When this is not the case, the large fraction of lingering CO on the surface might sustain the hydrogen conversion so that only solid carbon remains on those sites. This is illustrated in figure 6.10.

$$C_xH_y + y\,O^{2-} \leftrightarrow \frac{y}{2}\,H_2O + xCO_2 + 2y\,e^- \qquad [6.5]$$

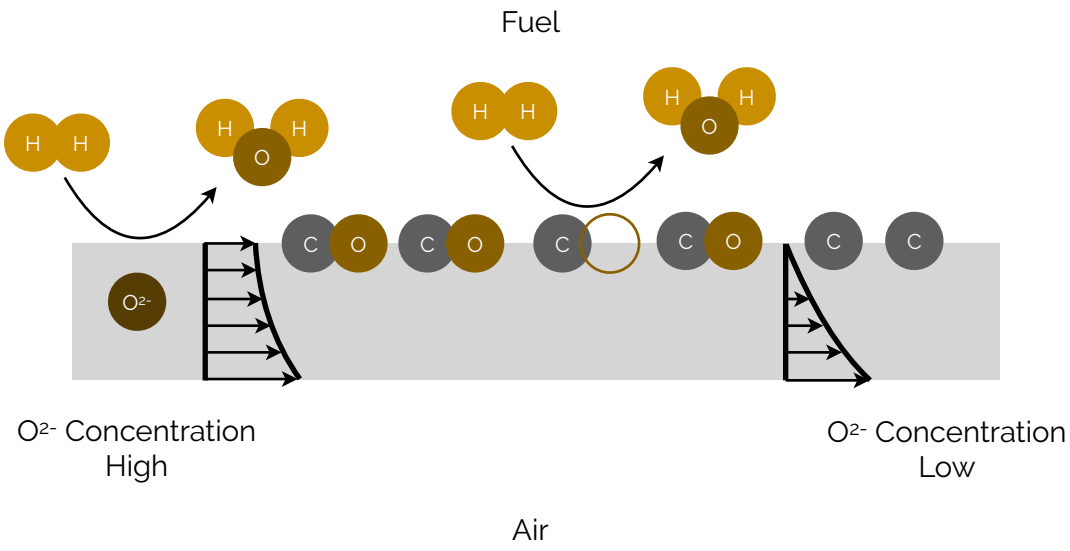

Figure 6.10 - Possible cause for carbon formation at low current density

Figure 6.5 shows al carbon containing derivates from methane to pure carbon. According to the results of this model, these species are only present in trace amounts. It seems unlikely that devastating carbon formation could form from such minute concentrations.
A transient version of this model might show if this concentration grows linearly until more complex carbon structures are formed. This could be done if the current reaction mechanism is extended with additional carbon-carbon and carbon-nickel reactions. A comprehensive DFT study must precede this as well.

6.5 - Residuals

The table in this section lists all residuals of the three cases discussed in this chapter. The size of the largest residual is often a good indicator if convergence has been achieved. Ideally, no residuals larger than $1 \cdot 10^{-6}$ (excellent convergence) should be present when the solver is suspended. Case III passes this criterium easily. For case I and case II, some residuals were still slightly larger. All values are still well above $1 \cdot 10^{-3}$ (good convergence), this is the minimum requirement CFD studies are typically compared with.

Equation	Case I	Case II	Case III
Continuity	$3.7879 \cdot 10^{-4}$	$1.8414 \cdot 10^{-5}$	$1.3083 \cdot 10^{-7}$
X-velocity	$2.1652 \cdot 10^{-8}$	$1.7344 \cdot 10^{-7}$	$5.9980 \cdot 10^{-8}$
Y-velocity	$9.5275 \cdot 10^{-8}$	$7.3475 \cdot 10^{-8}$	$9.2112 \cdot 10^{-8}$
Z-velocity	$1.1672 \cdot 10^{-4}$	$6.3588 \cdot 10^{-5}$	$9.8151 \cdot 10^{-8}$
Energy	$5.1602 \cdot 10^{-7}$	$2.2705 \cdot 10^{-7}$	$3.4991 \cdot 10^{-10}$
O2	$2.1163 \cdot 10^{-8}$	$4.1554 \cdot 10^{-5}$	$4.4233 \cdot 10^{-11}$
H2O	$1.6474 \cdot 10^{-7}$	$3.5968 \cdot 10^{-7}$	$4.4619 \cdot 10^{-10}$
CO	$1.7378 \cdot 10^{-6}$	$7.6469 \cdot 10^{-7}$	$2.1947 \cdot 10^{-7}$
CO2	$1.1533 \cdot 10^{-6}$	$4.5995 \cdot 10^{-7}$	$1.9380 \cdot 10^{-9}$
CH4	$7.5698 \cdot 10^{-7}$	$6.0234 \cdot 10^{-7}$	$3.0097 \cdot 10^{-9}$
H2	$6.1843 \cdot 10^{-7}$	$2.4847 \cdot 10^{-7}$	$2.8587 \cdot 10^{-9}$
Ar	$1.3569 \cdot 10^{-6}$	-	-
N2	-	-	$4.6359 \cdot 10^{-11}$
UDF-1	-	-	$5.0795 \cdot 10^{-10}$
UDF-2	-	-	$1.4065 \cdot 10^{-7}$

Table 6.6 - Residuals per equation at the end of each simulation

7 - Conclusions and Recommendations

CONCLUSIONS

The goal of the modelling part of this thesis is to find the critical areas inside the fuel channel that are most vulnerable to carbon deposition.
The chemical equilibrium conditions at varying temperatures where used to confirm that the surface mechanism functions in accordance with thermodynamics.
The temperature distribution shown in figure 6.2, and the estimation of activation energy in table 6.3 affirm this as well.

It is possible to combine complex surface mechanisms with the fuel cell module in Fluent. Because of this, the reaction kinetics of combined methane reforming and fuel cell electrochemistry can be obtained. The model used here provides two significant insights into the inner workings of a real three dimensional channel.

- Local mixture composition as the methane is reformed and the produced hydrogen is simultaneously consumed as fuel by the fuel cell.
- Surface site coverage, and more importantly, which species remain present on the surface during operation.

These results are a useful starting points to identify critical areas, vulnerable to irreversible carbon formations. Furthermore, it is difficult to obtain these results by conducting experiments since it is impossible to measure these conditions inside such small channels.

The first one-third of the channel is most likely the primary place where detrimental carbon deposition occurs first. Figure 6.6b shows how roughly 82% of all methane fed to the channel has been reformed within that segment at 1073 K.
Lower temperatures slows methane reforming down, as can be seen in figure 6.7. However, this is not the way to mitigate carbon deposition, as lower temperatures allow for encapsulating carbon formations to form. The key to mitigate carbon formation lies in slowing the methane reforming reaction down, whilst the temperature of the anode surface remains above 1073K, some options are discussed in the recommendation section.

Experiments have shown that a deficit in oxygen ions on the anode side of the electrolyte directly causes carbon formation. According to the results, on the active surface, a significant fraction (0.15 - 0.25) consists of carbon monoxide. Figure 6.10 shows how a limiting supply of oxygen ions could rapidly lead to an increase in pure carbon on the anode surface.

The model is not capable of modelling transient carbon formations that ultimately inhibit the fuel cells operation, so no strong conclusions based on the models should be drawn. However, the model already evaluates relevant parameters that are needed to model carbon deposition further, namely:

- Temperature variations due to methane reforming and hydrogen consumption
- Locally varying current densities

By extending the reaction mechanism with surface reactions that lead to permanent carbon structures, more solid conclusions can be made.

RECOMMENDATIONS FOR MODEL IMPROVEMENT

Case III can be a great basis for more advanced research to prevent carbon deposition in SOFCs. However, the model must be improved in two areas before one can proceed with other modifications and additions listed in the sections hereafter.

1. Several additional surface reactions must be added to model unsteady carbon formation. This is can be done with additional DFT calculations involving carbon, YSZ and differentiated nickel sites (radical sites along the TPB and regular sites). If these DFT calculations are successful and the reactions are incorporated in the surface mechanism, a distinction between reversible and irreversible carbon-nickel and carbon-YSZ bonds can be made.
2. The porous media can be developed further. They are currently defined by three global parameters found in literature. It is known that mass transfer in the porous media can become a current limiting factor. If this is not accurately modelled, the model will surpass realistic operation, current densities and efficiencies.

OPERATIONAL STRATEGY IMPROVEMENTS

When the extended surface mechanism is developed, operating windows where no irreversible carbon formations occur can be searched for. Two possible ways to achieve this are listed here.

1. The first approach may be to find general operating conditions that prevent carbon deposition. Findings in chapter 3 can help eliminate suggestions found in literature (such as the addition of sulfur to the fuel stream), and provide certain ranges for temperature and S/C ratios that seem promising.
2. Another promising approach is to fluctuate the inlet gas composition with added steam. When the steam is added, surface carbon is washed off before they can form non-removable formations. The current model can be used in pseudo-transient and transient schemes as well. These schemes allow for fluctuating boundary conditions.

RECOMMENDED DESIGN IMPROVEMENTS

The current state of a (solid oxide) fuel cell is still a somewhat basic device. The channel dimensions, materials and operating conditions are typically the same throughout the entire system. This is very reminiscent of the early days of internal combustion engines. Over a hundred years of development have seen great improvements in efficiency, durability and power output. These developments came with more complex designs, tackling local bottlenecks within the system. A same approach can be taken to further the advancements in fuel cell technology. Two possible ways to mitigate carbon formation in this way are listed here.

1. Sophisticated geometric design of the individual flow channels, and interwoven collection of flow channels can change local residence time. The goal of this study is to precisely control the local methane density and concentration, so that no carbon formations can form.
2. This can also be achieved by varying the material properties. The reforming of methane is completed for 90% within the first centimetres of a channel. Consequently, most methane reforming occurs here as well. Treating this part of the catalyst differently, by locally heating the material, using different materials or even electrically isolating this part of the catalyst may lead to new insights in eliminating carbon formations on the anode.

Note that these designs may become quite exotic, keep scalability and manufacturability in mind.

Appendix A1 - MATLAB-code for finding chemical equilibrium

```
%% Preparation
clc
close all

global Gjo_i R T_i
R = 8.314;                                          % [J/mol/K]
T = [600 700 800 900 1000 1100 1200 1300];          % [K]
p0 = 1;                                             % [bar]
p1 = 2;                                             % [bar]
Gjo = [-25.01   -396.7  -165.8  0   -214.2  0;
       -16.41   -398.1  -175.8  0   -209.1  0;
       -8.002   -399.8  -186.1  0   -203.9  0;
       0.132    -401.8  -196.5  0   -198.1  0;
       7.932    -404.2  -207.1  0   -193.2  0;
       15.35    -406.8  -217.9  0   -187.9  0;
       22.34    -409.7  -228.7  0   -182.4  0;
       28.89    -413.0  -239.7  0   -177.0  0];     % [kJ/mol]
Gjo = Gjo*1000;                                     % [J/mol]

species = {'CH4', 'CO2', 'CO', 'H2', 'H20', 'O2'};

% The results vector is used to store the mixture compositions.
results = zeros(length(species), length(T), 10);

distance = [0 1 2 3 4 5 6 7 8 9];                   % [mm]

for xx = 1:10
    %% Preprocessing

    % Concentration of elements in channel
    % Inlet flow
    n_H2O = 66;                                     % [mol]
    n_CH4 = 34;                                     % [mol]

    % Oxygen flow through electrolyte
    n_O = 8;                                        % [mol/mm]


    % The elements C, H, O, and their moleculair weight are
    % stored in the element cell array and mw vector. The
    % moleculair weight of H20 is used as a constant later on.

    element = {'C', 'H', 'O'};
    M = [12.01 1.008 16.00]';                       % [g/mol]

    % The OHCN vector will store the amount of O, H, and C in
    % the starting mixture.

    OHC = zeros(1, length(element));

    OHC(1) = n_O*(xx - 1) + n_H2O*(1);
    OHC(2) = n_H2O*(2) + n_CH4*(4);
    OHC(3) = n_CH4*(1);


    %% Setup
    % R is the universal gas constant.
    % The 2D Gjo matrix lists all the Gibbs Free energies of
    % formation for each species we expect to find on the right
    % side of the equation for temperatures from 600K up to
    % 1300K. These species are listed in the species cell
    % array. The types of biomass are listed in the biomass
    % cell array. The matrix Gjo is composed like this:
    %        Gf(CH4) Gf(CO2) ...
    % T=600 |       |       |
    % T=700 |       |       |
    %  ...  |       |       |
    %
    % The global variables Gjo_i, T_i (and R) are used in the
    % calculations below, where we pick a value from the T
    % array and Gjo matrix and find the mixture composition of
    % those specific values.

    Gjo_i = [];


    %% Linear equality constraints for atomic mass
    %% conservation
    % The Aeq matrix is used in the fmincon solver, together
    % with a vertical entry from the OHC matrix as Beq in
    % Aeq•x = Beq. The Aeq matrix lists the species on the
    % right side of the equation; CH4, CO2, H2 and H20. Just
    % like the OHC matrix, the first row are the number of O
    % atoms, and the second and third row show the number of H
    % and C atoms respectively. This matrix ensures that x1,
    % x2, x3 and x4 take into account the available species.

    Aeq =   [0 2 1 0 1 2        %O
             4 0 0 2 2 0        %H
             1 1 1 0 0 0];      %C

    %% Limits on mole number
    % In order to get valid results, we must set the lower
    % bound for each entry in the x vector to 0. Negative
    % values are not allowed.

    lb = zeros(1, length(species));

    %% Initial guess for the solver
    % The initial guess is just set to one. In order to make
    % sure that the global minimum is reached, we can set
    % another initial guess here. X0 = 0 is not allowed,
    % because that collides with our lower bound.

    X0 = [0.2 0.2 0.2 0.2 0.1 1e-21];

    %% Setup of minimisation
    % For the solver we chose the sqp (Sequential Quadratic
    % Programming) algorithm. This utilises an approximation of
    % the Lagrangian function, which is the exact solution to
    % the unbound set of (non)linear equations that our problem
    % consists of.

    options = optimset('Algorithm', 'sqp');

    % The solver is called for every iteration of temperature,
    % using the OHC(:) couple for Beq, Aeq, X0 and lb discussed
    % above.

    Beq = OHC;

    for i = 1:length(T)
        Gjo_i = Gjo(i,:) + R*T(i)*log(p1/p0);
        T_i = T(i);
        [x, fval] = fmincon(@gibbsEnergy, X0, [], [], Aeq, Beq,
        lb, [], [], options);

        x_t = sum(x);
        for z = 1:length(x)
            x(z) = (x(z)/x_t);
        end

        for j=1:numel(x)
            results(j, i, xx) = x(j);
        end
    end
end


%% Plot results
figure(1)
set(0,'DefaultAxesColorOrder',copper(length(species)))
% set(gca, 'YScale', 'log')
hold on
for i = 1:size(results,1)
        plot(T, results(i,:,1), 'LineWidth', 2)
end

legend(species)
title('Equilibrium composition at several temperatures')
xlabel('Temperature [K]')
ylabel('Composition [%]')
hold off

% Plot results from 1200 K (7th entry in y-direction)

channel_comp = zeros(length(species), length(distance));
for i = 1:length(species)
    for j = 1:length(distance)
        channel_comp(i,j) = results(i,7,j);
    end
end


figure(2)
hold on
for i = 1:size(results,1)
    plot(distance, channel_comp(i,:), 'LineWidth', 2)
end
legend(species)
title('Equilibrium composition at several temperatures')
xlabel('Distance [cm]')
ylabel('Composition [%]')
hold off

%% Gibbs free energy of a mixture
function G = gibbsEnergy(xi)
    global Gjo_i R T_i
    Exi = sum(xi);
    G = sum(xi.*(Gjo_i/R/T_i + log(xi/Exi)));
end
```

Appendix A2 - Reaction mechanism for methane reforming

n	Reaction	A ($cm^2/mol/s$)	B (-)	E (kJ/mol)	n	Reaction	A ($cm^2/mol/s$)	B (-)	E (kJ/mol)
1	$H_2 + \square_{Ni} \rightarrow 2\ H_{Ni}$	$3.62 \cdot 10^{14}$	0.5	0	22	$CH_{3,Ni} + H_{Ni} \rightarrow CH_{4,Ni} + \square_{Ni}$	$6.03 \cdot 10^{20}$	0	61.58
2	$2\ H_{Ni} \rightarrow H_2 + \square_{Ni}$	$2.55 \cdot 10^{18}$	0	81.21	23	$CH_{3,Ni} + \square_{Ni} \rightarrow CH_{2,Ni} + H_{Ni}$	$3.70 \cdot 10^{23}$	0	100.0
3	$H_2O + \square_{Ni} \rightarrow H_2O + \square_{Ni}$	$3.22 \cdot 10^{07}$	0.5	0	24	$CH_{2,Ni} + H_{Ni} \rightarrow CH_{3,Ni} + \square_{Ni}$	$1.29 \cdot 10^{22}$	0	55.33
4	$H_2O_{Ni} \rightarrow H_2O + \square_{Ni}$	$3.73 \cdot 10^{12}$	0	60.96	25	$CH_{2,Ni} + \square_{Ni} \rightarrow CH_{Ni} + H_{Ni}$	$3.70 \cdot 10^{23}$	0	97.10
5	$H_{Ni} + O_{Ni} \rightarrow OH_{Ni} + \square_{Ni}$	$5.00 \cdot 10^{21}$	0	97.90	26	$CH_{Ni} + H_{Ni} \rightarrow CH_{2,Ni} + \square_{Ni}$	$4.09 \cdot 10^{23}$	0	79.18
6	$OH_{Ni} + \square_{Ni} \rightarrow H_{Ni} + O_{Ni}$	$1.78 \cdot 10^{21}$	0	36.09	27	$CH_{Ni} + \square_{Ni} \rightarrow C_{Ni} + H_{Ni}$	$3.70 \cdot 10^{20}$	0	18.80
7	$H_{Ni} + OH_{Ni} \rightarrow H_2O_{Ni} + \square_{Ni}$	$3.00 \cdot 10^{19}$	0	42.70	28	$C_{Ni} + H_{Ni} \rightarrow CH_{Ni} + \square_{Ni}$	$4.56 \cdot 10^{21}$	0	161.2
8	$H_2O_{Ni} + \square_{Ni} \rightarrow H_{Ni} + OH_{Ni}$	$2.27 \cdot 10^{20}$	0	91.76	29	$CH_{4,Ni} + O_{Ni} \rightarrow CH_{3,Ni} + OH_{Ni}$	$1.70 \cdot 10^{23}$	0	88.30
9	$H_2O_{Ni} + O_{Ni} \rightarrow OH_{Ni} + OH_{Ni}$	$6.37 \cdot 10^{22}$	0	210.9	30	$CH_{3,Ni} + OH_{Ni} \rightarrow CH_{4,Ni} + O_{Ni}$	$9.87 \cdot 10^{21}$	0	30.37
10	$OH_{Ni} + OH_{Ni} \rightarrow H_2O_{Ni} + O_{Ni}$	$3.00 \cdot 10^{20}$	0	100.0	31	$CH_{3,Ni} + O_{Ni} \rightarrow CH_{2,Ni} + OH_{Ni}$	$3.70 \cdot 10^{23}$	0	130.1
11	$CO + \square_{Ni} \rightarrow CO_{Ni}$	$1.29 \cdot 10^{08}$	0.5	0	32	$CH_{2,Ni} + OH_{Ni} \rightarrow CH_{3,Ni} + O_{Ni}$	$4.61 \cdot 10^{20}$	0	23.62
12	$CO_{Ni} \rightarrow CO + \square_{Ni}$	$3.56 \cdot 10^{11}$	0	91.13	33	$CH_{2,Ni} + O_{Ni} \rightarrow CH_{Ni} + OH_{Ni}$	$3.70 \cdot 10^{23}$	0	126.8
13	$CO_2 + \square_{Ni} \rightarrow CO_{2,Ni}$	$2.06 \cdot 10^{03}$	0	0	34	$CH_{Ni} + OH_{Ni} \rightarrow CH_{2,Ni} + O_{Ni}$	$1.46 \cdot 10^{22}$	0	47.07
14	$CO_{2,Ni} \rightarrow CO_2 + \square_{Ni}$	$6.44 \cdot 10^{07}$	0	25.98	35	$CH_{Ni} + O_{Ni} \rightarrow C_{Ni} + OH_{Ni}$	$3.70 \cdot 10^{20}$	0	48.10
15	$CO_{Ni} + O_{Ni} \rightarrow CO_{2,Ni} + \square_{Ni}$	$2.00 \cdot 10^{18}$	0	123.6	36	$C_{Ni} + OH_{Ni} \rightarrow CH_{2,Ni} + O_{Ni}$	$1.63 \cdot 10^{20}$	0	128.6
16	$CO_{2,Ni} + \square_{Ni} \rightarrow CO_{Ni} + O_{Ni}$	$4.65 \cdot 10^{22}$	-1	89.32	37	$C_{Ni} + O_{Ni} \rightarrow CO_{Ni} + \square_{Ni}$	$5.20 \cdot 10^{22}$	0	148.1
17	$O_2 + 2\ \square_{Ni} \rightarrow 2\ O_{Ni}$	$9.09 \cdot 10^{13}$	0.5	0	38	$CO_{Ni} + \square_{Ni} \rightarrow C_{Ni} + O_{Ni}$	$1.35 \cdot 10^{21}$	-3	116.1
18	$2\ O_{Ni} \rightarrow O_2 + 2\ \square_{Ni}$	$4.28 \cdot 10^{22}$	0	474.9	39	$H_{Ni} + CO_{Ni} \rightarrow HCO_{Ni} + \square_{Ni}$	$4.02 \cdot 10^{19}$	-1	132.2
19	$CH_4 + \square_{Ni} \rightarrow CH_{4,Ni}$	$2.73 \cdot 10^{06}$	0.5	0	40	$HCO_{Ni} + \square_{Ni} \rightarrow H_{Ni} + CO_{Ni}$	$3.70 \cdot 10^{20}$	0	0
20	$CH_{4,Ni} \rightarrow CH_4 + \square_{Ni}$	$8.70 \cdot 10^{15}$	0	37.55	41	$HCO_{Ni} + \square_{Ni} \rightarrow CH_{Ni} + O_{Ni}$	$3.70 \cdot 10^{23}$	-3	95.80
21	$CH_{4,Ni} + \square_{Ni} \rightarrow CH_{3,Ni} + H_{Ni}$	$3.70 \cdot 10^{20}$	0	57.70	42	$CH_{Ni} + O_{Ni} \rightarrow HCO_{Ni} + \square_{Ni}$	$4.60 \cdot 10^{19}$	0	109.9

Appendix A3 - Model development using ANSYS Workbench

This model has been developed entirely in the ANSYS Workbench suite (version 19.1). The geometry was created in SpaceClaim. The meshing, blocking and boundary conditions were subsequently created in CFD. The unstructured mesh was finally imported to ANSYS Fluent, were the model was set up further and the solution was calculated.
In order to reproduce the results, or add to this type of model, important details on how this model was created can be found in this section.
Crucial aspects in design and modelling philosophy used in each program are justified as well.
Furthermore, background information is provided to how exactly convergence was reached. Major problems resulting in program crashes, freezes or divergent solver behaviour encountered during the development of the model are described here as well. Useful ways of overcoming these difficulties are provided as well, as the Fluent User Manual falls short on this area in some cases.

A3.1 - SpaceClaim

SpaceClaim is the relatively new CAD-program directly accessible from the ANSYS Workbench. Some interesting design features of the geometry are explained in this section.

LIMITS TO GEOMETRY DIMENSIONS

On of the limitations of SpaceClaim is the resolution of dimensions. Values smaller than 0.1 mm are not allowed. This is problematic since the cathode catalytic layer for example is just 0.025 mm thick. A workaround is to create the geometry on a different scale. The geometry in SpaceClaim was created on a larger scale, by factor 100 in the x- and y-direction, and by factor 10 in the z-direction. Only after the mesh has been imported into Fluent, it is scaled to the final correct dimensions. See figure A3.1 and table A3.1 for an overview.

	Name	Length (mm)		Name	Length (mm)
a	Anode Current Collector	$1{,}2 \cdot 10^{0}$	f	Cathode Support	$1{,}3 \cdot 10^{-2}$
b	Anode Support	$2{,}0 \cdot 10^{-2}$	g	Cathode Current Collector	$1{,}2 \cdot 10^{0}$
c	Anode Catalyst	$4{,}0 \cdot 10^{-1}$	h	Global Width	$2{,}0 \cdot 10^{0}$
d	Electrolyte	$8{,}0 \cdot 10^{-3}$	i	Channel Width	$1{,}0 \cdot 10^{0}$
e	Cathode Catalyst	$2{,}5 \cdot 10^{-2}$	j	Channel Height	$1{,}0 \cdot 10^{0}$

Table A3.1 - Dimensions of final geometry, scaled down in Fluent

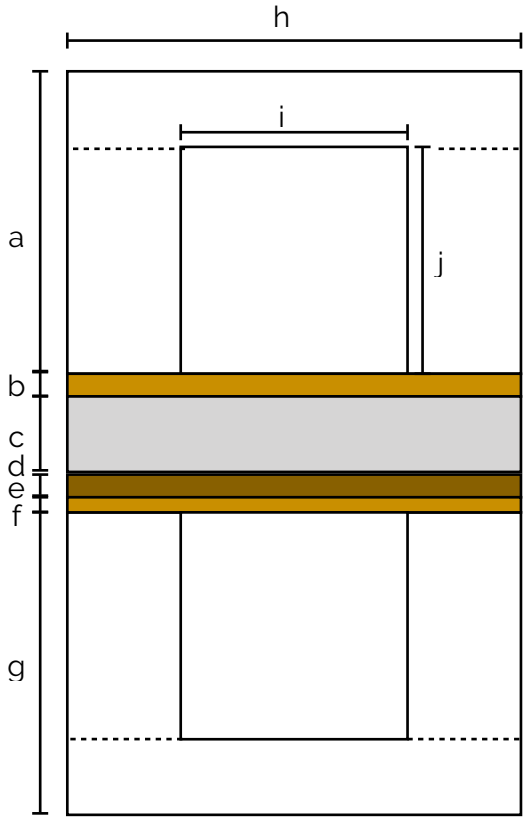

Figure A3.1 - SpaceClaim Geometry (x-y plane)

KEEPING AND DELETING INTERNAL SURFACES

When the geometry shown in figure 6.1 is created by drawing and extruding several rectangles, special care must be taken with removing and keeping internal surfaces. The dashed lines in figure A3.1 represent surfaces that were deleted. Not deleting those surfaces at this stage of model development could result in unnatural flow features and unneeded increased complexity. Surfaces should be deleted when both sides lie in the same domain.

When internal surfaces form the boundary of two physically different domains, like the anode support layer and the anode catalytic layer, they must be kept. In this case, these surfaces must be designated with an 'interior' boundary condition.

Surfaces that remain must either be merged to one single surface so that one edge and surface will remain. Alternatively, the surfaces must be set to share their topology. This means that the surfaces will automatically share the nodes of the mesh, as it will be impossible to select each unique edge later on.

A3.2 - ICEM CFD

The next step is to define the cell zones, mesh parameters and boundary conditions in ICEM CFD. This program was selected as it was unclear at this point which CFD program would be used. By using ICEM CFD, the mesh could be exported in different formats compatible with other CFD programs than Fluent.

ICEM CFD is a complex program where several workflows can result in basically the same file. During the development of this mesh file several problems were encountered. The workflow described below has resulted from consulting with the ICEM CFD User Manual and several

internet forums. For the creation of meshes with relatively simple geometry, but with multiple inlets, outlets, and several types of cell zones and other boundary conditions this workflow could be regarded as best practices.

BLOCKING AND CELL ZONES

After the standard procedure of naming and grouping all the surfaces, edges and points on block must be created encompassing the entire domain.
This block is then spliced into 13 sub-blocks shown in figure A3.2. The names of the zones are listed in table A3.2. These blocks are subsequently added to a body, which is interpreted by Fluent as a cell zone. These cell zones are used to define and model the various physical features of the fuel cell. The names and types of the bodies are shown in figure A3.2 as well.
The mesh size parameters can be defined next. The single surfaces or shared topology will help make sure the mesh is smooth at each domain border. Further details on mesh size are provided in chapter 5, section 5.5.

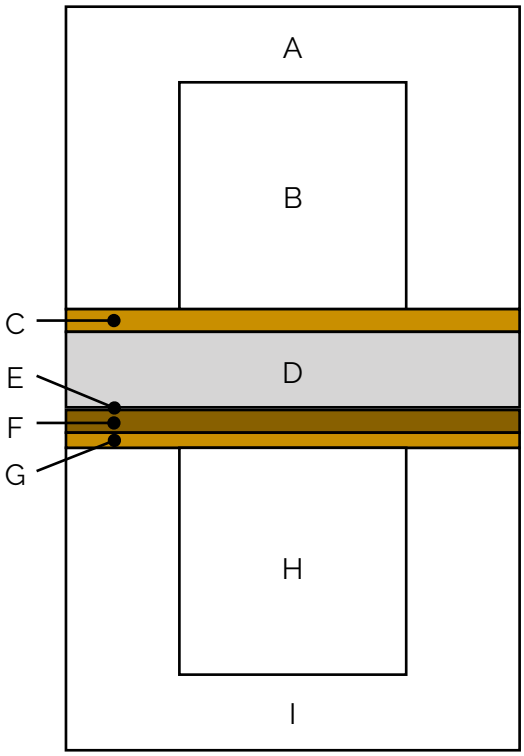

Figure A3.2 - Overview all blocks and cell zones (x-y plane)

Block	Cell zone name	Type	Block	Cell zone name	Type
A	Anode Current Collector	Solid	F	Cathode Catalyst	Fluid
B	Fuel Channel	Fluid	G	Cathode Support	Fluid
C	Anode Support	Fluid	H	Air Channel	Fluid
D	Anode Catalyst	Fluid	I	Cathode Current Collector	Solid
E	Electrolyte	Fluid			

Table A3.2 - Overview of fluid and solid domains

BOUNDARY CONDITIONS

The last step in ICEM CFD is to select the output solver and define boundary conditions.
Table A3.3 provides a short overview of all types of boundary conditions applied. The mass-flow inlet was chosen over a simple velocity inlet to make sure the mass balance equation in Fluent converges.
The pressure-vent outlet was chosen over a more simple 'outflow' boundary condition so that outlet conditions could be defined in Fluent. This is useful because during the first approximate thousand iterations, reversing flows at the outlet can occur even though an 'outflow' boundary condition is selected.

Boundary Name	Type	Boundary Name	Type
Fuel inlet	Mass flow inlet	Domain border	Wall
Air inlet	Mass flow inlet	Channel wall	Wall
Fuel outlet	Pressure outlet	Solid-liquid contacts	Wall
Air outlet	Pressure outlet	Liquid-liquid contacts	Interior

Table A3.3 - List of boundary conditions

A3.3 - Fluent

This section goes further into how the model was further developed in Fluent. It turns out that the order in which to add complexity and many other aspects are of crucial importance for obtaining a working model. These steps and accompanying program settings are explained first. This section concludes with some explanations and solutions for problems that are often encountered whilst working through a more complex case in Fluent. This section might be very helpful in order to reproduce this model.

STEP 1 - CONFIGURE FUEL CELL MODULE

The first step consists of importing and configuring the fuel cell module provided by ANSYS. The physical parameters such as porosities of the various catalyst and supporting layers are all listed in table 5.6 in chapter 5. The ANSYS User Manual provides a recommended order of defining cell zones and setting specific boundary conditions essential for a functioning module.
It is recommended to make sure the basic module works before continuing to the next step. It will be more cumbersome to debug the model when additional complexities are added.
The model at this stage has four modes of failure, the first of which is when the model completely crashes the program. This is most often caused by some erroneous setting with either the cell zone conditions, boundary conditions, boundaries between the separate cell zones, or finally one of the UDF-settings.
Secondly, the model can diverge after the first iteration. This is usually results in a floating point error. This can be caused by a too great a difference between the open circuit voltage and target cell voltage. A more subtle error is when the pressure and mass flow equations become decoupled. This results in Fluent quietly abandoning the mass conversation equation. How this can be detected and solved is discussed in the next section, along with all other error messages and fixes.

The final mode of failure is when some relaxation factors are set too low, so that convergence is never reached. The standard equation utilising a relaxation factor is shown in equation A3.1, where ϕ is a general variable and α is the accompanying relaxation factor.

$$\phi = \phi_{old} + \alpha \Delta\phi \qquad [A3.1]$$

This type of relaxation factor can be found in every book about computational fluid dynamics, and is used by Fluent as well. When this formula is used, the convergence rate varies linearly, and the problem described above will not occur.
Using a pressure-based solver with Fluent however, equation A3.2 will be used.

$$\frac{a_p \phi}{\alpha} = \sum_{nb} a_{nb} \phi_{nb} + b + \frac{1 - \alpha}{\alpha} \cdot a_p \cdot \phi_{old} \qquad [A3.2]$$

For this case, the relaxation factor is first applied to the old value non-linearly. This is added to the source term and similar terms from the neighbouring cells. Due to the implicit coupling of the flow equations, equation A3.2 is combined by Fluent in a way that is not documented in the user manual. The result is a strong non-linear relation between relaxation factor and the time to reach convergence. The relaxation factors used at each step are listed in table A3.4.

Relaxation Factor	Step 1	Step 2	Step 3	Relaxation Factor			
Pressure	0.70	0.8	0.8	Species	0.99	0.75	0.999
Density	1	0.8	0.8	Electric potential	1	-	0.9
Momentum	0.60	1	0.9	Protonic potential	1	-	0.9

Table A3.4 - Overview of relaxation factors used in each step

STEP 2 - EDIT MIXTURE AND ADD REACTIONS

Fluent has a way to import CHEMKIN files automatically. A new mixture is created and all specified physical constants are added to the mixture species. Furthermore, all gas and surface reactions are added as well.
This feature doesn't work together with the fuel cell module. It is not possible to combine both mixtures, and any attempt will result in program crashes. The only solution is to add the missing gas and site species manually to the fuel cell mixture created by the fuel cell module. Afterwards, the reactions can be added as well.
The CHEMKIN mechanisms can be imported in another case, in order to copy the individual values and parameters to the mixture that is created by the fuel cell module ("fc-mixture"). The mechanism text files, updated for compatibility for Fluent 19.x are added in Appendix A4.
It is recommended to verify the model keeps working during this stage. Net reaction rates of the surface reactions can be monitored to make sure they are working correctly.
Before continuing to the next step, it is useful to run the model with the surface mechanism enabled and the fuel cell module disabled until it is converged. This is in essence merely a methane reformer. Since this reaction has a relatively high overall rate, the species initial conditions for chemical equilibrium can be used inside the fuel channel. This will improve convergence rate dramatically.
The current state of the model can be used as a suitable initial condition, since most flow variables will be close to the final values, apart from the hydrogen and water content.

STEP 3 - RUN COMBINED MODEL

The final step will involve both the surface reactions and the fuel cell module. The initial conditions created by completing the previous step will form the basis for this step.

Trying to run with final boundary conditions will not work. As mentioned in the previous section, a too great a jump in potential difference will cause the solution to diverge. To prevent this, boundary conditions are gradually changed, as well as several physical aspects of the model. Table A3.5 shows in what order various aspects of the model were turned on. The heat of reaction is the first to be activated, which models the temperature drop due to the endothermic nature of methane reforming. The equation prone to diverge is the energy equation, so temporarily reducing the under-relaxation factor to 0.5 might be required.
The electro-chemical sources will enables the flow of electrons, creating the first rough estimation of a reforming fuel cell. This will be the most difficult step to make, as both user defined functions of the fuel cell module are likely to diverge at this point. This can be prevented by patching the values of the current densities (in each direction) to some finite value other than 0. The under-relaxation factors of the energy equation, udf-1 and udf-2 must be reduced temporarily to 0.25.
After this, the final three model features can be turned on sequentially. The order in which this occurs is not very important. It is however recommended to turn on the Buttler-Volmer rate last, since this will significantly slow down the calculation!

Setting	1	2	3	4	5	6	7	8
Cathode voltage	1.05	1.00	0.95	0.90	0.85	0.80	0.75	0.70
Heat of Reaction	✗	✗	✗	✓	✓	✓	✓	✓
Multi-component mixing	✗	✗	✗	✗	✓	✓	✓	✓
Electrochemical Sources	✗	✗	✗	✗	✓	✓	✓	✓
Thermal Diffusion	✗	✗	✗	✗	✗	✓	✓	✓
Joule Heating	✗	✗	✗	✗	✗	✗	✓	✓
Buttler-Volmer Rate	✗	✗	✗	✗	✗	✗	✗	✓

Table A3.5 - Order of changing boundary conditions and enabling options

A3.4 - Error handling

This section lists several issues and proven ways to fix them. Some issues may have multiple fixes that work in some cases, but not always. It is of course impossible to describe every scenario in perfect detail, so use this section as a starting point to work around encountered issues.
The order of the steps in which the model was build described in the previous section were found mainly by trial and error. Some issues can be avoided by following these steps. For example, automatically importing a surface mechanism in combination with the fuel cell module leads to an array of error messages and program crashes for a number of reasons. Firstly, some settings which are not easily accessible are altered. Furthermore, the imported mixture is not automatically added to the already existing mixture used in the fuel cell module. Combining these mixtures without losing several connections with the user-defined functions used in the fuel cell module is a minefield

where one misstep can leave you with two unusable mixtures. These errors can all be avoided by using the manual method described above.
However, some problems will still occur. The most commonly encountered ones and their solutions are listed in this section.

SURFACE MECHANISM

Problem: Importing the mechanism into Fluent doesn't work
Cause: Fluent syntax has changed since the release of the surface mechanism.
Fix: Put the text in Appendix 4 into two separate text files. These are compatible with Fluent 19.x.

Problem: Gaseous compounds are not reacting
Causes: Reactions may not be allowed to take place in the designated area.
Fix: Enable reactions in the relevant cell zone conditions.
Fix: Enable reactions on the relevant surfaces in boundary conditions
Fix: Enable wall surface reactions in the Species model list

Problem: Gaseous compounds are unrealistically slow
Causes: Reactions are allowed to take place, but one or more of these settings might be erroneous.
Fix: Make sure the correct wall is selected. In some cases, Fluent splits the walls in a primary and shadow wall (when the wall divides a solid and fluid cell zone for example). Select the correct side of the wall (but only one side), this might be the shadow side.
Fix: Under-relaxation factor is set too low. In the case of this simulation, the URF was set to 0.999 before meaningful changes at the outlet were detected.
Fix: Increase the Washcoat Factor for walls in the Boundary Conditions section
Fix: Increase the surface to volume ratio in the Porous Zone section of the Cell Zone Conditions menu.
Fix: Increase the site density in the Reaction Mechanism menu inside the Mixture menu.

ISSUES WITH COMBINING THE FUEL CELL MODULE WITH THE SURFACE MECHANISM

Problem: The model crashes as soon as the fuel cell module is enabled
Causes: Something went wrong during the combining process.The fuel cell module can't find the species that participate in the reactions.
Fix: Delete the faulty mixture, re-initialise the fuel cell module and verify it works with the basic mixture created by the add-on module. When this works, manually add the other species one by one.

GENERAL SOLVING ERRORS

Problem: Fluent crashes when starting the solver.
Cause: While working with complex models with many cell zone types and species transport, program crashes at this moment are often encountered.
Fix: Fluent hasn't got the best verbose error handling. Therefore, this error can have such a wide range of causes, it is impossible to describe a specific fix.
Problem: Fluent will not start iterating.
Cause: Next to an immediate program crash, this is the next most inhibiting situation. Like the previous issue, it can have many causes. The two most common ones are listed here. The system has not enough RAM available, due to a too high cell count. The mesh check feature will not always alert the user when the mesh will be too large as this might depend on model settings as well.
Fix: Reduce the mesh size if possible. Simulation only part of a domain by assuming symmetry in one direction may half the amount of nodes without coarsening the mesh.

Cause: Too many complex features and settings are active. Switching off initially superfluous settings like multi-component mixing, higher order solvers will lead to much quicker iteration time deltas. These settings can be added later, when the solution is already much closer to a physically realistic state.
Fix: Turn off second order model features. The solution will converge to a state closer to physical reality. From there, complex non-linear model features may be turned on again.

Problem: The solution does not converge or residuals diverge/oscillate
Cause: The under-relaxation factor of a specific equation is set too tight. The residual monitor will display strongly oscillation behaviour for one or more equations. The residual monitor is vital tool in Fluent, as it can show in real-time how the solution is behaving. Smooth, gradually decreasing lines for each flow parameter should be observed here. When this is not the case, it is very likely that coupling is lost, and the solution will eventually diverge. Furthermore, it is not recommended to stop the calculation, change some settings en continue from a state where residuals are behaving erratic. More often than not, the solution will not recover, even though correct settings have been selected.
Fix: Reduce the under-relaxation factor of the equation(s) that are displaying unstable behaviour.
Fix: Temporarily disable complex model features that act on the unstable equation.

Problem: Reversed flow at pressure outlets persist
Cause: At the start of a calculation, reversed flow at outlets can sometimes be observed. Initially, this will not lead to problems and the warning prompts can be disregarded. Only when the amount of cell faces where reversed flow is observed are not decreasing steadily, action should be taken as the mass balance equation will no longer be taken into account by the solver.
Fix: Increasing the pressure relaxation factor is often a solution, as the higher pressure at the inlets will cary more weight when the solver determines the direction of flow. The case should be initialised before continuing the solving process, especially when the amount of cell faces where reversed flow occurs exceeds ~200.

Problem: Temperature spikes of 0 and 5000 K
Cause: In the Solution Domain section, the minimum and maximum temperatures considered can be entered. The default range in Fluent is 0 - 5000 K.
Cause: When the Energy equation is being solved, it is usually the last equation that is evaluated. When problems occur with either the Energy equation or other equation(s) such as Momentum and Pressure such as unrealistically high pressures or velocities, the Energy equation must resolve this. For this reason, the temperature of the cells experiencing large gradients or divergent behaviour often drops to 0 or increases to 5000 K.
Fix: Use the Residual Monitor to find which equation(s) might be causing the Energy equation trouble, and use this a starting point for further debugging.

Appendix A4 - CHEMKIN mechanism and thermodynamic data

A4.1 - Thermodynamic Data

```
ELEMENTS
C H O NI AR
END

SPECIES
O2          H2O         CO          CO2         CH4         H2          AR
END

THERMO ALL
   300.0   1000.0   5000.0

CH4             (adjust)  C   1H   4    0    0     300.00   5000.00 1000.00      1
 1.68347883E+00 1.02372356E-02-3.87512864E-06 6.78558487E-10-4.50342312E-14    2
-1.00807871E+04 9.62339497E+00 7.78741479E-01 1.74766835E-02-2.78340904E-05    3
 3.04970804E-08-1.22393068E-11-9.82522852E+03 1.37221947E+01                   4
H2              (adjust)  H   2    0    0    0     300.00   5000.00 1000.00      1
 3.06670950E+00 5.74737550E-04 1.39383190E-08-2.54835180E-11 2.90985740E-15    2
-8.65474120E+02-1.77984240E+00 3.35535140E+00 5.01361440E-04-2.30069080E-07    3
-4.79053240E-10 4.85225850E-13-1.01916260E+03-3.54772280E+00                   4
H2O             (adjust)  H   2O   1    0    0     300.00   5000.00 1000.00      1
 2.61104720E+00 3.15631300E-03-9.29854380E-07 1.33315380E-10-7.46893510E-15    2
-2.98681670E+04 7.20912680E+00 4.16772340E+00-1.81149700E-03 5.94712880E-06    3
-4.86920210E-09 1.52919910E-12-3.02899690E+04-7.31354740E-01                   4
CO              (adjust)  C   1O   1    0    0     300.00   5000.00 1000.00      1
 3.02507806E+00 1.44268852E-03-5.63082779E-07 1.01858133E-10-6.91095156E-15    2
-1.42683496E+04 6.10821772E+00 3.26245165E+00 1.51194085E-03-3.88175522E-06    3
 5.58194424E-09-2.47495123E-12-1.43105391E+04 4.84889698E+00                   4
CO2             (adjust)  C   1O   2    0    0     300.00   5000.00 1000.00      1
 4.45362282E+00 3.14016873E-03-1.27841054E-06 2.39399667E-10-1.66903319E-14    2
-4.89669609E+04-9.55395877E-01 2.27572465E+00 9.92207229E-03-1.04091132E-05    3
 6.86668678E-09-2.11728009E-12-4.83731406E+04 1.01884880E+01                   4
O2              (adjust)  O   2    0    0    0     300.00   5000.00 1000.00      1
 3.61221390E+00 7.48531660E-04-1.98206470E-07 3.37490080E-11-2.39073740E-15    2
-1.19781510E+03 3.67033070E+00 3.78371350E+00-3.02336340E-03 9.94927510E-06    3
-9.81891010E-09 3.30318250E-12-1.06381070E+03 3.64163450E+00                   4
AR              (adjust)  AR  1    0    0    0     300.00   5000.00 1000.00      1
 2.50000000E+00 0.00000000E+00 0.00000000E+00 0.00000000E+00 0.00000000E+00    2
-7.45375020E+02 4.36600060E+00 2.50000000E+00 0.00000000E+00 0.00000000E+00    3
 0.00000000E+00 0.00000000E+00-7.45374980E+02 4.36600060E+00                   4
N2              (adjust)  N   2    0    0    0     300.00   5000.00 1000.00      1
 2.85328990E+00 1.60221280E-03-6.29368930E-07 1.14410220E-10-7.80574650E-15    2
-8.90080930E+02 6.39648970E+00 3.70441770E+00-1.42187530E-03 2.86703920E-06    3
-1.20288850E-09-1.39546770E-14-1.06407950E+03 2.23362850E+00                   4
NI(s)           (adjust)  NI  1    0    0    0     300.00   3000.00 1000.00      1
 0.00000000E+00 0.00000000E+00 0.00000000E+00 0.00000000E+00 0.00000000E+00    2
 0.00000000E+00 0.00000000E+00 0.00000000E+00 0.00000000E+00 0.00000000E+00    3
 0.00000000E+00 0.00000000E+00 0.00000000E+00 0.00000000E+00                   4
H2O(s)          (adjust)  H   2O   1NI  1    0     500.00   2000.00 2000.00      1
 3.50421382E+00 6.68594839E-04 1.76268743E-06-1.17030152E-09 2.26185355E-13    2
-3.79129166E+04-1.05582534E+01 3.50421382E+00 6.68594839E-04 1.76268743E-06    3
-1.17030152E-09 2.26185355E-13-3.79129166E+04-1.05582534E+01                   4
H(s)            (adjust)  H   1NI  1    0    0     500.00   2000.00 2000.00      1
 1.38522354E+00-3.60291509E-05 1.01482878E-06-6.39234047E-10 1.26064639E-13    2
-5.45886573E+03-5.04262898E+00 1.38522354E+00-3.60291509E-05 1.01482878E-06    3
-6.39234047E-10 1.26064639E-13-5.45886573E+03-5.04262898E+00                   4
OH(s)           (adjust)  H   1O   1NI  1    0     500.00   2000.00 2000.00      1
 2.08905501E+00 1.71443903E-03-4.27838552E-07 9.11211411E-12 1.13760370E-14    2
-2.67334298E+04-3.86138841E+00 2.08905501E+00 1.71443903E-03-4.27838552E-07    3
 9.11211411E-12 1.13760370E-14-2.67334298E+04-3.86138841E+00                   4
CO(s)           (adjust)  C   1O   1NI  1    0     500.00   2000.00 2000.00      1
 1.04958397E+00 5.37825549E-03-3.51895909E-06 1.06323431E-09-1.12689240E-13    2
-2.73744388E+04 7.60559022E+00 1.04958397E+00 5.37825549E-03-3.51895909E-06    3
 1.06323431E-09-1.12689240E-13-2.73744388E+04 7.60559022E+00                   4
C(s)            (adjust)  C   1NI  1    0    0     500.00   2000.00 2000.00      1
-3.49330914E+00 5.23524687E-03-3.03308918E-06 6.55611035E-10-1.40966550E-14    2
-2.23124726E+03 7.68421239E+00-3.49330914E+00 5.23524687E-03-3.03308918E-06    3
 6.55611035E-10-1.40966550E-14-2.23124726E+03 7.68421239E+00                   4
CH3(s)          (adjust)  C   1H   3NI  1    0     500.00   2000.00 2000.00      1
-6.10760599E-01 8.61612510E-03-2.17714930E-06-6.63815294E-10 3.13819319E-13    2
-8.89792082E+03-2.00828704E+00-6.10760599E-01 8.61612510E-03-2.17714930E-06    3
-6.63815294E-10 3.13819319E-13-8.89792082E+03-2.00828704E+00                   4
CH2(s)          (adjust)  C   1H   2NI  1    0     500.00   2000.00 2000.00      1
-1.56917589E+00 7.30948876E-03-2.33683999E-06-2.63575385E-10 2.08877321E-13    2
 1.94307500E+03 4.44265982E+00-1.56917589E+00 7.30948876E-03-2.33683999E-06    3
-2.63575385E-10 2.08877321E-13 1.94307500E+03 4.44265982E+00                   4
CH(s)           (adjust)  C   1H   1NI  1    0     500.00   2000.00 2000.00      1
-2.52762352E+00 6.00297402E-03-2.49669461E-06 1.36758705E-10 1.03915796E-13    2
 9.56681068E+03 7.44010148E+00-2.52762352E+00 6.00297402E-03-2.49669461E-06    3
 1.36758705E-10 1.03915796E-13 9.56681068E+03 7.44010148E+00                   4
CH4(s)          (adjust)  C   1H   4NI  1    0     500.00   2000.00 2000.00      1
 3.47651462E-01 9.92277358E-03-2.01747493E-06-1.06404583E-09 4.18759375E-13    2
-1.38997273E+04-4.61646253E+00 3.47651462E-01 9.92277358E-03-2.01747493E-06    3
-1.06404583E-09 4.18759375E-13-1.38997273E+04-4.61646253E+00                   4
O(s)            (adjust)  O   1NI  1    0    0     500.00   2000.00 2000.00      1
 9.33885773E-01 1.49287485E-03-1.51153811E-06 7.60133452E-10-1.42499395E-13    2
-2.88011883E+04-3.47247502E+00 9.33885773E-01 1.49287485E-03-1.51153811E-06    3
 7.60133452E-10-1.42499395E-13-2.88011883E+04-3.47247502E+00                   4
CO2(s)          (adjust)  C   1O   2NI  1    0     500.00   2000.00 2000.00      1
 2.15782085E+00 8.85798101E-03-7.33295570E-06 3.01455469E-09-4.83617407E-13    2
-5.17211366E+04-3.96778204E-01 2.15782085E+00 8.85798101E-03-7.33295570E-06    3
 3.01455469E-09-4.83617407E-13-5.17211366E+04-3.96778204E-01                   4
HCO(s)          (adjust)  C   1H   1O   1NI  1     500.00   2000.00 2000.00      1
 1.42054865E+00 6.41898600E-03-3.25611216E-06 6.60406470E-10-1.25958802E-14    2
-1.72299589E+04-1.34060408E+00 1.42054865E+00 6.41898600E-03-3.25611216E-06    3
 6.60406470E-10-1.25958802E-14-1.72299589E+04-1.34060408E+00                   4
END
```

A4.2 - Surface Reactions

```
SITE   /NI_surface/   SDEN /2.66E-09/
     NI(s)             /1/
     H2O(s)            /1/
     H(s)              /1/
     OH(s)             /1/
     CO(s)             /1/
     C(s)              /1/
     CH3(s)            /1/
     CH2(s)            /1/
     CH(s)             /1/
     CH4(s)            /1/
     O(s)              /1/
     CO2(s)            /1/
     HCO(s)            /1/
END

REACTIONS   KJOULES/MOLE
   H2     +   2NI(s)   =>   2H(s)              1.000E-002  0.00     0.0
          STICK
  2H(s)                 =>    H2     +   2NI(s)  2.545E+019  0.00    81.2
   O2     +   2NI(s)   =>   2O(s)              1.000E-002  0.00     0.0
          STICK
  2O(s)                 =>    O2     +   2NI(s)  4.283E+023  0.00   474.9
   CH4    +    NI(s)   =>    CH4(s)            8.000E-003  0.00     0.0
          STICK
   CH4(s)               =>    CH4    +    NI(s)  8.705E+015  0.00    37.5
   H2O    +    NI(s)   =>    H2O(s)            1.000E-001  0.00     0.0
          STICK
   H2O(s)               =>    H2O    +    NI(s)  3.732E+012  0.00    60.8
   CO2    +    NI(s)   =>    CO2(s)            1.000E-005  0.00     0.0
          STICK
   CO2(s)               =>    CO2    +    NI(s)  6.447E+007  0.00    26.0
   CO     +    NI(s)   =>    CO(s)             5.000E-001  0.00     0.0
          STICK
   CO(s)                =>    CO     +    NI(s)  3.563E+011  0.00   111.3
          COV        /CO(s)                    0.000E+000  0.00   -50.0/
   H(s)   +    O(s)    =>    NI(s)  +    OH(s)  5.000E+022  0.00    97.9
   NI(s)  +    OH(s)   =>    H(s)   +    O(s)   1.781E+021  0.00    36.1
   H(s)   +    OH(s)   =>    NI(s)  +    H2O(s) 3.000E+020  0.00    42.7
   NI(s)  +    H2O(s)  =>    H(s)   +    OH(s)  2.271E+021  0.00    91.8
  2OH(s)                =>    H2O(s) +    O(s)   3.000E+021  0.00   100.0
   H2O(s) +    O(s)    =>   2OH(s)              6.373E+023  0.00   210.9
   C(s)   +    O(s)    =>    NI(s)  +    CO(s)  5.200E+023  0.00   148.1
   NI(s)  +    CO(s)   =>    C(s)   +    O(s)   1.354E+022 -3.00   116.1
          COV        /CO(s)                    0.000E+000  0.00   -50.0/
   CO(s)  +    O(s)    =>    NI(s)  +    CO2(s) 2.000E+019  0.00   123.6
          COV        /CO(s)                    0.000E+000  0.00   -50.0/
   NI(s)  +    CO2(s)  =>    CO(s)  +    O(s)   4.653E+023 -1.00    89.3
   NI(s)  +    HCO(s)  =>    H(s)   +    CO(s)  3.700E+021  0.00     0.0
          COV        /CO(s)                    0.000E+000  0.00    50.0/
   H(s)   +    CO(s)   =>    NI(s)  +    HCO(s) 4.019E+020 -1.00   132.2
   NI(s)  +    HCO(s)  =>    CH(s)  +    O(s)   3.700E+024 -3.00    95.8
   CH(s)  +    O(s)    =>    NI(s)  +    HCO(s) 4.604E+020  0.00   110.0
   NI(s)  +    CH4(s)  =>    H(s)   +    CH3(s) 3.700E+021  0.00    57.7
   H(s)   +    CH3(s)  =>    NI(s)  +    CH4(s) 6.034E+021  0.00    61.6
   NI(s)  +    CH3(s)  =>    H(s)   +    CH2(s) 3.700E+024  0.00   100.0
   H(s)   +    CH2(s)  =>    NI(s)  +    CH3(s) 1.293E+023  0.00    55.3
   NI(s)  +    CH2(s)  =>    H(s)   +    CH(s)  3.700E+024  0.00    97.1
   H(s)   +    CH(s)   =>    NI(s)  +    CH2(s) 4.089E+024  0.00    79.2
   NI(s)  +    CH(s)   =>    H(s)   +    C(s)   3.700E+021  0.00    18.8
   H(s)   +    C(s)    =>    NI(s)  +    CH(s)  4.562E+022  0.00   161.1
   CH4(s) +    O(s)    =>    OH(s)  +    CH3(s) 1.700E+024  0.00    88.3
   OH(s)  +    CH3(s)  =>    CH4(s) +    O(s)   9.876E+022  0.00    30.4
   CH3(s) +    O(s)    =>    OH(s)  +    CH2(s) 3.700E+024  0.00   130.1
   OH(s)  +    CH2(s)  =>    CH3(s) +    O(s)   4.607E+021  0.00    23.6
   CH2(s) +    O(s)    =>    OH(s)  +    CH(s)  3.700E+024  0.00   126.8
   OH(s)  +    CH(s)   =>    CH2(s) +    O(s)   1.457E+023  0.00    47.1
   CH(s)  +    O(s)    =>    OH(s)  +    C(s)   3.700E+021  0.00    48.1
   OH(s)  +    C(s)    =>    CH(s)  +    O(s)   1.625E+021  0.00   128.6
END
```

Bibliography

1. Assabumrungrat, S., Laosiripojana, N., Pavarajarn, V., Sangtongkitcharoen, W., Tangjitmatee, A., & Praserthdam, P. (2005). Thermodynamic analysis of carbon formation in a solid oxide fuel cell with a direct internal reformer fuelled by methanol. *Journal of Power Sources, 139*(1-2), 55-60. doi:10.1016/j.jpowsour.2004.06.065
2. Bartholomew, C. H. (2001). Mechanisms of catalyst deactivation. *Applied Catalysis A: General, 212*(1-2), 17-60. doi:10.1016/s0926-860x(00)00843-7
3. Battelle. (2016). *Manufacturing Cost Analysis of 100 and 250 kW Fuel Cell Systems for Primary Power and Combined Heat and Power Applications*. Retrieved from https://www.energy.gov/sites/prod/files/2016/07/f33/fcto_battelle_mfg_cost_analysis_pp_chp_fc_systems.pdf
4. Biert, L. v. (2020). Solid Oxide Fuel Cell for Ships. Retrieved from https://repository.tudelft.nl/islandora/object/uuid%3Add1f7899-38ee-4c78-a5b0-a6fa92c90f56
5. Blum, L., Batfalsky, P., Fang, Q., De Haart, L. G. J., Malzbender, J., Margaritis, N., . . . Peters, R. (2015). SOFC Stack and System Development at Forschungszentrum Jülich. *Journal of The Electrochemical Society, 162*(10), F1199-F1205. doi:10.1149/2.0491510jes
6. Boaro, M., & Salvatore, A. (2017). Advances in Medium and High Temperature Solid Oxide Fuel Cell Technology (Vol. 574).
7. BP. (2019). Full Report - BP Statistical Review of World Energy 2019. Retrieved from London UK:
8. Carlsson, M. (2015). Carbon Formation in Steam Reforming and Effect of Potassium Promotion. *Johnson Matthey Technology Review, 59*(4), 313-318. doi:10.1595/205651315x688992
9. Clague, R., Marquis, A. J., & Brandon, N. P. (2012). Finite element and analytical stress analysis of a solid oxide fuel cell. *Journal of Power Sources, 210*, 224-232. doi:10.1016/j.jpowsour.2012.03.027
10. Coltrin, M. E., Kee, R. J., & Rupley, F. M. (1991). Surface chemkin: A general formalism and software for analyzing heterogeneous chemical kinetics at a gas-surface interface. *International Journal of Chemical Kinetics, 23*(12), 1111-1128. doi:10.1002/kin.550231205
11. Davis, R., & Haataja, M. (2017). Microstructural stability of supported metal catalysts: A phase field approach. *Journal of Power Sources, 369*, 111-121. doi:10.1016/j.jpowsour.2017.09.066
12. Detchem.com. (2021). DETCHEM Detailed Chemistry in CFD | Simulate reacting flows. Retrieved from https://www.detchem.com/mechanisms
13. Fan, L., Van Biert, L., Thallam Thattai, A., Verkooijen, A. H. M., & Aravind, P. V. (2015). Study of Methane Steam Reforming kinetics in operating Solid Oxide Fuel Cells: Influence of current density. *International Journal of Hydrogen Energy, 40*(15), 5150-5159. doi:10.1016/j.ijhydene.2015.02.096
14. Figueiredo, J. (1986). Gasification of carbon deposits on catalysts and metal surfaces. *Fuel, 65*(10), 1377-1382. doi:10.1016/0016-2361(86)90108-0
15. Hanjalic, K., Kenjeres, S., Tummers, M., & H.J.J, J. (2008). *"Analysis and Modelling of Physical Transport Phenomena"*.
16. Hanna, J., Lee, W. Y., Shi, Y., & Ghoniem, A. F. (2014). Fundamentals of electro- and thermochemistry in the anode of solid-oxide fuel cells with hydrocarbon and syngas fuels. *Progress in Energy and Combustion Science, 40*, 74-111. doi:10.1016/j.pecs.2013.10.001
17. Haverkort, J. W. (2019). A theoretical analysis of the optimal electrode thickness and porosity. *Electrochimica Acta, 295*, 846-860. doi:https://doi.org/10.1016/j.electacta.2018.10.065
18. Haverkort, J. W. (2020). *Electrochemical Energy Storage II*. Lecture Notes. Process & Energy. TU Delft.
19. Hecht, E. S., Gupta, G. K., Zhu, H., Dean, A. M., Kee, R. J., Maier, L., & Deutschmann, O. (2005). Methane reforming kinetics within a Ni–YSZ SOFC anode support. *Applied Catalysis A: General, 295*(1), 40-51. doi:10.1016/j.apcata.2005.08.003
20. Jong, W. (2014). Biomass as a Sustainable Energy Source for the Future: Fundamentals of Conversion Processes.
21. Kakac, S., Pramuanjaroenkij, A., & Zhou, X. (2007). A review of numerical modeling of solid oxide fuel cells. *International Journal of Hydrogen Energy, 32*(7), 761-786. doi:10.1016/j.ijhydene.2006.11.028
22. Koh, J.-H., Kang, B.-S., Lim, H., & Yoo, Y.-S. (2001). Thermodynamic Analysis of Carbon Deposition and Electrochemical Oxidation of Methane for SOFC Anodes. *Electrochemical and Solid State Letters - ELECTROCHEM SOLID STATE LETT, 4*. doi:10.1149/1.1339237
23. Laosiripojana, N., & Assabumrungrat, S. (2007). Catalytic steam reforming of methane, methanol, and ethanol over Ni/YSZ: The possible use of these fuels in internal reforming SOFC. *Journal of Power Sources, 163*(2), 943-951. doi:10.1016/j.jpowsour.2006.10.006
24. Li, C., Shi, Y., & Cai, N. (2011). Mechanism for carbon direct electrochemical reactions in a solid oxide electrolyte direct carbon fuel cell. *Journal of Power Sources, 196*(2), 754-763. doi:10.1016/j.jpowsour.2010.07.076
25. Li, C., Shi, Y., & Cai, N. (2013). Carbon deposition on nickel cermet anodes of solid oxide fuel cells operating on carbon monoxide fuel. *Journal of Power Sources, 225*, 1-8. doi:10.1016/j.jpowsour.2012.10.018
26. Lipman, T. E. W., Adam. (2019). Fuel Cells and Hydroden Production. New York: Springer-Verlag.
27. Liso, V., Cinti, G., Nielsen, M. P., & Desideri, U. (2016). Solid oxide fuel cell performance comparison fueled by methane, MeOH, EtOH and gasoline surrogate C 8 H 18. *Applied Thermal Engineering, 99*, 1101-1109. doi:10.1016/j.applthermaleng.2015.12.044

28. Ma, T., Zhang, Z., Lin, W., Cong, M., & Yang, Y. (2021). Impedance prediction model based on convolutional neural networks methodology for proton exchange membrane fuel cell. *International Journal of Hydrogen Energy*. doi:https://doi.org/10.1016/j.ijhydene.2021.02.204
29. Milewski, J., & Świrski, K. (2009). Modelling the SOFC behaviours by artificial neural network. *International Journal of Hydrogen Energy - INT J HYDROGEN ENERG, 34*, 5546-5553. doi:10.1016/j.ijhydene.2009.04.068
30. Milewski, J., Świrski, K., Santarelli, M., & Leone, P. (2011). *Advanced Methods of Solid Oxide Fuel Cell Modeling* (Vol. 40).
31. Mogensen, D., Grunwaldt, J. D., Hendriksen, P. V., Dam-Johansen, K., & Nielsen, J. U. (2011). Internal steam reforming in solid oxide fuel cells: Status and opportunities of kinetic studies and their impact on modelling. *Journal of Power Sources, 196*(1), 25-38. doi:10.1016/j.jpowsour.2010.06.091
32. Natesakhawat, S., Watson, R., Wang, X., & Ozkan, U. (2005). Deactivation characteristics of lanthanide-promoted sol–gel Ni/Al2O3 catalysts in propane steam reforming. *Journal of Catalysis, 234*(2), 496-508. doi:10.1016/j.jcat.2005.07.014
33. Offer, G. J., Mermelstein, J., Brightman, E., & Brandon, N. P. (2009). Thermodynamics and Kinetics of the Interaction of Carbon and Sulfur with Solid Oxide fuel Cell Anodes. *Journal of the American Ceramic Society, 92*(4), 763-780. doi:10.1111/j.1551-2916.2009.02980.x
34. Pan, H., & Barile, C. J. (2020). Electrochemical CO2 reduction to methane with remarkably high Faradaic efficiency in the presence of a proton permeable membrane. *Energy & Environmental Science, 13*(10), 3567-3578. doi:10.1039/d0ee02189j
35. Rakass, S., Oudghiri-Hassani, H., Rowntree, P., & Abatzoglou, N. (2006). Steam reforming of methane over unsupported nickel catalysts. *Journal of Power Sources, 158*(1), 485-496. doi:10.1016/j.jpowsour.2005.09.019
36. Sammes, N. (2006). *Fuel Cell Technology* (1 ed.): Springer-Verlag London.
37. Sasaki, K. (2003). Power Generation Characteristics of SOFCs for Alcohols and Hydrocarbon-Based Fuels. *ECS Proceedings Volumes, 2003-07*(1), 1295-1304. doi:10.1149/200307.1295pv
38. Sasaki, K., Haga, K., Yoshizumi, T., Minematsu, D., Yuki, E., Liu, R., . . . Yokomoto, K. (2011). Chemical durability of Solid Oxide Fuel Cells: Influence of impurities on long-term performance. *Journal of Power Sources, 196*(22), 9130-9140. doi:10.1016/j.jpowsour.2010.09.122
39. Sasaki, K., Hori, Y., Kikuchi, R., Eguchi, K., Ueno, A., Takeuchi, H., . . . Uchida, Y. (2002). Current-Voltage Characteristics and Impedance Analysis of Solid Oxide Fuel Cells for Mixed H[sub 2] and CO Gases. *Journal of The Electrochemical Society, 149*(3), A227. doi:10.1149/1.1435357
40. Sasaki, K., & Teraoka, Y. (2003). Equilibria in Fuel Cell Gases. *Journal of The Electrochemical Society, 150*(7), A885. doi:10.1149/1.1577338
41. Sasaki, K., Yoshizumi, T., Haga, K., Yoshitomi, H., Hosoi, T., Shiratori, Y., & Taniguchi, S. (2013). Chemical Degradation of SOFCs: External Impurity Poisoning and Internal Diffusion-Related Phenomena. *ECS Transactions, 57*(1), 315-323. doi:10.1149/05701.0315ecst
42. Sehested, J. (2006). Four challenges for nickel steam-reforming catalysts. *Catalysis Today, 111*(1-2), 103-110. doi:10.1016/j.cattod.2005.10.002
43. Sholl, D., & Steckel, J. (2009). Accuracy and Methods beyond "Standard" Calculations. In *Density Functional Theory* (pp. 209-233): Wiley.
44. Silveira, J. L. (2017). *Sustainable Hydrogen Production Processes*: Springer International Publishing Switzerland.
45. Singh, D., Hernández-Pacheco, E., Hutton, P. N., Patel, N., & Mann, M. D. (2005). Carbon deposition in an SOFC fueled by tar-laden biomass gas: a thermodynamic analysis. *Journal of Power Sources, 142*(1-2), 194-199. doi:10.1016/j.jpowsour.2004.10.024
46. Skafte, T. L., Blennow, P., Hjelm, J., & Graves, C. (2018). Carbon deposition and sulfur poisoning during CO2 electrolysis in nickel-based solid oxide cell electrodes. *Journal of Power Sources, 373*, 54-60. doi:10.1016/j.jpowsour.2017.10.097
47. Sovacool, B., & Dworkin, M. H. (2014). Global Energy Justice: Problems, Principles, and Practices.
48. Sun, B., Rudkin, R. A., & Atkinson, A. (2009). Effect of Thermal Cycling on Residual Stress and Curvature of Anode-Supported SOFCs. *Fuel Cells, 9*, 805-813. doi:10.1002/fuce.200800133
49. Tabish, A. N., Patel, H. C., & Aravind, P. V. (2017). Electrochemical Oxidation of Syngas on Nickel and Ceria Anodes. *Electrochimica Acta, 228*, 575-585. doi:10.1016/j.electacta.2017.01.074
50. Takeguchi, T., Kani, Y., Yano, T., Kikuchi, R., Eguchi, K., Tsujimoto, K., . . . Aizawa, M. (2002). Study on steam reforming of CH4 and C2 hydrocarbons and carbon deposition on Ni-YSZ cermets. *Journal of Power Sources, 112*(2), 588-595. doi:10.1016/s0378-7753(02)00471-8
51. Tao, Y., Ebbesen, S. D., & Mogensen, M. B. (2014). Carbon Deposition in Solid Oxide Cells during Co-Electrolysis of H2O and CO2. *Journal of The Electrochemical Society, 161*(3), F337-F343. doi:10.1149/2.079403jes
52. van Beurden, P. (2004). On the Catalytic Aspects of Steam-Methane Reforming. *ECS Proceedings Volumes*, 25.
53. Virkar, A. V. (2005). Theoretical analysis of the role of interfaces in transport through oxygen ion and electron conducting membranes. *Journal of Power Sources, 147*(1-2), 8-31. doi:10.1016/j.jpowsour.2005.01.038
54. Waldbillig, D., Wood, A., & Ivey, D. (2007). Enhancing the Redox Tolerance of Anode-Supported SOFC by Microstructural Modification. *Journal of The Electrochemical Society - J ELECTROCHEM SOC, 154*. doi:10.1149/1.2402116
55. Wang, S., & Lu, G. Q. (1998). Role of CeO2 in Ni/CeO2–Al2O3 catalysts for carbon dioxide reforming of methane. *Applied Catalysis B: Environmental, 19*(3-4), 267-277. doi:10.1016/s0926-3373(98)00081-2

56. Wang, Z., Weng, W., Cheng, K., Du, P., Shen, G., & Han, G. (2008). Catalytic modification of Ni–Sm-doped ceria anodes with copper for direct utilization of dry methane in low-temperature solid oxide fuel cells. *Journal of Power Sources, 179*(2), 541-546. doi:10.1016/j.jpowsour.2008.01.040
57. Watanabe, H., Okino, R., & Hanamura, K. (2019). Structural evolution of carbon deposition on a Ni/YSZ cermet of a SOFC analyzed by soft x-ray XANES spectroscopy. *International Journal of Hydrogen Energy, 44*(43), 24028-24035. doi:10.1016/j.ijhydene.2019.07.122
58. Wood, A., Pastula, M., Waldbillig, D., & Ivey, D. (2006). Initial Testing of Solutions to Redox Problems with Anode-Supported SOFC. *Journal of The Electrochemical Society, 153*, A1929-A1934. doi:10.1149/1.2240085
59. Wu, H., La Parola, V., Pantaleo, G., Puleo, F., Venezia, A., & Liotta, L. (2013). Ni-Based Catalysts for Low Temperature Methane Steam Reforming: Recent Results on Ni-Au and Comparison with Other Bi-Metallic Systems. *Catalysts, 3*(2), 563-583. doi:10.3390/catal3020563
60. Xiong, Y., Yamaji, K., Horita, T., Yokokawa, H., Akikusa, J., Eto, H., & Inagaki, T. (2009). Sulfur Poisoning of SOFC Cathodes. *Journal of The Electrochemical Society, 156*(5), B588. doi:10.1149/1.3090169
61. Xu, H., & Dang, Z. (2016). Lattice Boltzmann modeling of carbon deposition in porous anode of a solid oxide fuel cell with internal reforming. *178*, 294-307. doi:10.1016/j.apenergy.2016.06.007
62. Yokokawa, H., Watanabe, T., Ueno, A., & Hoshino, K. (2019). Investigation on Degradation in Long-Term Operations of Four Different Stack/Modules. *ECS Transactions, 7*(1), 133-140. doi:10.1149/1.2729082
63. Yurkiv, V. (2014). Reformate-operated SOFC anode performance and degradation considering solid carbon formation: A modeling and simulation study. *143*, 114-128. doi:10.1016/j.electacta.2014.07.136
64. Zhao, F., & Virkar, A. (2005). Dependence of polarization in anode-supported solid oxide fuel cells on various cell parameters. *Journal of Power Sources, 141*(1), 79-95. doi:10.1016/j.jpowsour.2004.08.057